

Two-Step Radionuclide Tumor Targeting through Bioorthogonal Mechanism using SPIONs

Fauzia, R.P.

DOI

[10.4233/uuid:9a06806c-a2ad-4588-bfad-0dd537867dbf](https://doi.org/10.4233/uuid:9a06806c-a2ad-4588-bfad-0dd537867dbf)

Publication date

2022

Document Version

Final published version

Citation (APA)

Fauzia, R. P. (2022). *Two-Step Radionuclide Tumor Targeting through Bioorthogonal Mechanism using SPIONs*. [Dissertation (TU Delft), Delft University of Technology]. <https://doi.org/10.4233/uuid:9a06806c-a2ad-4588-bfad-0dd537867dbf>

Important note

To cite this publication, please use the final published version (if applicable). Please check the document version above.

Copyright

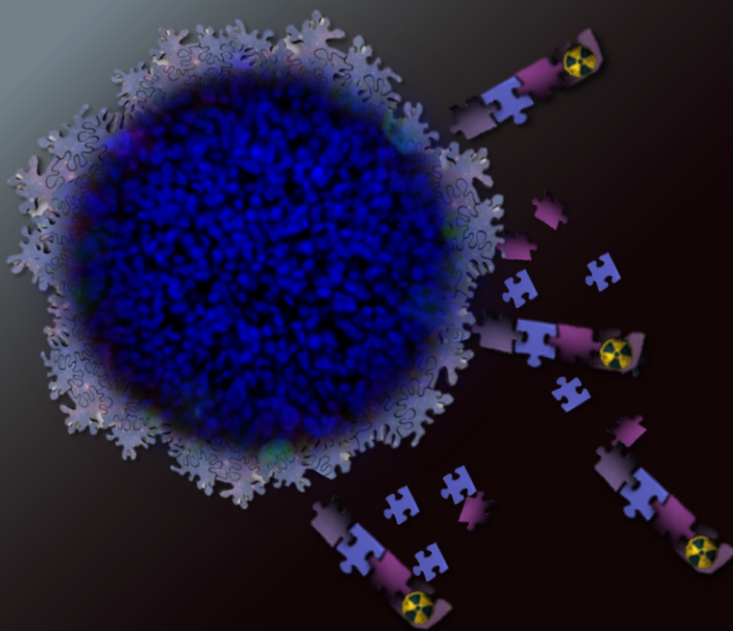
Other than for strictly personal use, it is not permitted to download, forward or distribute the text or part of it, without the consent of the author(s) and/or copyright holder(s), unless the work is under an open content license such as Creative Commons.

Takedown policy

Please contact us and provide details if you believe this document breaches copyrights. We will remove access to the work immediately and investigate your claim.

Two-Step Radionuclide Tumor Targeting through Bioorthogonal Mechanism using SPIONs

Retna Putri Fauzia



Two-Step Radionuclide Tumor Targeting through Bioorthogonal Mechanism using SPIONs

Retna Putri FAUZIA

Two-Step Radionuclide Tumor Targeting through Bioorthogonal Mechanism using SPIONS

Proefschrift

ter verkrijging van de graad van doctor
aan de Technische Universiteit Delft,
op gezag van de Rector Magnificus Prof.dr.ir. T.H.J.J. van der Hagen,
voorzitter van het College voor Promoties,
in het openbaar te verdedigen
op dinsdag 25 januari 2022 om 12.30 uur

door

Retna Putri FAUZIA

Magister Sains - Ilmu Kimia, Universitas Padjadjaran, Indonesië
geboren te Serang, Indonesië

Dit proefschrift is goedgekeurd door de promotoren:

Dr. K. Djanashvili

Dr.ir. A.G. Denkova

Samenstelling promotiecommissie:

Rector Magnificus,	voorzitter
Dr. K. Djanashvili	Technische Universiteit Delft, promotor
Dr.ir. A.G. Denkova	Technische Universiteit Delft, promotor

Onafhankelijke leden:

Dr. G. Digilio	Universita del Piemonte Orientale, Italië
Dr. S. Lacerda	CNRS Orléans, Frankrijk
Prof.dr. R.U.M.S. Soedjanaatmadja	Universitas Padjadjaran, Indonesië
Dr. R. Eelkema	Technische Universiteit Delft
Prof.dr. H.T. Wolterbeek	Technische Universiteit Delft
Prof.dr. U. Hanefeld	Technische Universiteit Delft, reserve lid

This PhD project is fully funded by Lembaga Dana Pengelola Dana Pendidikan Republik Indonesia (Indonesia Endowment Fund for Education).



lembaga pengelola dana pendidikan

The research in this thesis is performed at the Department of Radiation Science and Technology and Department of Biotechnology, Faculty of Applied Sciences, Delft University Of Technology, the Netherlands.

ISBN: 978-94-6384-295-2

Copyright © 2021 by Retna Putri Fauzia

All rights reserved. No part of the material protected by this copyright notice may be reproduced or utilized in any form or by any other means, electronic or mechanical, including photocopying, recording or by any information storage and retrieval system, without written permission from the author.

Printed in the Netherlands by Gildeprint

To my parents...

Table of Contents

Chapter 1: General Introduction	1
Introduction	2
Radionuclide therapy	3
Drug delivery strategies	4
Click-reaction	7
Outline of the thesis.....	8
References	11
Chapter 2: Potential of MRI in Radiotherapy Mediated by Small-Conjugates and Nanosystems	15
Introduction	16
The role of MRI in External Radiation Therapy	18
The role of MRI in Internal Radionuclide Therapy	28
Neutron Capture Therapy combined with MRI.....	34
Conclusions	38
References	40
Chapter 3: Preparation and Surface Functionalization of Superparamagnetic Iron Oxide Nanoparticles Designed for Theranostic Application	47
Introduction	48
Results and Discussion	50
Conclusions	67
Experimental details	68
Acknowledgement	72
References	73
Chapter 4: <i>In vitro</i> Evaluation of Click-reaction between Azide-functionalized SPIONs and DOTA-cyclooctyne	77
Introduction	78
Results and Discussion	81

Conclusions	97
Experimental details	98
Acknowledgement	101
References	102
Chapter 5: Evaluation of the therapeutic effect of the alpha-emitter ²²⁵Ac in combination with SPIONs	105
Introduction	106
Results and Discussion	108
Conclusions	115
Experimental details	115
References	119
Summary	121
Samenvatting	125
Acknowledgements	129
List of publications	133
Curriculum Vitae	135

General Introduction

1

Introduction

Cancer is currently the second most frequent cause of death with more than a million cases happening yearly in Europe. In 2020, cancer accounted for 10 million lethal cases worldwide (WHO Data). There are several types of cancer treatments, which are typically applied in the current clinical practice. Surgery is usually the first choice often combined with external beam therapy and chemotherapy. In the case of metastasised tumors chemotherapy or radionuclide therapy is preferred.^[1] In the last few years radionuclide therapy has gained a lot of attention since it has shown to lead to considerable prolongation of the life expectancy of terminal patients.^[2] Timely diagnosis plays an important role here, increasing the survival chances for cancer patients and allowing to choose the most optimal treatment based on disease characteristics. To do that, numerous imaging techniques are used, such as Magnetic Resonance Imaging (MRI), Computed Tomography (CT), Ultrasonography (US), Single Photon Emission Computed Tomography (SPECT) and Positron Emission Tomography (PET). Each of these techniques differ in terms of resolution, sensitivity and application of imaging agents. Thereby, the type and stage of the disease usually dictate the choice for a certain imaging modality. The benefits of monitoring the delivery of therapeutics as well as monitoring of the therapeutic outcome are important for an optimal treatment. Therefore, the current research is very much focused on the development of agents that combine imaging and therapeutic components in one system, called *theranostics*,^[3] which is seen as the key to a high-precision cancer treatment.^[4]

One way to realize a theranostic product is by implementing metals with dual and even triple properties, such as in the case of the beta-emitters ^{177}Lu ($t_{1/2} = 2.8$ d) and ^{166}Ho ($t_{1/2} = 2.1$ d), respectively. ^{177}Lu has been used in peptide receptor radionuclide therapy (PRRT) through administration of ^{177}Lu -DOTA-Tyr³-octreotate (DOTATATE). In this case, the accumulation of the agent at the tumor through somatostatin receptors overexpressed at the disease site visualized by SPECT, is combined with the delivery of therapeutic radiation dose leading to a promising treatment.^[5] ^{166}Ho has a similar multimodal potential as it can be observed by SPECT and additionally by MRI (due to its high magnetic moment of 10.6 μB), and kill tumors by delivering beta-radiation.^[6] ^{166}Ho -microspheres are already applied

successfully in the clinic for radioembolization of liver cancer, and their feasibility for head-and-neck^[7] and brain^[8] cancers is being investigated.

Another promising approach is exploiting nanotheranostics^[9] by development of small nanoparticles composed of polymers,^[10] inorganic materials,^[11] dendrimeric structures,^[12] and lipids,^[13] which can be used to conjugate or encapsulate diagnostic and therapeutic moieties.^[14] Nanosystems are believed to play an important role in the future cancer theranostics due to their versatility and advantageous pharmacokinetic features, such as prolonged blood-circulation time, tumor accumulation/retention, and most importantly, the ability to carry multiple components in one scaffold. These benefits are especially attractive in the case of radionuclide therapy, which is explored in this thesis.

Radionuclide therapy

An important advantage of radionuclide therapy compared to the conventional external beam radiation therapy is its capability to treat metastasized tumors using rather high radiation dose.^[1] The effects depend on the radiation dose and type of the accompanying linear transfer (LET) energy causing the DNA damage. DNA can be damaged directly by the radiation itself or indirectly through generated reactive oxygen species (ROS) and hydrated electrons. As a consequence, cells that are exposed to radioactivity, *i.e.* in the proximity of radionuclides, will undergo apoptosis.^[15]

There are several radionuclides, which are currently being applied in the clinic. These include beta-emitting radionuclides ^{131}I ($t_{1/2} = 8.0$ d), ^{177}Lu ($t_{1/2} = 6.7$ d), ^{153}Sm ($t_{1/2} = 46.5$ h), and ^{90}Y ($t_{1/2} = 64.1$ h) that are characterized by low LET and approximate range of 0.4 - 5.3 mm in tissues. Despite its very high potential, radionuclide therapy is still often hampered by the relatively low radiation dose delivered to the tumor or inhomogeneity of the dose which is insufficient to kill all cancer cells. Therefore, in radionuclide therapy more and more radionuclides having high linear energy transfer, such as alpha particles are being pursued.

Alpha-therapy

Alpha-emitting radionuclides are receiving much attention in oncology due to their appealing therapeutic properties.^[16] For instance, shorter penetration depth (50 – 100 μm) and higher LET (50-250 $\text{keV}/\mu\text{m}$)^[17] compared to the beta-emitting radionuclides lead to more effective DNA destruction, and hence, the cytotoxic effects of alpha-particles are much more potent.^[18] Several alpha-emitters such as astatine-211 (^{211}At , 7.2h), bismuth-213 (^{213}Bi , 45.6 min), radium-223 (^{223}Ra , 11.4 d), and actinium-225 (^{225}Ac , 10.0 d) are currently under investigation.^[16] There, the latter radionuclide is the most interesting one due to its convenient half-life.^[19] The challenge in the case of ^{225}Ac is the release of its daughters due to the recoil effect resulting from the alpha-emission. The energy that the recoiling daughter receives is above 100 keV, which leads to breaking of chemical bonds. Some of the daughters such as ^{221}Fr and ^{213}Bi (i.e. ^{213}Po) are relatively long-lived alpha-emitters in this situation,^[20] and therefore, their release can damage healthy tissues and organs.^[21] Therefore, in the case of alpha-radionuclide therapy it is very important to deliver the alpha emitting radionuclides to the site of interest very fast and selectively, preventing harm to the healthy tissues.^[20]

Drug delivery strategies

Passive targeting

Considering nanotheranostic materials, it is important to realize that the size of the nanoparticles is an essential determinant for an effective tumor delivery. Nanoparticles with the sizes below 5-10 nm are typically excreted by the kidneys,^[22] while larger particles (20-100 nm) are most likely ending up in the liver and/or spleen.^[23] Accumulation of larger nanoparticles in the lungs has also been reported.^[24] Provided that the nanoparticles are not instantly removed from the blood-circulation, their accumulation at the tumor site can be expected. The reason for this *passive targeting* is the rapid tumor growth that is associated with formation of neovasculature. The immature blood vessels are composed of endothelial cells that are more permeable compared to those around the normal tissues.

These leaky blood vessels allow nanoparticles to extravasate through the gaps and accumulate at the tumor site (Figure 1.1). This phenomenon is called enhanced permeability and retention (EPR) effect, widely exploited in tumor drug delivery of nanoparticles.^[25] Basically, correctly chosen size of the nanoparticles facilitates blood-circulation and thus higher tumor uptake.^[26]

However, size is not the only parameter determining the blood-circulation and tumor uptake. The surface properties also play an important role in the tumor accumulation, mainly due to the recognition of nanoparticles by the immune system resulting in activation of macrophages and fast clearance from the blood stream.^[27] To prevent this, nanoparticles are typically decorated with stealth molecules that prevent the premature removal of the nanoparticles, and by doing this, prolong the circulation time allowing for accumulation at the tumor. Polyethyleneglycol (PEG) is one of the typically used coating macromolecules that is known to enhance biocompatibility of the nanoparticles and increase their blood-circulation time.^[28] When injected intravenously, PEG-coated nanoparticles will neither be recognized as foreign objects nor be taken up by the macrophages and mononuclear phagocyte system (MPS) cells.^[29] Additionally, PEGylation of the surface of nanoparticles can enhance their hydrophilicity and colloidal stability, thus preventing their aggregation.^[30]

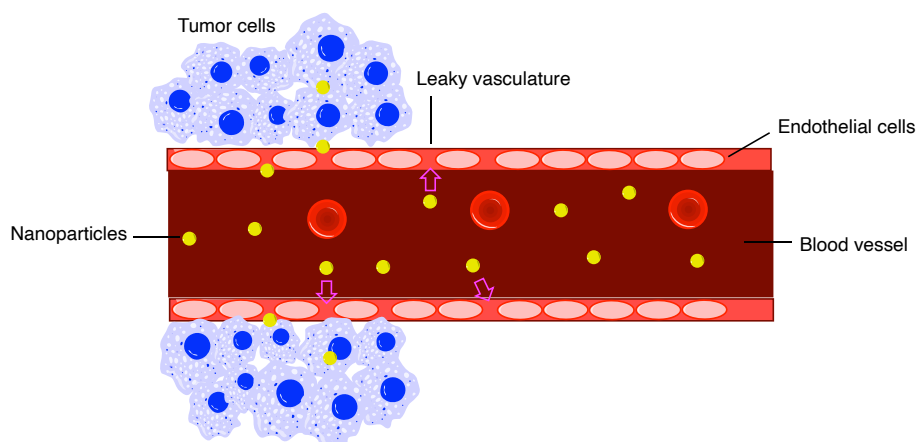


Figure 1.1. Schematic of nanoparticles taking part in the EPR effect in the tumor vasculature.

Active targeting

While the effectiveness of passive targeting is still under debate,^[31] another strategy for specific tumor delivery by means of targeting vectors is implemented. These vectors range from small molecules, such as folic acid (FA),^[32] prostate specific membrane antigen (PSMA),^[33] to large entities such as monoclonal antibodies (mAbs).^[34] The principle is based on the recognition of tumors by binding to overexpressed receptors. In the case of folic acid receptors (FAR), four different types can be distinguished: FAR- α , FAR- β , FAR- γ , and FAR- δ .^[35] Among of these, FAR- α is most commonly used for targeted drug delivery due to its overexpression on cancer tissues.^[36] FAR on the normal tissues are limited to the kidney, and epithelia of intestine, lung, retina, placenta and choroid plexus, and thus not accessible for the binding with the blood-circulating targeting agents. The affinity to FAR- α ($K_d = 10^{-10}$ M) at the surface of ovarian, lung, breast, brain, and endometrium tumor cells is sufficient for FA to be used as a targeting vector in combination with nanoparticles.^[37]

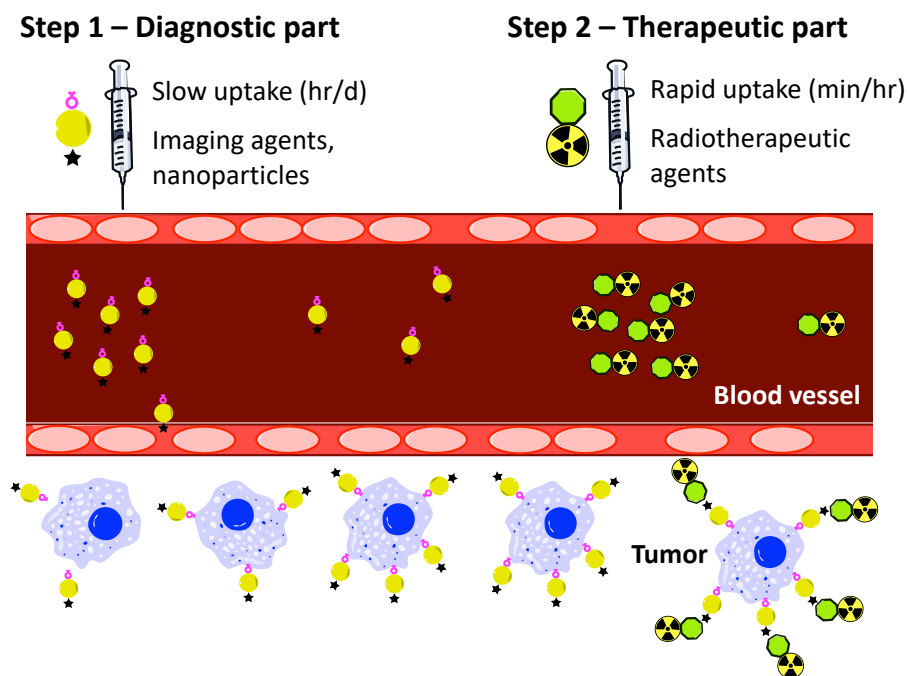


Figure 1.2. Schematic representation of the pretargeting approach.

Pretargeting

Pretargeting concept involves injecting two components in sequence, from which the first is used to target the tumor and the second to seek the tumor-bound moiety. When a theranostic approach is concerned, one of the components has an additional imaging capacity (Figure 1.2). Being already applied preclinically, this strategy has a clear potential for monitoring the therapeutic response in cancer patients during and after the treatment.^[38] Initially, the pretargeting strategy was designed for antibodies in radioimmunotherapy using antibody/hapten,^[39] strept(avidin)-biotin,^[40] and *in vivo* click-reaction mechanisms.^[41] The latter example describes injection of an immunconjugate, which was left to circulate, accumulate at the tumor and be cleared from the blood, after which a ⁶⁴Cu-tracer was injected and its binding to the first component via the click-reaction was visualized by PET. When the PET-tracer was cleared, its therapeutic analogue ⁶⁷Cu was injected and delivered to the tumor via the same route for the treatment.^[41] In the current research, the *in vivo* click-reaction strategy is considered very attractive due to the formation of covalent binding that leads to a higher tumor uptake of the radiopharmaceuticals.^[42]

Click-reaction

A classic representation of the click-reaction is copper catalyzed alkyne-azide cycloaddition (CuAAC).^[43] This reaction is very slow and requires high temperatures and copper as a catalyst to increase the reaction rate (Figure 1.3A).^[44] However, the use of copper *in vivo* has to be ruled out due to its toxicity. Therefore, utilization of highly strained cyclooctyne derivatives has been presented as an alternative click-reaction mediator compatible with living organisms (Figure 1.3B).^[45]

The very first example of the click-reaction *in vivo* was demonstrated by Bertozzi and co-workers, who explored selective labeling of biomolecules to investigate biological processes. For this purpose, mice were injected with an azide-modified sugar N-azidoacetylmannosamine (Ac₄ManNAz), which was then metabolized and came to

expression as part of glycan-chain at the surface of the cells.^[46] Injection of antibody labeled with fluorescein isothiocyanate and cyclooctyne enabled visualization of the target *via* the click-reaction. Keeping in mind that some glycosilation patterns are typical for certain diseases, this approach can be used for therapeutic purposes and enables imaging during the treatment.^[47] High efficiency and selectivity as a result of bioorthogonality without interfrance with physiological processes *in vivo* represent the main arguments for the interest on click-chemistry in the medical field.^[48]

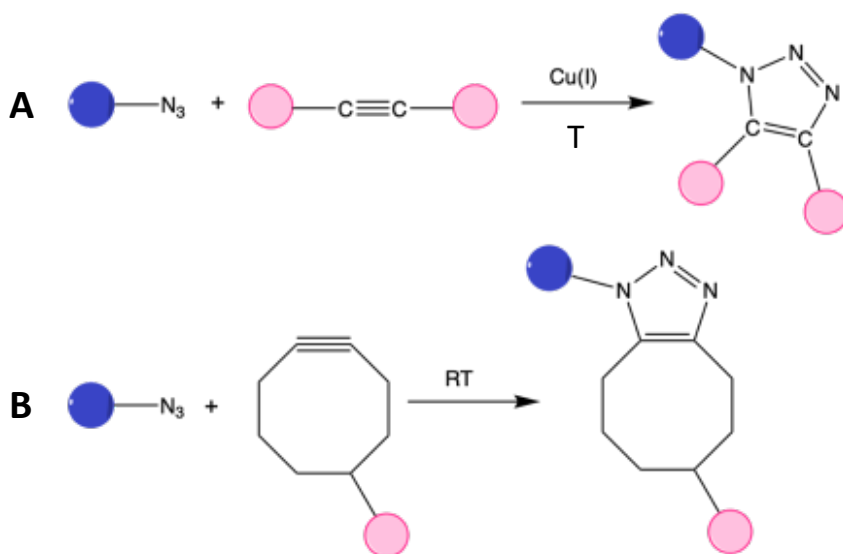


Figure 1.3. Click-reactions between azides and alkynes with (A) and without (B) copper as a catalyst.

Outline of the thesis

The aim of this thesis is to develop a two-step tumor targeting strategy based on the bioorthogonal mechanism by using cyclooctyne promoted click-reaction between azide-functionalized superparamagnetic iron oxide nanoparticles (SPIONs) and alpha-emitting DOTA-cyclooctyne complex. Thereby, the ultimate goal is to exploit this combination for fast and selective delivery of alpha-therapeutics to the tumor under visualization of the whole process with MRI. The principle of MRI-guidance during different types of radiotherapy is reviewed in **Chapter 2**.

Advantage of the two-step tumor pretargeted therapy is the possibility to introduce an MRI-active label on the tumor cells, followed by delivery of the radiotherapeutic in a rapid, and most importantly, selective way. The choice for MRI as an imaging modality is based on its non-invasive character and high resolution. SPIONs, commonly applied as T_2 MRI contrast agents (dark contrast),^[49] can be functionalized on their surface to ensure tumor specificity (folic acid), prolonged circulation times (PEG), click-reaction (azides) and optical signal for *in vitro* confocal microscopy (fluorescein-tag). Once the presence of SPIONs at the tumor site is confirmed by MRI, the radiotherapeutics can be injected in the second step.

The following three chapters focus on the actual development of SPIONs, their full characterization and demonstration of their ability to generate MRI contrast, target tumors and bind radiotherapeutics. The design and preparation of SPIONs as well as functionalization of their surface are explained in **Chapter 3**. Special attention is paid to the size-control and uniformity of the resulting nanoparticles. Examination of different preparation methods leads to conclusion that the co-precipitation procedure is the best method to prepare SPIONs with a diameter of 10 nm and a narrow size-distribution. Besides the morphological and physical properties of the nanoparticles, surface chemistry represents an important aspect in the design of theranostic probes. The purpose of functionalization is firstly to enable conjugation with targeting vectors for specific tumor delivery *via* folic acid receptors overexpressed by a number of tumors. Further modification is necessary to enable the click-reaction with a cyclooctyne-carrying radiotherapeutic molecule. Finally, polyethyleneglycol (PEG) molecules are introduced on the surface of SPIONs and their influence on the tumor-recognition as well as to the cellular uptake is investigated *in vitro*.

Chapter 4 focuses on determination of experimental conditions for an optimal click-reaction between azide-functionalized SPIONs and cyclooctyne-DOTA. Aiming at the final application of an alpha-emitting metal ion, DOTA (1,4,7,10-Tetraazacyclododecane-1,4,7,10-tetraacetate) is first complexed with Eu^{III} and the click-reaction process is studied by NMR and UV-spectroscopies. Further complexation with Gd^{III} enables T_1/T_2 NMR relaxation studies in which the click-reaction can be monitored by increase in relaxation times. Both

types of contrast enhancements simultaneously confirm the successful conjugation between the nanoparticles and the radiotherapeutic prototype.

The effectiveness of the click-reaction under physiological conditions is evident from the *in vitro* experiments, in which the azide-functionalized SPIONs are incubated with HeLa and U87 glioblastoma cells that are grown as 2D pallets and 3D spheroids. Visualization of cell interaction (incl. possible internalization) by confocal microscopy is possible due to the presence of a fluorescent tag at the surface of SPIONs. Complexation of DOTA-cyclooctyne with radioactive metal-ions ^{111}In and ^{177}Lu enables gamma-counting to confirm that the click-reaction took place. In addition, therapeutic effects of beta-emmitter ^{177}Lu is observed using 3D glioblastoma tumor model.

Finally, in the last **Chapter 5** the designed two-step tumor targeting approach is adopted to the alpha-emitter ^{225}Ac . Another series of *in vitro* experiments similar to those described in the previous chapter is performed and the growth and morphology of the cells exposed to the ^{225}Ac -DOTA-complex after the click-reaction with SPIONs accumulated in the tumor is presented. Additionally, DNA damage caused by the alpha-emitter ^{225}Ac to the glioblastoma spheroids is analyzed and the therapeutic impact is evaluated.

References

- [1] R. P. Fauzia, A. G. Denkova and K. Djanashvili, *Inorganics* **2019**, *7*.
- [2] K. Massey and J. Reese, *Journal of Nuclear Medicine* **2015**, *56*, 2702-2702.
- [3] S. S. Kelkar and T. M. Reineke, *Bioconjugate Chemistry* **2011**, *22*, 1879-1903.
- [4] L. B. Solnes, R. A. Werner, K. M. Jones, M. S. Sadaghiani, C. R. Bailey, C. Lapa, M. G. Pomper and S. P. Rowe, *Journal of Nuclear Medicine* **2020**, *61*, 311-318.
- [5] P. M. Kasi, A. Sharma and M. K. Jain, *Case Reports in Oncology* **2019**, *12*, 98-103.
- [6] M. L. J. Smits, M. Elschot, M. A. A. J. van den Bosch, G. H. van de Maat, A. D. van het Schip, B. A. Zonnenberg, P. R. Seevinck, H. M. Verkooijen, C. J. Bakker, H. W. A. M. de Jong, M. G. E. H. Lam and J. F. W. Nijsen, *Journal of Nuclear Medicine* **2013**, *54*, 2093.
- [7] R. C. Bakker, R. J. J. van Es, A. Rosenberg, S. A. van Nimwegen, R. Bastiaannet, H. de Jong, J. F. W. Nijsen and M. Lam, *Nuclear Medicine Communications* **2018**, *39*, 213-221.
- [8] M. de Vries, N. J. M. Klaassen, N. C. Morsink, S. A. van Nimwegen, J. F. W. Nijsen and J. J. van den Dobbelen, *Medical Engineering and Physics* **2021**, *96*, 13-21.
- [9] L. M. Madaswamy S Muthu, Si-Shen Feng, *Nanomedicine* **2014**, *9*, 1277-1280.
- [10] Z. Karimi, S. Abbasi, H. Shokrollahi, G. Yousefi, M. Fahham, L. Karimi and O. Firuzi, *Materials Science and Engineering C: Materials for Biological Applications* **2017**, *71*, 504-511.
- [11] S. Palanisamy and Y.-M. Wang, *Dalton Transactions* **2019**, *48*, 9490-9515.
- [12] F. Fu, Y. Wu, J. Zhu, S. Wen, M. Shen and X. Shi, *ACS Applied Materials and Interfaces* **2014**, *6*, 16416-16425.
- [13] A. Bao, W. T. Phillips, B. Goins, X. Zheng, S. Sabour, M. Natarajan, F. Ross Woolley, C. Zavaleta and R. A. Otto, *International Journal of Pharmaceutics* **2006**, *316*, 162-169.
- [14] P. I. Siafaka, N. U. Okur, I. D. Karantas, M. E. Okur and E. A. Gundogdu, *Asian Journal of Pharmaceutical Sciences* **2021**, *16*, 24-46.
- [15] W. Hur and S. K. Yoon, *International Journal of Molecular Sciences* **2017**, *18*.
- [16] M. Makvandi, E. Dupis, J. W. Engle, F. M. Nortier, M. E. Fassbender, S. Simon, E. R. Birnbaum, R. W. Atcher, K. D. John, O. Rixe and J. P. Norenberg, *Targeted Oncology* **2018**, *13*, 189-203.

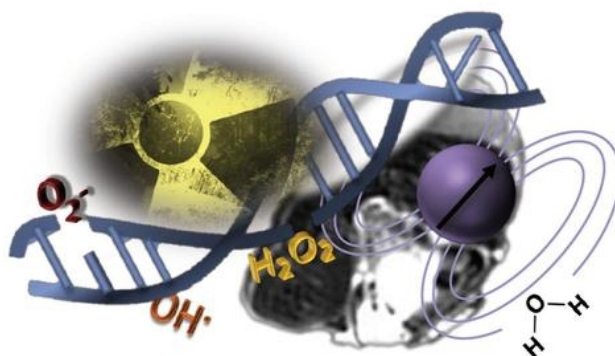
- [17] S. Poty, L. C. Francesconi, M. R. McDevitt, M. J. Morris and J. S. Lewis, *Journal of Nuclear Medicine* **2018**, *59*, 878-884.
- [18] L. Marcu, E. Bezak and B. J. Allen, *Critical Reviews in Oncology/Hematology* **2018**, *123*, 7-20.
- [19] C. A. Alfred Morgenstern, Clemens Kratochwil, Mike Sathekge, Leszek and K. a. F. Bruchertseifer, *Current Radiopharmaceuticals* **2018**, *11*, 200-208.
- [20] R. M. de Kruijff, H. T. Wolterbeek and A. G. Denkova, *Pharmaceuticals (Basel)* **2015**, *8*, 321-336.
- [21] J. Kozempel, O. Mokhodoeva and M. Vlk, *Molecules* **2018**, *23*.
- [22] P. V. Hauser, H.-M. Chang, N. Yanagawa and M. Hamon, *Applied Sciences* **2021**, *11*.
- [23] F. Danhier, O. Feron and V. Preat, *Journal of Controlled Release* **2010**, *148*, 135-146.
- [24] Y. Maitani, Y. Nakamura, M. Kon, E. Sanada, K. Sumiyoshi, N. Fujine, M. Asakawa, M. Kogiso and T. Shimizu, *International Journal of Nanomedicine* **2013**, *8*, 315-323.
- [25] T. S. Hiroshi Maeda, Toshimitsu Konno, *Journal of Controlled Release* **2001**, *74*, 47-61.
- [26] S. Acharya and S. K. Sahoo, *Advanced Drug Delivery Reviews* **2011**, *63*, 170-183.
- [27] E. Sadauskas, H. Wallin, M. Stoltenberg, U. Vogel, P. Doering, A. Larsen and G. Danscher, *Part Fibre Toxicol* **2007**, *4*, 10.
- [28] S. Y. Fam, C. F. Chee, C. Y. Yong, K. L. Ho, A. R. Mariatulqabtiah and W. S. Tan, *Nanomaterials (Basel)* **2020**, *10*.
- [29] P. L. Vanessa Carla Furtado Mosqueira, Annette Gulik, Olivier Bourdon, Ruxandra Gref, Denis Labarre, Gillian Barra, *Biomaterials* **2001**, *22*, 2967-2979.
- [30] J. S. Suk, Q. Xu, N. Kim, J. Hanes and L. M. Ensign, *Advanced Drug Delivery Reviews* **2016**, *99*, 28-51.
- [31] Y. Shi, R. van der Meel, X. Chen and T. Lammers, *Theranostics* **2020**, *10*, 7921-7924.
- [32] S. Haller, J. Reber, S. Brandt, P. Bernhardt, V. Groehn, R. Schibli and C. Muller, *Nuclear Medicine and Biology* **2015**, *42*, 770-779.
- [33] F. Wang, Z. Li, X. Feng, D. Yang and M. Lin, *Prostate Cancer and Prostatic Diseases* **2021**.
- [34] Y. Tokuda, *International Journal of Clinical Oncology* **2003**, *8*, 224-229.

- [35] N. A. Bandara, M. J. Hansen and P. S. Low, *Molecular Pharmaceutics* **2014**, *11*, 1007-1013.
- [36] W. A. H. Philip S. Low, and Derek D. Doorneweerd, *Account of Chemical Research* **2008**, *41*, 120-129.
- [37] A. Cheung, H. J. Bax, D. H. Josephs, K. M. Ilieva, G. Pellizzari, J. Opzoomer, J. Bloomfield, M. Fittall, A. Grigoriadis, M. Figini, S. Canevari, J. F. Spicer, A. N. Tutt and S. N. Karagiannis, *Oncotarget* **2016**, *7*, 52553-52574.
- [38] F. G. v. S. Otto C. Boerman, Wim J.G. Oyen, and Frans H.M. Corstens, *Journal of Nuclear Medicine* **2003**, *44*.
- [39] S. M. Cheal, H. Xu, H. F. Guo, S. G. Lee, B. Punzalan, S. Chalasani, E. K. Fung, A. Jungbluth, P. B. Zanzonico, J. A. Carrasquillo, J. O'Donoghue, P. M. Smith-Jones, K. D. Wittrup, N. V. Cheung and S. M. Larson, *European Journal of Nuclear Medicine and Molecular Imaging* **2016**, *43*, 925-937.
- [40] S. H. Frost, S. L. Frayo, B. W. Miller, J. J. Orozco, G. C. Booth, M. D. Hylarides, Y. Lin, D. J. Green, A. K. Gopal, J. M. Pagel, T. A. Back, D. R. Fisher and O. W. Press, *PLoS One* **2015**, *10*, e0120561.
- [41] O. Keinanen, K. Fung, J. M. Brennan, N. Zia, M. Harris, E. van Dam, C. Biggin, A. Hedt, J. Stoner, P. S. Donnelly, J. S. Lewis and B. M. Zeglis, *Proceedings of the National Academy of Sciences U S A* **2020**, *117*, 28316-28327.
- [42] G. Liu, *Frontiers in Pharmacology* **2018**, *9*, 1476.
- [43] C. P. Ramil and Q. Lin, *Chemical Communications (Cambridge)* **2013**, *49*, 11007-11022.
- [44] B. Dervaux and F. E. Du Prez, *Chem. Sci.* **2012**, *3*, 959-966.
- [45] P. V. Chang, J. A. Prescher, E. M. Sletten, J. M. Baskin, I. A. Miller, N. J. Agard, A. Lo and C. R. Bertozzi, *Proceedings of the National Academy of Sciences U S A* **2010**, *107*, 1821-1826.
- [46] J. M. Baskin, J. A. Prescher, S. T. Laughlin, N. J. Agard, P. V. Chang, I. A. Miller, A. Lo, J. A. Codelli and C. R. Bertozzi, *Proceedings of the National Academy of Sciences U S A* **2007**, *104*, 16793-16797.
- [47] D. H. D. Jennifer A Prescher, Carolyn R Bertozzi, *Nature* **2004**, *430*, 873-877.
- [48] K. N. a. M. W. Brechbiel, *Cancer Biotherapy and Radiopharmaceuticals* **2009**, *24*.

[49] J. Li, Y. Hu, J. Yang, W. Sun, H. Cai, P. Wei, Y. Sun, G. Zhang, X. Shi and M. Shen, *Journal of Materials Chemistry B* **2015**, 3, 5720-5730.

Potential of MRI in Radiotherapy Mediated by Small-Conjugates and Nanosystems

2



Introduction

Radiotherapy (RT) has become an indispensable tool in oncology, representing non-surgical treatment by cytotoxic ionizing radiation with the ability to destroy cancerous cells. One of the main objectives of a successful treatment is an accurate delivery of a correct therapeutic dose to the target while avoiding radiation exposure of the surrounding healthy tissues. This requires careful delineation of tumor by detecting its extension as well as assessing morphology, physiology, and biochemistry prior to therapy. All this information is gathered typically within the radiotherapy treatment planning (RTP) practice, which basically includes collective efforts by radiation oncologists, physicians, and radiologists for determination of the appropriate RT procedure, be it application of external radiation beams, internal brachytherapy or prescription of internal radionuclide therapeutics. Modern medical imaging is a valuable aid for RTP, and for many years computed tomography (CT) was considered the most suitable imaging modality based on its accessibility and high precision in determination of geometrical target parameters necessary for accurate external irradiation, and tissue electron density for the dose calculation. However, its poor soft-tissue contrast is in many cases limiting the spatial accuracy, which is important for the correct determination of tumor margins, especially when cancer is in the proximity to the vital organs. Another concern in external RT is patient misalignment as a result of internal motions, such as swallowing, respiration or muscle contraction/relaxation. Again the insufficient depiction of soft-tissues in radiographic images forms a serious drawback that requires calling in of complementary imaging techniques.

Magnetic resonance imaging (MRI) overcomes the aforementioned limitations due to its superb temporal and spatial resolution, and excellent soft-tissue contrast. As a non-invasive imaging modality without implication of ionizing radiation, it relies on the observation of water molecule protons, based on their density and relaxation dynamics. Altogether, these parameters lead to visualization of the differences in tissues by generation of either T_1 - (positive/bright) or T_2 -weighted (negative/dark) contrast. Thereby, tailored MRI pulse-sequences enable various types of contrast for functional and volumetric assessment of tumors, with the possibility for unlimited multiplanar image reconstruction. Furthermore,

dynamic contrast-enhanced MRI offers the possibility to monitor the signal in a tumor over time with rapid (\pm every 3 s) 3D-imaging using T_1 -weighted sequences.^[1] The methods for data acquisition in MRI allow for slice orientation in sagittal, coronal or any other convenient angle for better alignment with anatomy, compared to transaxial CT. Concerning assessment of functional tumor parameters, blood oxygenation level-dependent (BOLD) MRI can be used to visualize tumor hypoxia, which is one of the predictors of patient response to radiotherapy.^[2] From the instrumental point of view, systems integrating MRI and a linear accelerator are being developed and tested in the clinic with the goal to improve definition and geometrical calibration of tumors and to enable simultaneous irradiation^{[3],[4]}.

With all the above-mentioned advantages, MRI suffers from intrinsic lack of sensitivity that can be circumvented by administration of contrast agents (CAs), which are typically either small paramagnetic Gd(III)- or Mn(II)-complexes or superparamagnetic iron oxide nanoparticles (SPIONs) that shorten T_1 or T_2 relaxation times of surrounding protons, respectively. The effectiveness of CAs is expressed in relaxivity (r_1 or r_2), defined as the rate of increase of the corresponding relaxation time per mM of metal ion. The relaxivity enhancement is then either the result of dipolar interactions between the paramagnetic center and the protons in its vicinity, or perturbation of magnetic field around superparamagnetic center, which translates into the generation of high-resolution T_1 or T_2 contrast, respectively.

All these features substantiate the importance of MRI as a technique complementary to CT for its application in RTP^[5] and open perspectives for this imaging modality to serve as a platform for new types of agents for combined imaging and therapy, called theranostics.^[6] This review focuses on the role of MRI for different types of RT (Figure 2.1) and surveys the most important types of MRI CAs that have been developed to enhance the effects of external RT, enable monitoring of delivery and distribution of the internal radiotherapeutics, and evaluate the therapeutic outcome.

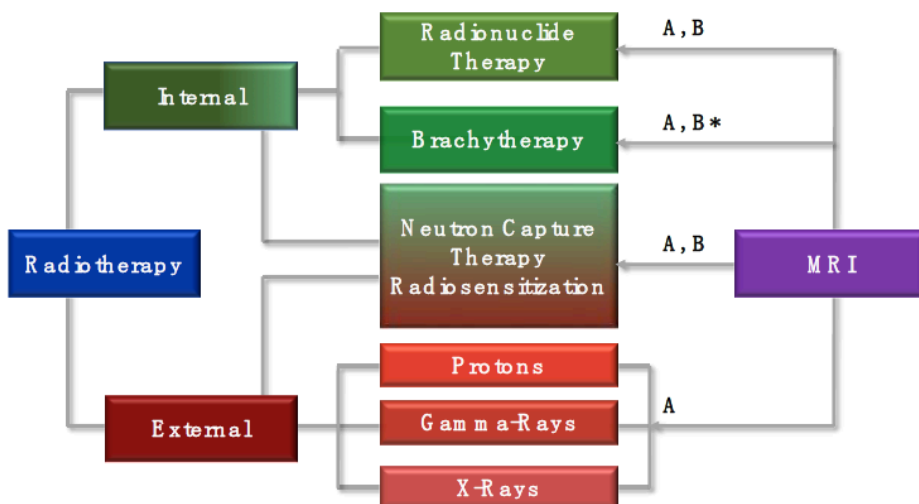


Figure 2.1. Overview of radiotherapeutic methods and the role of magnetic resonance imaging (MRI) in: (A) treatment planning, including volume of interest delineation and (B) monitoring delivery and distribution of therapeutic agents (* = only for non-sealed source brachytherapy).

The role of MRI in External Radiation Therapy

The essence of external radiation therapy (ERT) is the exposure of the patients to ionizing radiation originated from the beams (photons, high-energy electrons, protons or neutrons) produced by linear accelerators, cyclotrons or nuclear reactors. The treatment requires methods to decrease healthy tissues risk, i.e., delivery of the therapeutic dose exclusively to the site of interest. This precision matter involves several strategies, one of which is adjustment of the dose distribution in and around the tumor known as intensity-modulated radiation therapy (IMRT).^[7] In this type of ERT, multiple beams directed to the tumor are modulated in a way to intentionally deliver non-uniform intensity. Other exciting applications are stereotactic radiosurgery (SRS) and stereotactic body radiotherapy (SBRT), both of which are types of ERT initially designed to treat small brain tumors with a high precision of 1–2 mm. Thereby, 3D-imaging techniques are used not only to locate and describe the tumor but also to design radiation beams to cover the target area from different angles and plans, which implies careful patient positioning for the RT session. In all the aforementioned techniques, accurate determination of tumor margins and

morphology is the key factor, which can typically be achieved with CT. However, in many cases, such as brain or head/neck tumors, the full extent of the tumor can often only be fully visualized by an additional MRI scan on the basis of voxel to voxel matching resulting in a CT-MRI fused image. The study by Emami et al. is, thereby, a good example that shows a significant difference of the tumor volume obtained from the CT images compared to MRI (74% increase), which consequently leads to underdosing of the applied radiation by 14%.^[8] Another approach to minimize the damage of healthy tissues and enhance the effects of ERT involves the application of radiosensitizers, which are typically therapeutically inert (with exception to chemotherapeutic examples)^[9] compounds that increase susceptibility of cells to ionizing radiation and thus improving the dose efficacy.^[10] The effect is based on the particular physical properties of radiosensitizers such as high density and high atomic number (Z) of the comprising elements (*vide infra*). An additional benefit can be gained by providing these agents with the ability to generate an accompanied MRI signal that allows for visualization of the delivery of such theranostic probes to the site of interest as well as monitoring the effects of RT.

Radiosensitization

While careful definition of tumor size, shape and volume can to a certain extent be secured by high-resolution CT or MRI 3D-imaging, increasing the tumor-killing efficiency can be optimized by radiosensitive substances, which either result in additional boost in radiation dose (e.g., Au nanoparticles) or in biologically driven decrease in radiation resistance (e.g., kinase inhibitors). Generally, exposure of a soft tissue to ionizing radiation such as gamma- or X-rays as well as alpha-, beta-particles or electron, proton or neutron beams, causes a cascade of events leading to cell death. In this process, radiation beams, depending on their linear transfer energy, interact with DNA either directly or through the formation of free radicals originating from intracellular water molecules and dissolved oxygen. Metal-based radiosensitizers delivered to the target site are able to create differences between healthy and cancer cells rendering the latter more vulnerable to radiation, which, in turn, affects their proliferation and leads to apoptosis. The principle is based on the high density and high atomic number of the elements composing these agents. In response to irradiation,

the electrons of these elements absorb the energy, which is then transformed into kinetic energy sufficient to extract them from the atomic orbitals causing scattering of (fluorescent) photons and photo-, Compton-, or Auger-electrons. The type of effect is mainly determined by the Z/E ratio (Z = atomic number, E = energy of the incoming radiation), where E on its turn defines the range of the effect within the tissue. This phenomenon drew attention for the first time during RT treatment of mandibular cancer patients with high- Z material implants^[11] and was demonstrated later for iodine-containing contrast media with radiosensitizing effect on cultured mammalian cells.^[12] The most thorough investigation over the last decades, however, was done with high- Z elements, such as gold and mainly in the form of nanoparticles (NPs).

The general advantage of NPs is their ability to permeate tumor tissues through the leaky vasculature, an effect known as enhanced permeability and retention (EPR), often addressed as passive targeting.^[13] The result of such accumulation is slow systemic clearance compared to low-molecular agents, which prolongs the radiosensitizing effect. Additionally, the surface of NPs can be exploited for grafting of various functionalities, for example with polyethylene glycol (PEG) chains that reduce the uptake and removal of NPs by the reticuloendothelial system.^[14] Densely packed metal NPs possess higher mass absorption coefficients than those of soft tissues and high scattering cross-sections, which upon irradiation causes release of short-path-length photoelectric and Auger-electrons that induce the localized damage through the formation of free radicals. Gold nanoparticles (AuNPs) represent one of the most important class of radiosensitizing materials demonstrated first by Hainfeld et al.^[15] Applied in EMT-6 mammary carcinoma tumors implanted in mice, AuNPs of 1.9 nm diameter were delivered intravenously prior to 250 keV X-ray therapy enhancing the outcome. Next to excellent biocompatibility, a valuable additional property of AuNPs is their ability to generate contrast in CT enabling delineation of tumors. However, this review intends to focus on MRI-guided radiotherapy, and therefore, the main accent is on combination of radiosensitizing and magnetic properties of the agents.

Gadolinium-based radiosensitization

Gadolinium can be considered as the most exciting element envisioned for the combination of MRI with radiosensitization due to its strong paramagnetic nature and high mass-absorption coefficient thanks to its relatively high atomic number ($Z_{\text{Gd}} = 64$). The paramagnetic properties are due to seven unpaired electrons in the f-shell with rather long relaxation times. Coordination numbers of 8–9 and strong complexing properties underlie its wide application as clinical T_1 MRI CA in the form of small complexes with DOTA- or DTPA-like chelates (DOTA = 1,4,7,10-tetraazacyclododecane-1,4,7,10-tetraacetate; DTPA = diethylenetriamine pentaacetic acid) with high thermodynamic and kinetic stabilities. The parameters governing the efficiency of low-molecular Gd-based MRI CAs are extensively discussed in the literature.^[16] Numerous studies over the last two decades have been dedicated to the design of Gd(III)-complexes with modulated number (q) and residence time (τ_M) of water molecules in the first coordination sphere and the rotational correlation time (τ_R) of the complex in order to increase the r_1 . Recently, an important safety concern has been raised in connection with possible release of toxic “free” Gd(III)-ions *in vivo* causing nephrogenic systemic fibrosis^[17] or their accumulation in the central nervous system.^[18] Therefore, every new design of a potential MRI CA molecule towards increased r_1 by optimization of the aforementioned parameters by chemical modifications requires thorough evaluation of the thermodynamic and kinetic stabilities of the final complex.

A small Gd(III)-complex designed for radiosensitization combined with MRI is porphyrin-like macrocycle motexafin gadolinium (MGd) (Figure 2.2) that belongs to the texaphyrins class of drugs, which proved effective to mediate radiation of tumors and brain metastasis in particular.^[19] A pre-clinical MRI study has revealed a selective uptake of MGd by malignant cells, most probably facilitated by the tumor pH being lower compared to those of healthy cells. A nine-fold contrast enhancement within 24h post-injection (*p.i.*) into murine mammary tumor mice models was accompanied by the rapid clearance from plasma through the bowel.^[20] The therapeutic effect is based on several mechanisms, including depletion of intracellular reducing metabolites, such as ascorbate, glutathione and NADPH

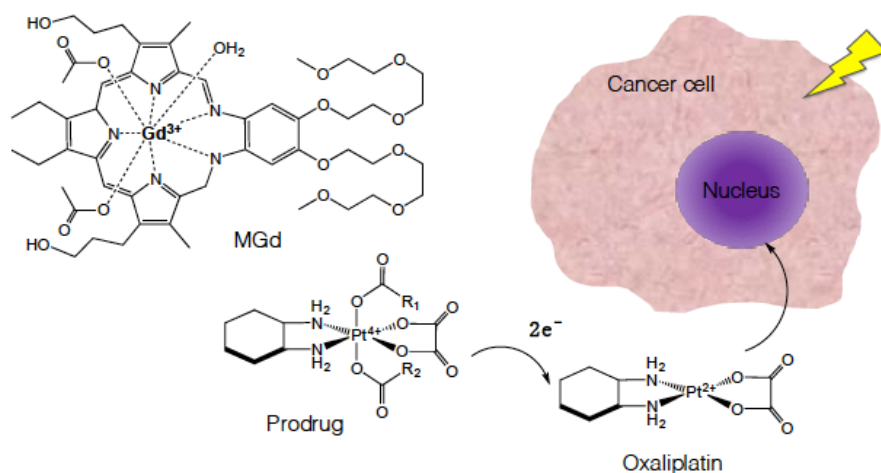


Figure 2.2. Schematic representation of synergistic effect of motexafin gadolinium (MGd) accumulated at the tumor cells with chemotherapeutics upon photo-irradiation. Pt(IV) prodrugs vary as: R₁/R₂ = CH₃, R₁/R₂ = CH₂CH₃, R₁/R₂ = (CH₂)₂COOH, or R₁ = (CH₂)₂COOH, R₂ = CH₃.^[21]

that are typically taking part in repair of oxidative DNA damage upon irradiation. Additionally, MGd was shown to exhibit a synergistic effect in combination with some chemotherapeutics. An example is reduction of platinum (IV) prodrugs to their active form oxaliplatin (Pt(II)) by the metabolites, such as sodium ascorbate, generated upon photo-irradiation in the presence of MGd accumulated selectively at the tumor.^[21]

In general, the strategies to enhance the MRI performance of *T*₁ CAs include either accommodation of multiple Gd(III)-complexes on nanocarriers or application of Gd-containing NPs; both concepts striving for a higher payload of paramagnetic units increasing the *r*₁ per Gd(III)-ion.^[22] Development of a polyol method for the synthesis of crystalline core Gd₂O₃ NPs^[23] within the size-range of 1-5 nm enabled a series of studies that demonstrated higher *r*₁ (8.8 s⁻¹ mM⁻¹ vs. 4.1 s⁻¹ mM⁻¹ of Gd(III)-DOTA) based on the additional contribution of Gd-ions located inside the core.^[24] In terms of radiosensitization, densely packed NPs show an increased ability to scatter/absorb the X-rays and gamma radiation that leads to more localized damage of targeted cancer cells. Lux and co-workers have developed an original top-down process for the preparation of ultrasmall Gd-NPs with a size below 5 nm,

convenient for *in vivo* circulation and renal clearance.^[25,26] The method consisted of several steps, starting with the initial preparation of Gd₂O₃ core, which was then encapsulated into a polysiloxane shell that was conjugated with DOTAGA (1,4,7,10-tetra-azacyclododecane-1-glutaric anhydride-1,4,7,10-triacetic acid) ligands. The subsequent dissolution of the core has led to chelation of the released Gd(III)-ions by the ligands and defragmentation of the shell yielding ultrasmall NPs (Figure 2.3A). The stability of the resulting complexes ($\log \beta_{110} = 24.8$), was found to be very close to that of DOTA ($\log \beta_{110} = 25.6$), while the r_1 measured at 60 MHz was $11.9 \text{ s}^{-1} \text{ mM}^{-1}$ per Gd(III). The intravenous injection of these NPs into gliosarcoma-bearing rats resulted in a swift accumulation (~ 10 min) in the tumor through the EPR effect. The MRI data was used to determine the timepoints for the subsequent application of microbeam radiation therapy (MRT). Accumulated at the tumor, Gd-NPs acted as radiosensitizers upon irradiation and the therapeutic effect was demonstrated by the different median survival of the MRT-treated animals with (48 days) and without (20 days) administration of NPs (Figure 2.3B–D). An additional application of these NPs was demonstrated by intratracheal administration for MRI visualization of lung cancer, which was possible due to their small size (~ 3 nm) and hence the ability to pass through the pulmonary airways and be excreted later through the kidneys.^[27]

Further progress with these NPs has been made by incorporation of bismuth Bi(III) into DOTA-chelates on the surface of the aforementioned silica carrier with Gd/Bi ratio of 8/6.^[28] The presence of bismuth resulted in strengthening of radiosensitizing effect due to its high atomic number ($Z_{\text{Bi}} = 83$) and additional possibility to visualize the particles by CT. MRI monitoring of the arrival of the particles after intravenous injection into lung carcinoma-bearing mice was used to determine the right timing (30 min *p.i.*) for the delivery of 10 Gy radiation dose. Evaluation of double-strand DNA breaks for both tumor and healthy tissues was used as quantification of radiosensitizing effect, which eventually resulted in significantly higher survival rate for the animals irradiated after injection of Gd/Bi NPs.

Carbon quantum dots (CDs) represent another interesting nanopatform for MRI-guided radiosensitization. Doping of carbon crystals with Gd could be achieved through hydrothermal carbonization of Gd-DTPA in the presence of glycine as passivation agent resulting in a composite, resistant for Gd-leakage even under harsh conditions.^[29] The r_1

relaxivity of $6.5 \text{ s}^{-1} \text{ mM}^{-1}$, which was higher than that of Gd-DTPA ($4.5 \text{ s}^{-1} \text{ mM}^{-1}$), was attributed to the much larger hydrodynamic surface area of CDs ($\sim 20 \text{ nm}$) with Gd-ions in the lattice. The intravenous injection of Gd-CDs into a tumor-bearing mouse was followed by MRI, starting with passive accumulation and retention in the tumor and ending with the final renal clearance of the probe. The remarkable radiosensitizing efficacy was demonstrated in a single treatment of HepG2 cells by 8 Gy X-ray radiation leading to reduced growth by 90.1% and further shrinkage of the tumor by 53% in 7 days, compared to 12% for the group of mice irradiated in the absence of Gd-CDs.

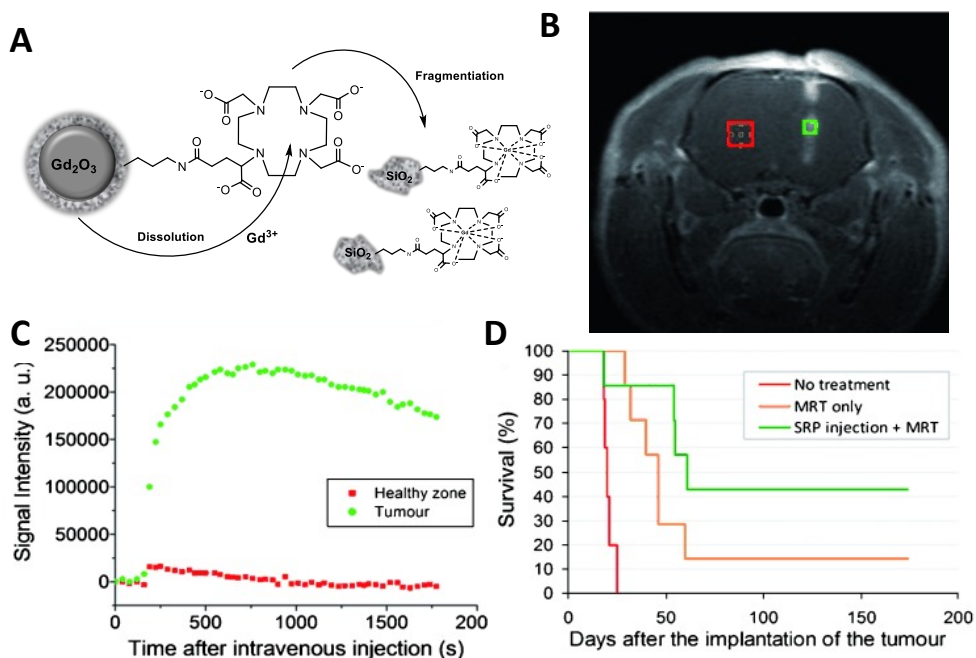


Figure 2.3. MRI/microbeam radiation therapy (MRT) study with Gd nanoparticles (NPs): (A) top-down process going from Gd_2O_3 coated with SiO_2 conjugated with DOTAGA (1,4,7,10-tetraazacyclododecane-1-glutaric anhydride-1,4,7,10-triacetic acid), followed by dissolution and complexation of Gd(III)-ions and fragmentation of ultrasmall NPs; (B) T1-weighted MR image of rat's brain overexpressing gliosarcoma tumor. Green and red area indicate tumoral and non-tumoral accumulation of NPs, respectively; (C) MRI signal obtained at 7T following accumulation of NPs in tumor and healthy zone over time; (D) animal survival rate without treatment and after application of dose rate of $90 \text{ Gy} \cdot \text{s}^{-1} \cdot \text{mA}^{-1}$ with and without administration of NPs.^[25]

Iron oxide Nanoparticles

The use of superparamagnetic iron oxide nanoparticles (SPIONs, mainly magnetite (Fe_3O_4) or maghemite ($\gamma\text{Fe}_2\text{O}_3$)) in medical field ranges from various types of therapies, such as targeted drug delivery, immunoassays, hyperthermia and tissue repair to diagnosis by MRI.^[30] The latter application relies on the ability of SPIONs to generate dark contrast promoted by magnetic domains within iron oxide crystals containing unpaired electrons. Gathered in one particle, the single-domains display a strong collective magnetic moment that results in magnetic susceptibility, disruption of external magnetic field homogeneity, and creation of field gradients. Consequently, the transversal relaxivity of water molecules diffusing in the vicinity of SPIONs is reduced significantly, leading to a T_2 -weighted contrast, while the emerged field inhomogeneities induce a T_2^* -weighted contrast.^[31] Intracellular delivery of SPIONs is to a great extent determined by the size of the particles as well as functionalization of their surface with various coatings and conjugated vectors for increased affinity towards certain pathological epitopes. These features of SPIONs along with the available facile manufacturing methods have led to many interesting formulations for labeling and *in vivo* MRI-tracking of stem cells, imaging of apoptosis and inflammation.^[32] In general, the small size of the particles allows them to penetrate small capillaries and be captured and retained by the affected cells. Using SPIONs as drug delivery systems carrying conjugated chemotherapeutics, such as e.g., methotrexate that can be cleaved from the surface under intracellular conditions, represents an interesting strategy, especially when the process can be monitored by MRI.^[33] Medarova et al. have demonstrated a possibility to track tumor response for chemotherapy by application of SPION's decorated with peptides for recognition of mucin-1 tumor-specific antigen (uMUC-1) attached to their crosslinked dextran coating. MR images acquired on mice with pancreatic adenocarcinomas clearly indicated alteration of T_2 -weighted contrast before and after the treatment with the chemotherapeutic agent 5-FU.^[34]

The multifunctional potential of SPIONs is currently being extended to radiosensitization applications (Table 2.1), despite the less convenient characteristics of iron ($Z_{\text{Fe}} = 56$, X-ray absorption enhancement factor (AEF) = 1.2) compared to gold ($Z_{\text{Au}} = 79$, AEF = 1.6).

Radiosensitization typically occurs due to interaction between high Z-materials and low energy X-rays (keV-range) through photoelectric effects, while at higher energies Compton effects are dominating. Therefore, the shift to the megavoltage range can be seen as beneficial for clinical applications due to skin sparing and convenient dose-distribution to the deep-seeded tumors, such as in case of colon cancer.^[35] Recent studies revealed that the radiosensitizing effect of dextran-crosslinked SPIONs exposed to 6 MeV X-rays might be both concentration and dose-rate dependent with the optima observed at 80 $\mu\text{g}/\text{mL}$ and 370 cGy/min, respectively.^[36] Another study by Khoei et al. with human prostate carcinoma DU145 cell line demonstrated that coating of particles with dextran with additional amino-groups increases the cellular uptake significantly compared to plain particles (only dextran-coating). As the result, the best MRI enhancement by NH_2 -dextrane-SPIONs was observed for the concentration of 1 mg/mL and the radiosensitization effect was found to be dose-independent under MeV energies.^[37]

Table 2.1. Examples of SPIONs applied as radiosensitizing MRI contrast agents.

Composition/ Coating	Preparation Method	Size (nm)	Radiation Energy	Cell Line	Tested Application	Ref.
$\text{Fe}_3\text{O}_4/\text{dextran}$	Co-precipitation	15	6 MeV	MCF-7/HeLa	ERT	[36]
SPIONs/dextran- NH_2	— ¹	130	6 MeV	DU-145	ERT/MRI	[37]
$\text{Fe}_2\text{O}_3/\text{Fe}_3\text{O}_4/\text{citrate}$	Co-precipitation ³	6-20 ² 3-10 ³	120 keV	MCF-7	ERT	[38]
SPIONs/citrate	Co-precipitation	6-25	6 MeV	MCF-7/MDAH-2447/MDA-MB-231	ERT	[39]
BiFeO_3	Sol-gel	30	160 keV	MCF-7	MRI/ERT/CT/HT	[40]
$\text{Fe}_3\text{O}_4/\text{Ag}/\text{C}225$	Co-precipitation	102	6 MeV	CNE	ERT	[41]
$\text{Fe}_4[\text{Fe}(\text{CN})_6]^{3-}$ $\text{Au}/\text{citrate-PEG}$	Electrostatic absorption	139	—	4TI	MRI/CT/PTT/ERT	[42]

¹ Commercially available; ² 0 °C; ³ 220 °C.

The necessity of an appropriate coating of the metal core, which applies for any NPs envisioned for *in vivo* applications, becomes particularly interesting in case of SPIONs. Next to decreased toxicity by ion-leakage inhibition, the arguments for coating are surface passivation, prevention of aggregation and interaction with reticuloendothelial system. All these measures ultimately lead to prolonged blood-circulation time and increase the chance

for accumulation at the site of interest. The choice of coating materials, in addition to influences on the aforementioned parameters, has a dramatic effect on the MRI performance of SPIONs. For instance, coating of the core of the SPIONs with carboxylates leads to a drop of net magnetization and the consequent decrease of the T_2 -effect, which is not observed in case of phosphate coating.^[43] On the other hand, the presence of hydrophilic molecules promotes a greater hydration around the particles and results in higher relaxivity of surrounding protons. The role of the chain length of coating polymers on the r_2 relaxivity is determined by the access of water molecules to the metal core. Generally, long PEG-chains tend to reduce relaxivities due to prohibition of diffusing water molecules from contact with the magnetic core. However, when PEG is anchored to SPIONs in a single layer, water molecules are not excluded from such interactions and high relaxivities can be achieved even with smaller particles based on slow diffusion and hence more efficient dephasing of magnetic moments.^[44]

Interesting results have been obtained by Klein et al. who have studied the effects of coating density on the radiosensitization properties of SPION's.^[38] The intrinsic toxicity of SPIONs is based on generation of oxygen reactive species (ROS), such as H_2O_2 , $\cdot OH$, $HO_2\cdot$, and O_2^- that are produced upon release of iron ions from particles endocytosed into tumor cells. Application of SPIONs that are partially coated with citrate induced cooperative toxicity under X-ray irradiation, resulting in enhancement of radiosensitizing effect due to increase of ROS formation by 240 %. Thereby, the effect was found to be more pronounced in case of SPIONs containing both maghemite and magnetite domains (high-temperature preparation) compared to SPIONs containing maghemite only (low-temperature preparation). *In vitro* studies on three types of human carcinoma cell lines (ovarian, breast estrogen receptor positive and negative) incubated with the same amount of citrate coated SPIONs and exposed to 6 MeV X-rays showed that the best AEF could be achieved at 2 and 4 Gy for the first two and the latter cell line, respectively.^[39] Moreover, no further radiosensitization effect enhancement was found above 8 Gy, which means that irradiation can be done at low doses adopted for specific tumor cells.

Combination of iron with other metals was also explored for theranostic purposes. Rajae et al. considered Bi as a more efficient radiosensitizer due to its higher atomic number (Z_{Bi}

= 82), while keeping the benefits of combination of high photoelectric absorption and magnetic properties of iron^[40]. Bismuth ferrite nanoparticles (BiFeO_3) of the size ~ 30 nm, prepared by the sol-gel method using equal amounts of Bi and Fe, displayed excellent MRI properties in addition to CT contrast due to the high density of Bi. Furthermore, the BiFeP_3 particles showed response to inductive heating at 480 kHz enabling their applicability as magnetic hyperthermia (HT) mediators, which is considered advantageous for improved efficacy of radiotherapy.^[45] Another group investigated synergetic MRI/ERT performance of SPIONs combined with silver ($Z_{\text{Ag}} = 47$) in a single particle.^[41] In this study, Fe–Ag NPs were conjugated to an epidermal growth factor (EGFR) receptor-specific monoclonal antibody (C225) currently applied in the clinic for the treatment of advanced brain tumors. The researchers demonstrated 80% inhibition of proliferation of carcinoma cells (CNE) in the presence of 8 mg/L of nanocomposite and down-regulation of EGFR, but most importantly, the accompanying enhancement of sensitivity of CNE to X-ray irradiation by 2.3-fold. Dou et al. have doped clinically applied cubic shaped (83 nm) Prussian Blue NPs with AuNPs (13 nm) via electrostatic adsorption^[42]. After PEGylation, the final nanocomposite (138 nm) injected intravenously into 4T1 xenograft bearing mice was observed by MRI (both T_1 - and T_2 -weighted images) and CT (gold-contrast) showing accumulation at the tumor site after 24h *p.i.* Further exposure of the tumor-bearing animals to both photothermal therapy (PTT) by near-infrared (NIR) treatment (heating of tissues up to 55 °C in the presence of iron) and X-ray irradiation showed reduction of tumor volumes by $\sim 94\%$, compared to 39% and 47% of each individual therapy, respectively. The results were correlated with the ability of RT to reach deeply located cancer cells, while PTT increases the sensitivity of the radio-resistant hypoxic cells to X-ray irradiation.

The role of MRI in Internal Radionuclide Therapy

Internal radionuclide therapy (IRT) is gaining increased attention as a type of cancer treatment shown to increase life expectancy for terminal patients up to several years with a good quality of life^[46]. Regarding the application of radiation emitting nuclides, the main advantage of IRT is the delivery of a highly concentrated radiation dose to metastasized malignancies otherwise untreatable by external radiation beams, such as bone metastases.

Radiolabeled molecules used for this treatment are often referred to as radiotherapeutics or radiopharmaceuticals. Physical properties of the constituting radionuclides, e.g., half-life, type of emission, energy, possible daughter nuclides, and production routes, are the first determinants in the radionuclide choice for every particular therapy or palliation treatment.^[47] However, the biochemical characteristics of radiopharmaceuticals, such as their biological half-life and tumor uptake, retention, and clearance mechanisms also play an important role. The ability of selective delivery of radiotherapeutics to the tumors as well as fast clearance is decisive for their safety as well as the final therapeutic outcome. To achieve this, the current strategies include exploitation of metabolic pathways (e.g., accumulation of ^{131}I in thyroid cancer,^[48] targeting overexpressed receptors or antigens by radiolabeled peptides or monoclonal antibodies ^[49]), and natural uptake of bone-seeking radiopharmaceuticals.^[50] The most important examples of therapeutic radionuclides and their physical properties are listed in Table 2.2. More detailed description can be found elsewhere;^[51] here we focus on specific examples of MRI contrast agents designed for combination with IRT.

A special type of IRT is represented by interstitial brachytherapy in which a radiation source is sealed in a small seed (mm) that is placed directly into a tumor (typically prostate) under anesthesia. Depending on the intended dose, the treatment can vary from a few minutes (high-dose rate) to a few days (low-dose rate). In some cases, the seeds can even be left in place permanently. MRI certainly plays an important role prior to the treatment planning,^[52] but there are currently no examples of sealed radiation sources with additional MR imaging properties. The potential of MRI in combination with internal radiotherapy is most evident in studies applying ^{166}Ho -containing microspheres.^[53] These radioactive microspheres are used primarily for liver radioembolization, but their application can be extended to intratumoral treatments as a promising new brachytherapy method. The polymeric microspheres contain ^{165}Ho , part of which is converted to ^{166}Ho upon neutron activation. The ^{166}Ho with its convenient half-life of 26.8 h, has a maximum β -energy of 1.9 MeV, applicable to kill tumors, as well as a gamma emission of 81 keV, suitable for single photon emission computed tomography (SPECT) imaging. Furthermore, the magnetic moment of ^{165}Ho , being one of the highest among the whole series of lanthanides (10.6 μB), enables

simultaneous monitoring of the therapeutic events by T_2 -weighted MRI.^[54] In the clinical study by Smith et al. a total of 15 patients excluding those having surgical clips (to avoid interferences in the MRI evaluations) were evaluated.^[55] The SPECT and MRI data obtained showed high correlation, which however raised some questions in terms of dosimetry. The high resolution of MRI is undoubtedly superior for collection of dosimetric data in small areas, but when the microspheres are located near the organs containing air, such as lungs, the susceptibility artefacts of MRI lead to decreased accuracy of the method. The authors concluded that although a direct comparison between SPECT and MRI is difficult, the two techniques are complementary to each other and MRI had the advantage of providing biodistribution long after the activity of ^{166}Ho had decayed allowing for better post-treatment evaluation (Figure 2.4). The added value of MRI was also evaluated in intratumoral injections of the ^{166}Ho microspheres in lab animals having orthotopic renal tumors. The results showed that combination of the high sensitivity of SPECT and the high-resolution soft-tissue contrast of MRI was beneficial in assessment of the distribution of the microspheres within the tumor to ascertain proper tumor coverage.

Another potential for MR-assisted IRT lies in the application of SPIONs radiolabeled with therapeutic radionuclides. The first example is radiolabeling of NPs with ^{188}Re (half-life of 17 h and maximum β -energy of 2.1 MeV), which is one of the radionuclides used routinely in the clinic. Production through $^{188}\text{W}/^{188}\text{Re}$ -generator, convenient in clinical environment, has already stimulated development of several ^{188}Re -radiolabeled biomolecules. Several SPIONs platforms coated with silica,^[56] human serum albumin,^[57] polyacrylamide^[58] or prepared within apoferritin cavities^[59] have been explored for the application in magnetically targeted radiotherapy. The rationale behind this approach is to profit from the localized magnetic field gradients to attract the NPs to the tumor for the subsequent radiotherapy. The radiolabeling yield and *in vitro* stability of the NPs prepared in the aforementioned studies are high, and even though the MRI performance of these materials has not been investigated in particular, its potential certainly exists and can be explored for radiotheranostic purposes.

Table 2.2 Most important radionuclides for internal radionuclide therapy (IRT).

Radio-nuclide	Half-life	Decay Mode	Soft Tissue Range (mm)	Product	Most Common Clinical Application ¹
¹⁶⁶ Ho	26.8 h	β-	8.5	¹⁶⁶ Er	Hepatic cancer ^[54]
¹⁸⁶ Re	3.7 d	β-/ε	3.6	¹⁸⁶ Os/ ¹⁸⁶ W	Bone metastasis, arthristis
¹⁸⁸ Re	17.0 h	β-	11.0	¹⁸⁸ Os	Bone metastasis, arthristis ^[59]
⁸⁹ Sr	50.6 d	β-	8.0	⁸⁹ Y	Bone metastasis
¹⁷⁷ Lu	6.7 d	β-	1.7	¹⁷⁷ Hf	Various cancer
⁹⁰ Y	64.6 h	β-	11.0	⁹⁰ Zr	Hepatic metastasis ^[60]
¹⁵³ Sm	46.3 h	β-	3.4	¹⁵³ Eu	Bone metastasis
¹⁶⁵ Dy	2.3 h	β-	5.7	¹⁶⁵ Ho	Rheumatoid arthritis
³² P	14.3 h	β-	7.9	³² S	Cystic craniopharyngioma
²²³ Ra	11.4 d	α	0.01	²¹⁹ Rn	Bone metastasis
¹³¹ I	8.0 d	β-	2.4	¹³¹ Xe	Thyroid cancer, neuroblastoma ^[61,62]
¹²⁵ I	59.4 d	γ/ε	17.0	¹²⁵ Te	Brachytherapy of prostate cancer, postsurgical treatment of brain cancer, uveal melanoma ^[62]

¹ The references are given for the existing studies demonstrating potential for combination IRT with MRI.

In the next example, the magnetite SPIONs were radiolabeled with ⁹⁰Y,^[60] which is a high energy β-emitter (2.27 MeV) with a half-life of 64.1 h, known to affect the tumors at a maximum depth up to 10–11 mm due to the ability of β-radiation to cross multiple individual cells. Targeting of tumor cells with this radionuclide is, therefore, not strictly necessary, provided that accurate accumulation of the particles in tumors can be performed and monitored by MRI. In this study, ⁹⁰Y labeling was successfully achieved with either naked- or PEG₆₀₀-coated Fe₃O₄-NPs. In the case of naked NPs, the surface (≡FeOH) was deprotonated at pH > 6.2 (≡FeO⁻) to enable stable electrostatic interaction with ⁹⁰Y(III)-ion, yielding 97% radiolabeling. Radiolabeling of PEGylated NPs was possible due to their carboxylate-rich surface interacting with positively charged tracer leading to 99% yield. Both types of particles exhibited superparamagnetic behavior at room temperature, which was considered suitable for *in vivo* hyperthermia under clinical magnetic field frequency of 580 kHz. The biodistribution studies in healthy Wistar rats showed a substantial accumulation of NPs in liver and lungs. The latter uptake was particularly high in case of non-PEGylated ⁹⁰Y-Fe₃O₄ NPs due to *in vivo* agglomeration, while PEGylated analogues exhibited longer blood-circulation time, and were therefore, considered suitable for β-therapy of liver malignances with additional visualization by MRI.

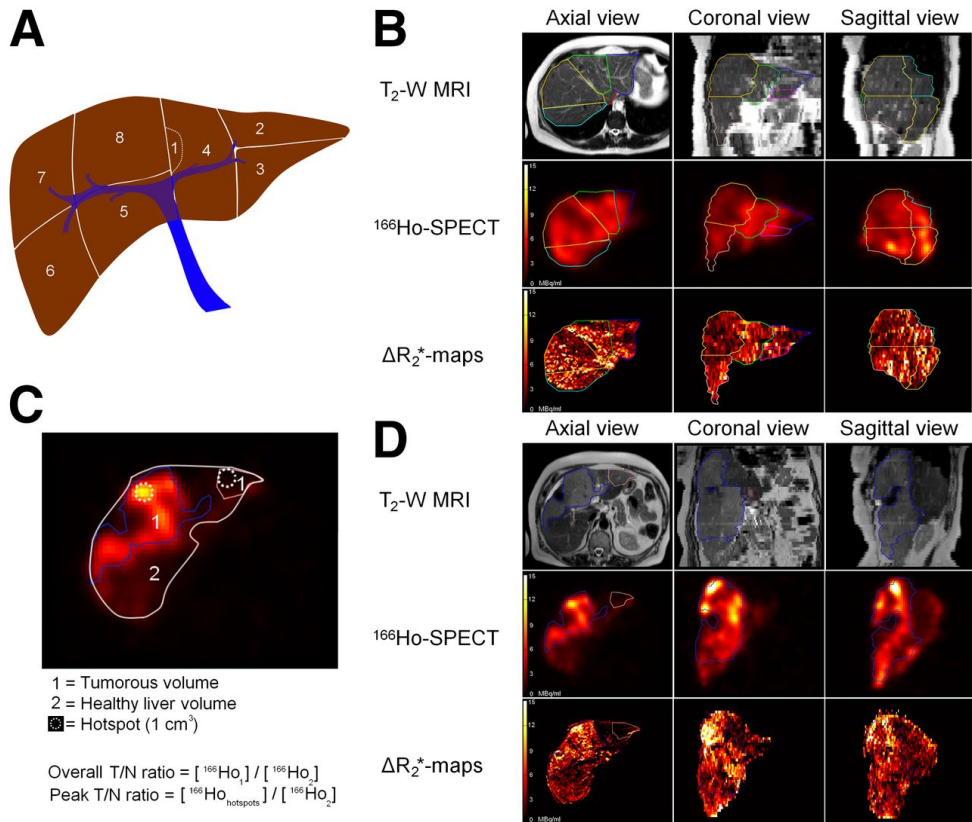


Figure 2.4. Single photon emission computed tomography/magnetic resonance (SPECT/MR) imaging of ^{166}Ho -microspheres for treatment of liver cancer: (A) schematic overview of liver segments; (B) delineation of liver segments on T_2 -weighted MR images (top row), volumes of interest (VOIs) registered to SPECT activity maps (middle row), ΔR_2^* -based activity maps for some set of VOIs; (C) schematic overview of created tumor VOIs and calculations of tumor-to-nontumor ratios and the fine distribution assessment; (D) delineation of tumors.^[54]

Labeling of MRI contrast agents with various radioisotopes of iodine offers advantages for multimodal imaging (SPECT (^{123}I), positron emission tomography (PET (^{124}I)), as well as biological research (^{125}I) and radiotherapy (^{131}I). Chen et al. came up with an integrative approach for gene therapy combined with IRT using commercial SPIONs (SilenceMag) designed for *in vivo* gene delivery and targeted cell transfection with nucleic acids, as nanocarriers and imaging reporters^[61]. The positively charged surface of these NPs interacts with negatively charged phosphate backbone of RNAs that can be then delivered to the target under application of external magnetic field (EMF). In this study, the authors

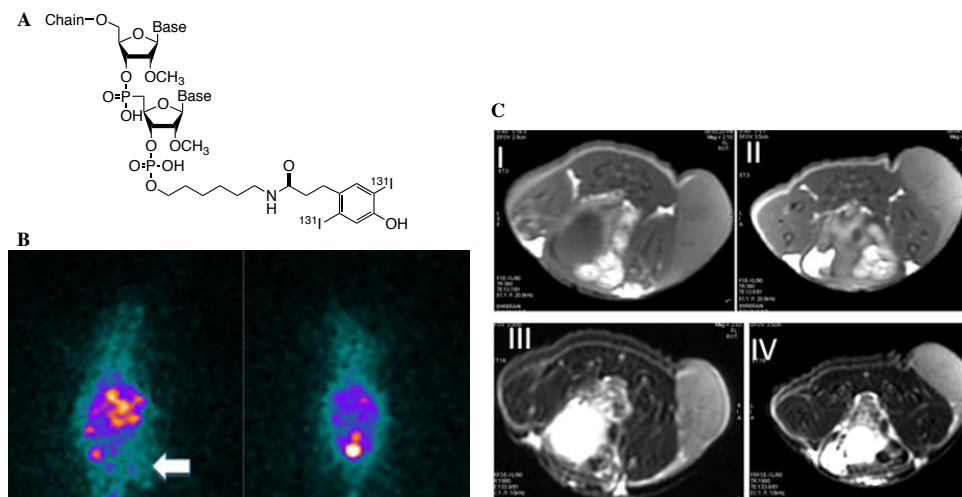


Figure 2.5. A) Structure of modified ^{131}I -labeled hVEGF siRNA used for conjugation with SilenceMag; Visualization of the probe 30 min p.i. into HepGr HCC bearing mice xenograft by B) scintigraphy and C) MRI in the presence (left) and absence (right) of EMF, applying T_1 - (I and II) and T_2 -weighting (III and IV).^[61]

aimed at targeting of hepatocellular carcinoma (HCC) cells known to overexpress vascular endothelial growth factor (VEGF) that correlates with progressive tumor growth. Prior to conjugation, the human VEGF siRNA was first modified chemically in order to (i) increase its biological half-life time and (ii) provide the molecule with a linker for the subsequent radiolabeling with ^{131}I -containing Bolton Hunter reagent (Figure 2.5A). Then the ^{131}I -hVEGF siRNA/SilenceMag NPs were injected into HCC bearing mice xenograft and prolonged blood-circulation in the presence of EMF (2.22 vs. 3.37 h) with a significant accumulation at the tumor site was demonstrated (Figure 2.5B).

Examination of the therapeutic effect of ^{131}I -hVEGF siRNA/SilenceMag revealed decreased final tumor weight with the inhibition rate of 49.8% and a dramatic decrease of VEGF protein expression. Localization of ^{131}I -hVEGF siRNA/SilenceMag using MR could be done by T_1 -weighted imaging visualizing the periphery of tumors, while T_2 -weighted imaging was surprisingly less effective (Figure 2.5C). This phenomenon was attributed to either a small amount of SilenceMag entering the tumor microenvironment or the inefficiency of SPIONs to create local field inhomogeneity and dephase magnetic moments of protons leading to

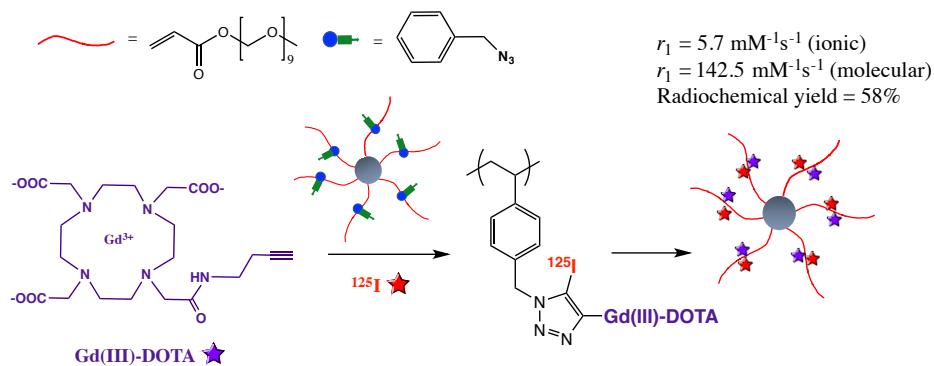


Figure 2.6. Synthetic strategy for the preparation of Gd(III)-DOTA star polymer NP radiolabeled with ^{125}I .

T_2 -shortening. However, the therapeutic efficiency of the probe due to the radiosensitizing effect allows for the assumption that application of the same radiolabeling strategy to SPIONs with physical properties optimized for MRI will enable synergetic radiotheranostic treatment of HCC.

An elegant approach for combination of MRI with IRT was proposed in a recent study^[62] reporting one-pot synthesis of a dendrimer-like star polymer conjugated with Gd(III)-DOTA and radiolabeled with ^{125}I (Figure 2.6). The presence of multiple paramagnetic chelates (25/molecule) and slow molecular dynamics endowed the NPs with high r_1 relaxivity promising for MR imaging. At the same time, efficient radiochemical yield (58%) enables the application of this probe for combined PET imaging, opening at the same time the possibilities for therapy either in the current form or by substitution of the radiolabel with ^{131}I .

Neutron Capture Therapy combined with MRI

The therapeutic nature of neutron beams^[63] and two decades later was demonstrated experimentally as a binary modality known today as neutron capture therapy (NCT). This approach combines the features of both internal- and external radiotherapies: in the first step, the patient is injected intravenously (IRT) with a non-radioactive compound that accumulates in the tumor, and then externally irradiated (ERT)

with epithermal neutrons in the second step. The principle relies on the ability of selected stable isotope to capture neutrons due to cross-sections many times higher than those of naturally present tissue elements. One of the successful applications of this methodology is boron neutron capture therapy (BNCT) that exploits non-radioactive isotope ^{10}B (20% natural abundance). Capturing of neutrons by ^{10}B yields excited $^{11}\text{B}^*$ that undergoes nuclear fission reaction releasing high linear energy transfer (LET) α -particles (^4He) and recoiling ^7Li nuclei, two products within the range of the cell diameter (5–10 μm) (Figure 2.7A). The efficacy of the therapy is to a great extent determined by the concentration of selectively delivered boron atoms: typically $\sim 10^9$ atoms/cell (or lower if located close to the cell nucleus)^[64]. In cases where the critical boron concentration is not reached, irradiation of the patient will only lead to undesired side-effects due to neutron capturing by endogenous elements, such as nitrogen and hydrogen. Sufficient retention at the tumor during the treatment, tumor-to-healthy tissues (3:1) and tumor-to-blood ratios (5:1), as well as adequate lipophilicity for efficient cross-over of the blood–brain barrier (BBB) and safe clearance, are other restraints for a successful BNCT probe. Provided that these conditions are met, the radiation dose to the tumor cells will be much higher than that in the surrounding health tissues, which renders BNCT especially suitable for locally dispersed tumors.

Boron delivery agents have passed through considerable development over the years.^[65] The first generation of simple borax compounds caused severe adverse effects, which could be slightly improved in the case of polyhedral decahydrodecaborate (Figure 2.7B), but the selectivity of these compounds towards tumors remained poor. Better results in terms of toxicity and specificity were achieved later with ^{10}B -enriched sodium mercaptoundecahydro-closo-dodecaborate (BSH) and l-boronophenylalanine (l-BPA), both applied in clinical trials. The latter compound has also been formulated as a complex with a fructose molecule for better solubility in water.

The search for a proper BNCT agent, however, has still not reached its optimum, which certainly hampers the application of this otherwise attractive therapeutic technique. Therefore, the possibility to evaluate the *in vivo* kinetics of potential BNCT agents by means of high-resolution imaging represents a valuable asset. The first attempts to visualize the

process was made by radiolabeling of BPA with ^{18}F for simultaneous PET imaging ^[66]. However, this method had disadvantages due to limited availability of the tracer and low resolution of PET. Therefore, conjugation of MRI reporters with either polyhedral or BPA boron-containing fragments represents a more elegant approach. One of the early examples of this approach is a Mn(II)-porphyrin complex bearing four carborane moieties (Mn(II)-BOPP, Figure 2.7C).^[67] The compound showed a good *in vivo* affinity towards gliomas and enabled assessment of biodistribution by T_1 -weighted MR imaging. Another group has exploited Gd(III)-DTPA complex for conjugation with both BPA and carborane functionalities for *in vivo* delivery of boron species to a hepatoma tumor that could be followed by MRI.^[68] However, the biodistribution of the conjugates appeared unfavorable compared to the native BNCT agents and the resulting boron concentration in the cells not sufficient for therapy. This problem was tackled later by the design of Gd(III)-DOTA-carborane (Figure 2.7C) with increased molecular weight due to supramolecular assembly with β -cyclodextrin and the consequent r_1 relaxivity of $15.5 \text{ mM}^{-1} \text{ s}^{-1}$ at 20 MHz. The therapeutic advantage of the probe was demonstrated by its ability to deliver up to $35 \mu\text{g}$ of boron per gram of B16 melanoma tissue within 4h p.i. and the subsequent decreased tumor growth after neutron irradiation.

An additional advantage of Gd, next to its superior paramagnetic properties, is the high neutron absorption cross-section of two of its natural isotopes ^{155}Gd and ^{157}Gd , with the value for the latter (255,000 barns) being 65× higher than that of ^{10}B . As the result, the same amount of Gd delivered to the tumor cells would result in a much higher rate of neutron absorption reactions, or better to say, the same therapeutic outcome could be reached with a lower integrated thermal flux and/or lower concentrations of the probe applied. Moreover, the delivery process can be monitored by MRI, which allows for personalized irradiation of the patients. Despite these benefits, Gd-NCT has not reached the clinics mainly due to secondary radiation effects intrinsically different than those in BNCT. The neutron capturing reaction of ^{157}Gd leads to excited $^{158}\text{Gd}^*$ accompanied with prompt γ -rays emission and inner-shell transitions that in turn generate Auger electrons and X-rays (Figure 2.7A). The high energy of prompt γ affects tissues in the range of several tens of cm, which can be seen as a drawback reducing the selectivity of Gd-NCT. On the other hand, the energy

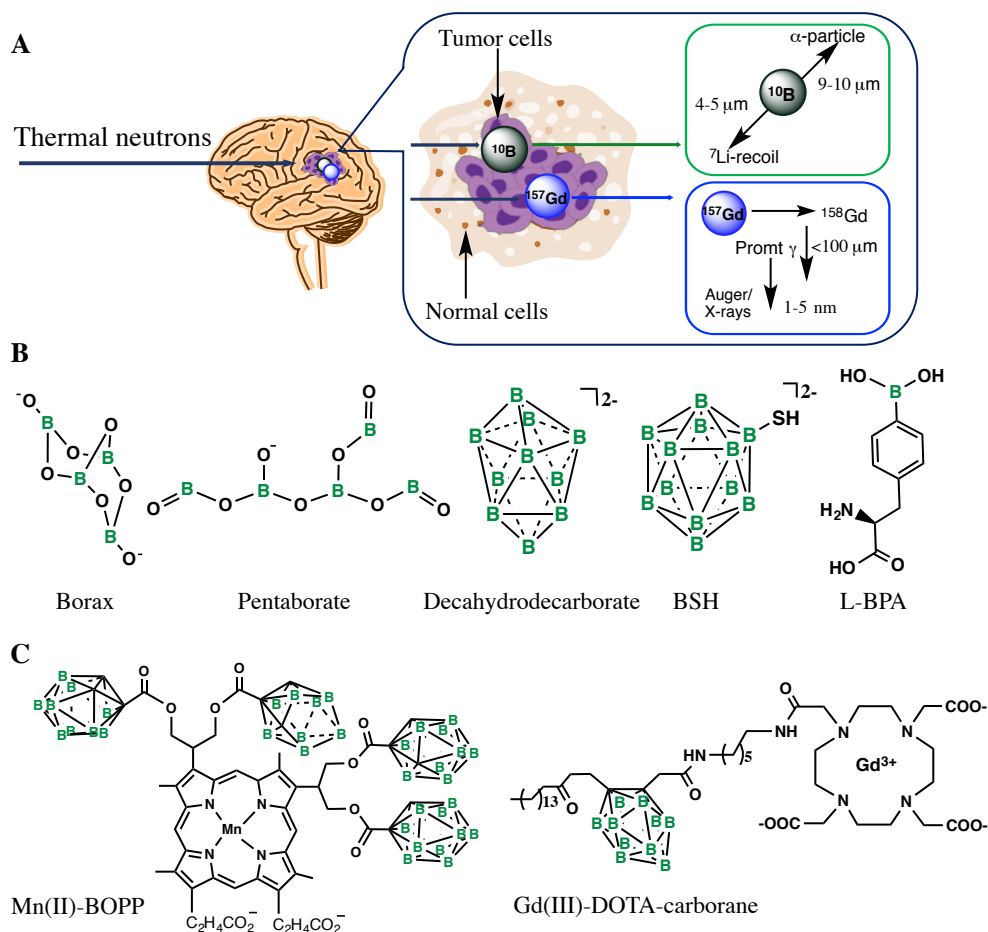


Figure 2.7. Principles and agents for boron and gadolinium NCT: A) Schematic representation of boron and gadolinium neutron capture reaction; B) first drugs for BNCT; C) examples of probes for combined MR imaging and BNCT.

deposition of the prompt γ is much less in comparison to the dose delivered by Auger electrons, which results in double-stranded DNA breaks, provided that ^{157}Gd is deposited in the direct proximity of the nucleus or other vital organelles with the effective concentration of 200 $\mu\text{g/g}$ of tumor tissues. These considerations require even more careful design of the agents for successful therapies, as extensively reviewed in the literature.^[69]

An obvious choice for the Gd-containing agents for Gd-NCT would be MRI CAs that already exist in the clinic if not their unspecific nature towards the tumors. Several groups have reported on the *in vivo* therapeutic effect of Gd(III)-DTPA upon neutron irradiation of tumors either after continuous infusion^[70] or intratumoral administration^[71] of the agent. An improved intravenous delivery of ¹⁵⁷Gd (up to 800 µg) with a favorable brain tumor/normal tissue ratio could be achieved with Gd(III)-EDTMP (ethylene diaminetetrabismethylenephosphonate) — a phosphonated ethylenediaminetetraacetic acid (EDTA)-analogue.^[72] However, all these attempts only confirmed the prerequisite for not only the specificity of the agents towards tumors, but also their prolonged retention during irradiation sessions. From this perspective, encapsulation of Gd-complexes into nanoparticulate systems offers a possibility for intravenous delivery of high-payloads of Gd to the tumors based on either EPR effect or conjugation with targeting vectors; both approaches have been worked out extensively for MRI. For instance, loading of Gd(III)-DTPA into chitosan nanoparticles^[73] or calcium phosphate micelles^[74] resulted in enhanced accumulation of the probe after intratumoral injection was accompanied with significant reduction of tumor growth under localized MRI contrast compared to Gd(III)-DTPA alone.

Conclusions

Translation of MRI-assisted radiotherapy into the clinic requires interdisciplinary efforts taking into account the beneficial aspects of each modality as well as the limitations and challenges. Due to its non-invasive nature and high soft-tissue resolution, MRI has already established itself as a good alternative to CT imaging that can offer complementary information in RTP. On the other hand, increased involvement of MRI during actual RT will eventually depend on the instrumental progress in integration of linear accelerators and MRI scanners and development of new treatment modalities such as image-guided brachytherapy, which will ultimately lead to expansion of the research towards MRI-based radiotheranostics. The already existing examples of such probes discussed in this review highlight the advantages of imaging for RT by enhancing the accuracy of the treatment relying on determination of the correct values of the delivered doses, the right timing for

irradiation, and the possibility to follow the therapeutic effects in time. Maximization of the therapeutic effect was shown to be reached through additional assets such as radiosensitization, simultaneous hyperthermia, or the presence of an external magnetic field. These methodologies can profit from the versatile properties of NPs. In general, the preference to nanoparticulate systems with high relaxivities and the simultaneous ability to either serve as radiosensitizer or carry various radiotherapeutic functionalities is clearly identified. The small size in combination with high surface-to-volume ratio, the possibility for facile surface functionalization, and the capacity for high-payload of imaging reporters render NPs very attractive for radiotheranostic applications. Delivery of NPs can be realized through either passive (EPR) or active (conjugation of specific vectors) targeting, while the administration route is an important parameter determining the biodistribution. A drawback in case of intravenous injection of NPs is their removal from the circulation by the monoclonal phagocytosis with 80% deposition in the liver Kupffer cells. Thereby, the negative surface charges of NPs increase hepatic uptake, while neutral charges increase blood-circulation time. Intratumoral administration of radiotherapeutic NPs, with additional MRI enhancing properties as a good alternative for brachytherapy, will obviously require careful study of tumor microenvironments in order to functionalize NPs in accordance with the therapeutic objective and the best imaging performance. In the case of SPIONs, the intracellular uptake typically results in their metabolization into lysosomes and release of non-superparamagnetic iron ions, which then undergo intrinsic iron metabolic pathways. However, elevated blood concentrations of iron may lead to severe anaphylactic reactions, which has mainly been the reason for the withdrawal of SPIONs from clinics. Therefore, the aspects such as non-specific accumulation, toxicity, long-term deposition, decomposition and eventual elimination of NPs are the most important challenges to be tackled during the design of MRI nanoproboscopes for radiotherapy, even if their properties for imaging and therapeutic efficiency seem to be satisfactory.

References

- [1] S. Gaddikeri, R. S. Gaddikeri, T. Tailor and Y. Anzai, *AJNR American Journal of Neuroradiology* **2016**, *37*, 588-595.
- [2] P. J. Hoskin, D. M. Carnell, N. J. Taylor, R. E. Smith, J. J. Stirling, F. M. Daley, M. I. Saunders, S. M. Bentzen, D. J. Collins, J. A. d'Arcy and A. P. Padhani, *International Journal of Radiation Oncology, Biology, Physics* **2007**, *68*, 1065-1071.
- [3] T. Bostel, N. H. Nicolay, J. G. Grossmann, A. Mohr, S. Delorme, G. Echner, P. Häring, J. Debus and F. Sterzing, *Radiation Oncology Journal* **2014**, *9*, 12.
- [4] B. W. Raaymakers, J. J. Lagendijk, J. Overweg, J. G. Kok, A. J. Raaijmakers, E. M. Kerkhof, R. W. van der Put, I. Meijsing, S. P. Crijns, F. Benedosso, M. van Vulpen, C. H. de Graaff, J. Allen and K. J. Brown, *Physics in Medicine and Biology* **2009**, *54*, N229-237.
- [5] A. Torresin, M. G. Brambilla, A. F. Monti, A. Moscato, M. A. Brockmann, L. Schad, U. I. Attenberger and F. Lohr, *Zeitschrift für Medizinische Physik* **2015**, *25*, 210-220.
- [6] S. S. Kelkar and T. M. Reineke, *Bioconjugate Chemistry* **2011**, *22*, 1879-1903.
- [7] L. Veldeman, I. Madani, F. Hulstaert, G. De Meerleer, M. Mareel and W. De Neve, *The Lancet Oncology* **2008**, *9*, 367-375.
- [8] B. Emami, A. Sethi and G. J. Petruzzelli, *International Journal of Radiation Oncology, Biology, Physics* **2003**, *57*, 481-488.
- [9] O. Caffo, *Lung Cancer* **2001**, *34*, 81-90.
- [10] P. Wardman, *Clinical Oncology* **2007**, *19*, 397-417.
- [11] M. H. Castillo, T. M. Button, R. Doerr, M. I. Homs, C. W. Pruett and J. I. Pearce, *The American Journal of Surgery* **1988**, *156*, 261-263.
- [12] H. Matsudaira, A. M. Ueno and I. Furuno, *Radiation Research* **1980**, *84*, 144-148.
- [13] R. Ngoune, A. Peters, D. von Elverfeldt, K. Winkler and G. Pütz, *Journal of Controlled Release* **2016**, *238*, 58-70.
- [14] J. V. Jokerst, T. Lobovkina, R. N. Zare and S. S. Gambhir, *Nanomedicine* **2011**, *6*, 715-728.
- [15] J. F. Hainfeld, D. N. Slatkin and H. M. Smilowitz, *Physics in Medicine and Biology* **2004**, *49*, N309-N315.

- [16] E. Toth, L. Helm and A. Merbach in *Relaxivity of gadolinium(III) complexes: theory and mechanism*, Eds.: A. Merbach, L. Helm and E. Toth), John Wiley and Sons Ltd, pp. 25-81-25-81.
- [17] B. Zhang, L. Liang, W. Chen, C. Liang and S. Zhang, *PLOS ONE* **2015**, *10*, e0129720.
- [18] E. Vergauwen, A.-M. Vanbinst, C. Brussaard, P. Janssens, D. De Clerck, M. Van Lint, A. C. Houtman, O. Michel, K. Keymolen, B. Lefevere, S. Bohler, D. Michielsen, A. C. Jansen, V. Van Velthoven and S. Gläser, *Hereditary Cancer in Clinical Practice* **2018**, *16*, 2.
- [19] S. R. Thomas and D. Khuntia, *Expert Opinion on Drug Discovery* **2011**, *6*, 195-203.
- [20] G. M. Richards and M. P. Mehta, *Expert Opinion on Pharmacotherapy* **2007**, *8*, 351-359.
- [21] G. Thiabaud, R. McCall, G. He, J. F. Arambula, Z. H. Siddik and J. L. Sessler, *Angewandte Chemie International Edition in English* **2016**, *55*, 12626-12631.
- [22] M. Botta and L. Tei, *European Journal of Inorganic Chemistry* **2012**, *2012*, 1945-1960.
- [23] R. Bazzi, M. A. Flores, C. Louis, K. Lebbou, W. Zhang, C. Dujardin, S. Roux, B. Mercier, G. Ledoux, E. Bernstein, P. Perriat and O. Tillement, *Journal of Colloid and Interface Science* **2004**, *273*, 191-197.
- [24] J.-L. Bridot, D. Dayde, C. Rivière, C. Mandon, C. Billotey, S. Lerondel, R. Sabattier, G. Cartron, A. Le Pape, G. Blondiaux, M. Janier, P. Perriat, S. Roux and O. Tillement, *Journal of Materials Chemistry* **2009**, *19*, 2328-2335.
- [25] A. Mignot, C. Truillet, F. Lux, L. Sancey, C. Louis, F. Denat, F. Boschetti, L. Bocher, A. Gloter, O. Stéphan, R. Antoine, P. Dugourd, D. Luneau, G. Novitchi, L. C. Figueiredo, P. C. de Morais, L. Bonneviot, B. Albela, F. Ribot, L. Van Lokeren, I. Déchamps-Olivier, F. Chuburu, G. Lemerrier, C. Villiers, P. N. Marche, G. Le Duc, S. Roux, O. Tillement and P. Perriat, *Chemistry – A European Journal* **2013**, *19*, 6122-6136.
- [26] G. Le Duc, S. Roux, A. Paruta-Tuarez, S. Dufort, E. Brauer, A. Marais, C. Truillet, L. Sancey, P. Perriat, F. Lux and O. Tillement, *Cancer Nanotechnology* **2014**, *5*, 4.
- [27] A. Bianchi, F. Lux, O. Tillement and Y. Crémillieux, *Magnetic Resonance in Medicine* **2013**, *70*, 1419-1426.
- [28] A. Detappe, E. Thomas, M. W. Tibbitt, S. Kunjachan, O. Zavidij, N. Parnandi, E. Reznichenko, F. Lux, O. Tillement and R. Berbeco, *Nano Letters* **2017**, *17*, 1733-1740.

- [29] F. Du, L. Zhang, L. Zhang, M. Zhang, A. Gong, Y. Tan, J. Miao, Y. Gong, M. Sun, H. Ju, C. Wu and S. Zou, *Biomaterials* **2017**, *121*, 109-120.
- [30] M. Mahmoudi, H. Hosseinkhani, M. Hosseinkhani, S. Boutry, A. Simchi, W. S. Journeay, K. Subramani and S. Laurent, *Chemical reviews* **2011**, *111*, 253-280.
- [31] S. Laurent, D. Forge, M. Port, A. Roch, C. Robic, L. Vander Elst and R. N. Muller, *Chemical Reviews* **2008**, *108*, 2064-2110.
- [32] R. A. Revia and M. Zhang, *Materials Today* **2016**, *19*, 157-168.
- [33] N. Kohler, C. Sun, A. Fichtenholtz, J. Gunn, C. Fang and M. Zhang, *Small* **2006**, *2*, 785-792.
- [34] Z. Medarova, W. Pham, Y. Kim, G. Dai and A. Moore, *International Journal of Cancer* **2006**, *118*, 2796-2802.
- [35] A. Saberi, D. Shahbazi-Gahrouei, M. Abbasian, M. Fesharaki, A. Baharlouei and Z. Arab-Bafrani, *International Journal of Radiation Biology* **2017**, *93*, 315-323.
- [36] K. Khoshgard, P. Kiani, A. Haghparast, L. Hosseinzadeh and M. T. Eivazi, *International Journal of Radiation Biology* **2017**, *93*, 757-763.
- [37] S. Khoei, S. R. Mahdavi, H. Fakhimikabir, A. Shakeri-Zadeh and A. Hashemian, *International Journal of Radiation Biology* **2014**, *90*, 351-356.
- [38] S. Klein, A. Sommer, L. V. R. Distel, W. Neuhuber and C. Kryschi, *Biochemical and Biophysical Research Communications* **2012**, *425*, 393-397.
- [39] E. K. Kirakli, G. Takan, S. Hoca, F. Z. B. Müftüler, A. Y. Kılçar and S. A. Kamer, *Journal of Radioanalytical and Nuclear Chemistry* **2018**, *315*, 595-602.
- [40] A. Rajaei, X. Wensheng, L. Zhao, S. Wang, Y. Liu, Z. Wu, J. Wang and F. Si-Shen, *J Biomed Nanotechnol* **2018**, *14*, 1159-1168.
- [41] D. Zhao, X. Sun, J. Tong, J. Ma, X. Bu, R. Xu and R. Fan, *Acta Biochimica et Biophysica Sinica* **2012**, *44*, 678-684.
- [42] Y. Dou, X. Li, W. Yang, Y. Guo, M. Wu, Y. Liu, X. Li, X. Zhang and J. Chang, *ACS Applied Materials and Interfaces* **2017**, *9*, 1263-1272.
- [43] T. J. Daou, J. M. Grenèche, G. Pourroy, S. Buathong, A. Derory, C. Ulhaq-Bouillet, B. Donnio, D. Guillon and S. Begin-Colin, *Chemistry of Materials* **2008**, *20*, 5869-5875.
- [44] M. Longmire, P. L. Choyke and H. Kobayashi, *Nanomedicine* **2008**, *3*, 703-717.

- [45] T. M. Zagar, J. R. Oleson, Z. Vujaskovic, M. W. Dewhirst, O. I. Craciunescu, K. L. Blackwell, L. R. Prosnitz and E. L. Jones, *International Journal of Hyperthermia* **2010**, *26*, 612-617.
- [46] C. Kratochwil, F. Bruchertseifer, F. L. Giesel, M. Weis, F. A. Verburg, F. Mottaghy, K. Kopka, C. Apostolidis, U. Haberkorn and A. Morgenstern, *Journal of Nuclear Medicine* **2016**, *57*, 1941.
- [47] C.-H. Yeong, M.-h. Cheng and K.-H. Ng, *Journal of Zhejiang University SCIENCE B* **2014**, *15*, 845-863.
- [48] D. P. Carvalho and A. C. F. Ferreira, *Arquivos Brasileiros de Endocrinologia and Metabologia* **2007**, *51*, 672-682.
- [49] S. Srivastava and E. Dadachova, *Seminars in Nuclear Medicine* **2001**, *31*, 330-341.
- [50] G. D'angelo, R. Sciuto, M. Salvatori, I. Sperduti, G. Mantini, C. Maini and G. Mariani, *The Quarterly Journal of Nuclear Medicine and Molecular Imaging: Official Publication of the Italian Association of Nuclear Medicine (AIMN)[and] the International Association of Radiopharmacology (IAR),[and] Section of the Society of..* **2012**, *56*, 538-543.
- [51] D. Ashutosh, F. F. Knapp and M. R. A. Pillai, *Current Radiopharmaceuticals* **2013**, *6*, 152-180.
- [52] T. J. Pugh and S. S. Pokharel, *Brachytherapy* **2017**, *16*, 659-664.
- [53] W. Bult, S. G. C. Kroeze, M. Elschot, P. R. Seevinck, F. J. Beekman, H. W. A. M. de Jong, D. R. A. Uges, J. G. W. Kosterink, P. R. Luijten, W. E. Hennink, A. D. van het Schip, J. L. H. R. Bosch, J. F. W. Nijsen and J. J. M. Jans, *PLOS ONE* **2013**, *8*, e52178.
- [54] M. L. J. Smits, M. Elschot, M. A. A. J. van den Bosch, G. H. van de Maat, A. D. van het Schip, B. A. Zonnenberg, P. R. Seevinck, H. M. Verkooijen, C. J. Bakker, H. W. A. M. de Jong, M. G. E. H. Lam and J. F. W. Nijsen, *Journal of Nuclear Medicine* **2013**, *54*, 2093.
- [55] G. H. van de Maat, P. R. Seevinck, M. Elschot, M. L. J. Smits, H. de Leeuw, A. D. van het Schip, M. A. D. Vente, B. A. Zonnenberg, H. W. A. M. de Jong, M. G. E. H. Lam, M. A. Viergever, M. A. A. J. van den Bosch, J. F. W. Nijsen and C. J. G. Bakker, *European Radiology* **2013**, *23*, 827-835.
- [56] J. Cao, Y. Wang, J. Yu, J. Xia, C. Zhang, D. Yin and U. O. Häfeli, *Journal of Magnetism and Magnetic Materials* **2004**, *277*, 165-174.

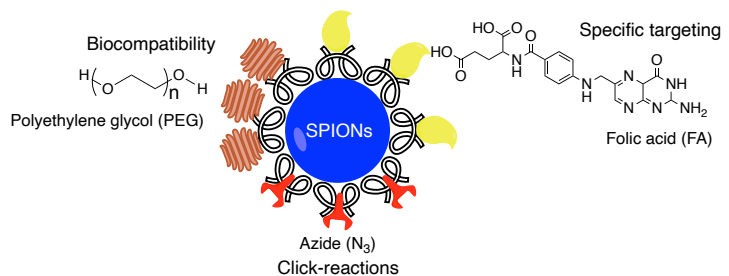
- [57] Z. Chunfu, C. Jinquan, Y. Duanzhi, W. Yongxian, F. Yanlin and T. Jiajü, *Applied Radiation and Isotopes* **2004**, *61*, 1255-1259.
- [58] C. Zhang, H. Sun, J. Xia, J. Yu, S. Yao, D. Yin and Y. Wang, *Journal of Magnetism and Magnetic Materials* **2005**, *293*, 193-198.
- [59] T. N. Aslan, E. Aşık and M. Volkan, *RSC Advances* **2016**, *6*, 8860-8869.
- [60] M. Radović, M. P. Calatayud, G. F. Goya, M. R. Ibarra, B. Antić, V. Spasojević, N. Nikolić, D. Janković, M. Mirković and S. Vranješ-Đurić, *Journal of Biomedical Materials Research Part A* **2015**, *103*, 126-134.
- [61] J. Chen, S. Zhu, L. Tong, J. Li, F. Chen, Y. Han, M. Zhao and W. Xiong, *BMC Cancer* **2014**, *14*, 114.
- [62] L. Esser, N. A. Lengkeek, B. A. Moffat, M. N. Vu, I. Greguric, J. F. Quinn, T. P. Davis and M. R. Whittaker, *Polymer Chemistry* **2018**, *9*, 3528-3535.
- [63] G. Locher, *American Journal of Roentgenology* **1936**, *36*, 1-13.
- [64] S.-I. Miyatake, S. Kawabata, R. Hiramatsu, T. Kuroiwa, M. Suzuki, N. Kondo and K. Ono, *Neurologia medico-chirurgica* **2016**, *56*, 361-371.
- [65] R. F. Barth, J. A. Coderre, M. G. H. Vicente and T. E. Blue, *Clinical Cancer Research* **2005**, *11*, 3987-4002.
- [66] G. W. Kabalka, G. T. Smith, J. P. Dyke, W. S. Reid, C. D. Longford, T. G. Roberts, N. K. Reddy, E. Buonocore and K. F. Hübner, *Journal of Nuclear Medicine* **1997**, *38*, 1762-1767.
- [67] K. Takahashi, H. Nakamura, S. Furumoto, K. Yamamoto, H. Fukuda, A. Matsumura and Y. Yamamoto, *Bioorganic and Medicinal Chemistry* **2005**, *13*, 735-743.
- [68] L. R. Huang, R. M. Straubinger, S. B. Kahl, M.-S. Koo, J. J. Alletto, R. Mazurchuk, R. I. Chau, S. L. Thamer and R. J. Fiel, *Journal of Magnetic Resonance Imaging* **1993**, *3*, 351-356.
- [69] A. Deagostino, N. Protti, D. Alberti, P. Boggio, S. Bortolussi, S. Altieri and S. G. Crich, *Future Medicinal Chemistry* **2016**, *8*, 899-917.
- [70] Y. Akine, N. Tokita, K. Tokuyue, M. Satoh, H. Churei, C. L. Pechoux, T. Kobayashi and K. Kanda, *Japanese Journal of Cancer Research* **1993**, *84*, 841-843.
- [71] V. F. Khokhlov, P. N. Yashkin, D. I. Silin, E. S. Djorova and R. Lawaczeck, *Academic Radiology* **1995**, *2*, 392-398.
- [72] R. Brugger and J. Shih, *Strahlentherapie und Onkologie* **1989**, *165*, 153-156.

[73] H. Tokumitsu, J. Hiratsuka, Y. Sakurai, T. Kobayashi, H. Ichikawa and Y. Fukumori, *Cancer Letters* **2000**, *150*, 177-182.

[74] N. Dewi, P. Mi, H. Yanagie, Y. Sakurai, Y. Morishita, M. Yanagawa, T. Nakagawa, A. Shinohara, T. Matsukawa, K. Yokoyama, H. Cabral, M. Suzuki, Y. Sakurai, H. Tanaka, K. Ono, N. Nishiyama, K. Kataoka and H. Takahashi, *Journal of Cancer Research and Clinical Oncology* **2016**, *142*, 767-775.

Preparation and Surface Functionalization of Superparamagnetic Iron Oxide Nanoparticles Designed for Theranostic Application

3



Introduction

Magnetic Resonance Imaging (MRI) is a non-invasive diagnostic technique, which enables anatomical images of soft tissues with a resolution much higher compared to other imaging techniques, such as Computed Tomography (CT), Ultrasonography (US) or Positron and Single Photon Emission Tomographies (PET and SPECT, respectively). Compared to PET/SPECT, no ionizing radiation is involved, and therefore, the whole process of imaging with MR can be done repeatedly, without any harmful effects on the patients. To enhance the images, contrast agents (CAs) are applied in almost 30% of MRI scans.^[1] Two types of MR imaging representations can be distinguished based on either longitudinal (T_1) or transversal (T_2) relaxation of protons in tissues, generating bright or dark contrast, respectively.^[2] For the T_1 -weighted imaging, small paramagnetic complexes, e.g. Gd(III)-DOTA or Gd(III)-DTPA are applied, while in the case of the T_2 -weighted imaging, superparamagnetic iron oxide nanoparticles (SPIONs) are the typical contrast agents. An example of a clinically approved T_2 MRI CA is ENDOREM.^[3]

Magnetic properties of SPIONs are affected by the crystallinity and size of the magnetite core.^[4] In general, SPIONs with the size below 20 nm are preferred for the application as T_2 MRI CAs.^[5] However, it has to be taken into account that smaller nanoparticles (<5 nm) are easily cleared from the body, while the bigger ones (>10 nm) are typically taken up by the liver.^[6] These considerations require a careful design of SPIONs in terms of morphology as well as availability of facile methods for the preparation of nanoparticles in a highly controlled way. To obtain SPIONs with a good shape/size distribution and favorable magnetic properties, several synthetic protocols have been developed, such as co-precipitation,^[7] thermal decomposition,^[8] polyol process,^[9] microemulsion,^[10] and hydrothermal method.^[11] The former method, being convenient and cheap, can be considered as the most suitable for the production of well-dispersed SPIONs within the diameter of ± 10 nm.^[7] At the same time, the co-precipitation method is often accompanied with agglomeration and insufficient crystallinity of the resulted nanoparticles. Recently, thermal decomposition method has been gaining attention for the production of

monodispersed nanoparticles by using iron acetylacetonate as a precursor with a simple control of the size-growth under heating at certain temperatures.^[8]

The interest in magnetic nanoparticles as MRI contrast agents is not only due to their superior magnetic properties but also their ability to accumulate at the tumor site by enhanced permeability and retention (EPR) effect,^[12] which means that small nanoparticles can easily enter the leaky vasculature of the blood vessels surrounding the abnormal cancer cells in contrast to normal tissues.^[13] Thereby, with a proper surface modification, SPIONs are promising agents not only for MRI diagnosis but also for therapeutic purposes, such as targeted drug delivery^[6] and magnetic hyperthermia.^[14]

When injected intravenously, nanoparticles for imaging/therapeutic applications must in any case be long-circulating and stealthy to the immune system that otherwise recognizes and removes them from the blood-circulation through macrophage activation. This can be achieved by decorating the surface of nanoparticles with biocompatible polyethyleneglycol (PEG) molecules, preferably with long chains up to 35 kDa.^[15] An additional advantage of PEG-functionalization is to enhance the colloidal stability of the SPIONs.^[12]

In this study, we exploit all the mentioned advantages of SPIONs for a two-step tumor targeting approach, which as such is beyond scope of this chapter. However, the design of functionalized nanoparticles described in this work is realized to allow events on the surface of cancer cells involving specific MRI-guided delivery of SPIONs (step 1), followed by injection of a radiotherapeutic agent that seeks out and binds to the nanoparticles (step 2). This strategy requires investigations on synthetic methods for better size control, colloidal stability, and proper functionalization of the SPIONs surface. The first two aspects were addressed by comparing a common co-precipitation method with thermal decomposition, which was shown to be more efficient and resulted in SPIONs with magnetic properties sufficient for a good MRI contrast.

The guidelines for functionalization of the surface of SPIONs (Figure 3.1) are primarily based on the selectivity towards cancer cells, which was rationalized with the use of folic acid (FA) known to bind to folic acid receptors (FAR) overexpressed by a number of tumors, including ovarian, breast and cervical cancers.^[16] Further functionality serving the concept of the *in vivo* two-step targeting, are azide-groups that were stayed at the surface in order to

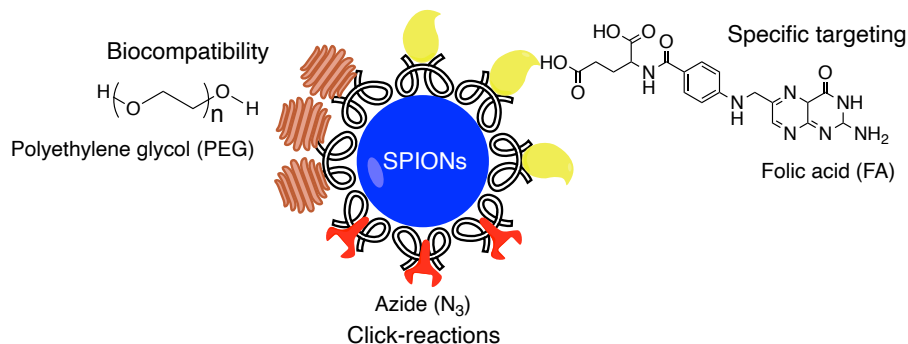


Figure 3.1. Schematic representation of SPIONs functionalization strategies using polyethyleneglycol (PEG), folic acid (FA) and azide (N_3) molecules for the purpose of biocompatibility, specific targeting and click-reaction, respectively.

enable the intended click-reaction with a radiotherapeutic agent modified with a cyclooctyne moiety (see next chapter). Finally, some of the SPIONs were provided with PEG-molecules with the aforementioned purpose, and some were left without it to investigate their influence on the tumor-recognition as well to the cellular uptake in the *in vitro* studies. Investigations reported in this chapter include description of procedures to prepare SPIONs and synthesize the functional molecules, full characterization of the physical properties, and biological evaluation of the final materials.

Results and Discussion

Synthesis and characterization of SPIONs

Co-precipitation method

Co-precipitation is one of the most common methods used to prepare SPIONs.^[7] This low-cost procedure is quite simple and involves the use of ferrous and ferric ions in the presence of aqueous base, such as tetramethylammonium hydroxide. With pH as one of the crucial parameters to control the size of the produced SPIONs,^[17] the method allows the preparation of SPIONs as small as 10 nm in diameter. Aggregation of SPIONs prepared by this method represents a significant drawback, which can, however, be circumvented by sonicating the suspensions for at least 1h. After this, the coating can be applied, which is

typically performed by the Stöber method.^[18] Tetraethylorthosilicate (TEOS), acting as the silica source, first reacts with water in an alcoholic solution (typically ethanol), then an ammonia solution is added. Consequently, TEOS undergoes hydrolysis in the ethanol/ammonia mixture and silanol monomers are formed in which the ethoxy groups (-Si-OEt) are replaced by hydroxides (-Si-OH).^[19] Additionally, ultrasonication for 1h is applied to prevent the aggregation of the coated SPIONs, followed by incubation at 60 °C for 6h to stabilize the Si-O-Fe linkages.

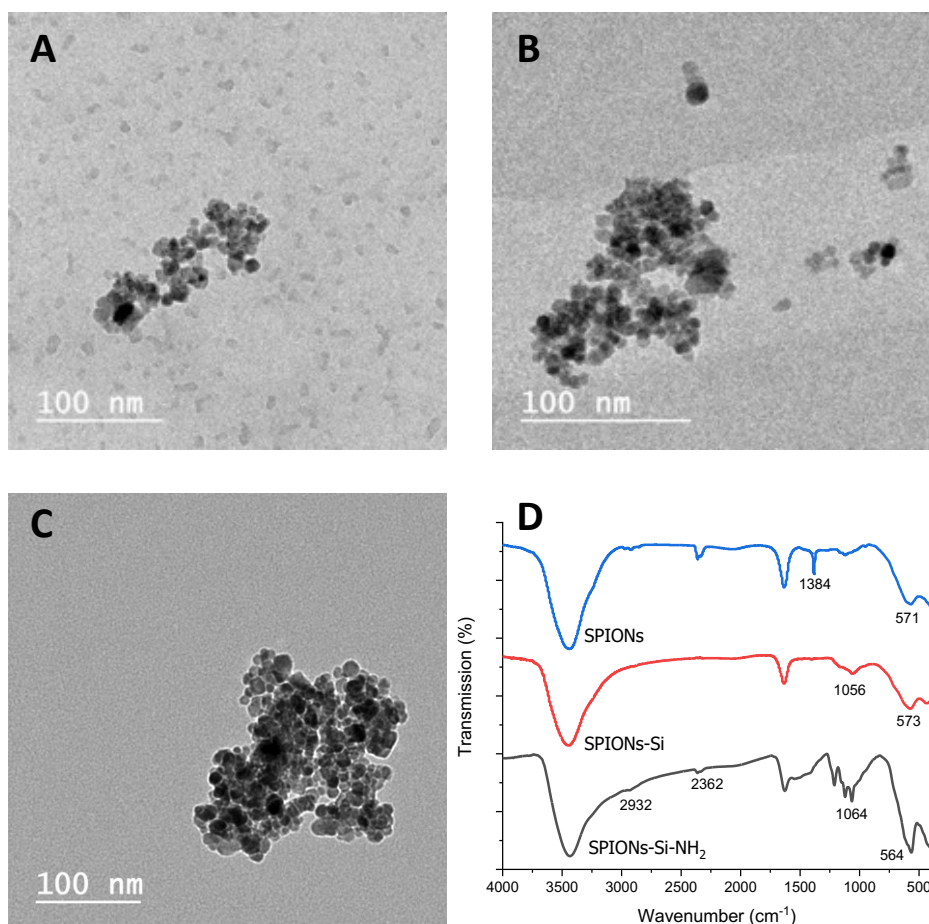


Figure 3.2. TEM images of SPIONs: non-coated (A), Si-coated (B), amino-group functionalized (C), and the corresponding FTIR-spectra (D).

Figure 3.2A-B shows TEM images of SPIONs before (A) and after (B) Si-coating. The diameters of nanoparticles calculated from the TEM measurements are 11 and 14 nm, respectively. The slight increase in diameter is attributed to the Si-coating, which was further confirmed by FTIR analysis (Figure 3.2D). Fe-O stretching band for the nanoparticles before surface modification was observed at 1384 cm^{-1} . After the coating with silica, the intensity of this peak decreased and the newly appeared peak at 1056 cm^{-1} was attributed to the Si-O-Fe linkage. Comparison of the ζ -potential of the uncoated and Si-coated SPIONs revealed the drop in values from -17.7 to -38.1 mV. This decrease in surface charge can be explained by the presence of the silanol groups that subsequently enhance the colloidal stability of the nanoparticles, which is an important parameter for *in vivo* applications.^[20] Furthermore, the presence of the ± 3 nm layer of silica on the surface of nanoparticles is expected to provide them with the necessary chemical stability and enable further conjugation with functional groups. In preparation for this functionalization, SPIONs-Si were modified with an amino group by attachment of (3-aminopropyl)trimethoxysilane (APTMS) to the surface using a simple silanization method.^[21] The successful attachment of $-\text{NH}_2$ on the SPIONs' surface was confirmed by the FTIR analysis, which shows an appearing peak at 2932 cm^{-1} (Figure 3.2D), as well as by increased ζ -potential ($+0.05$ mV). However, significant increase in size (up to 22 nm) of SPIONs after this step, as revealed in the TEM image (Figure 3.2C), suggests possible aggregation in the presence of APTMS, which could not be overcome by sonification.

Thermal decomposition method

Alternatively, thermal decomposition method to prepare SPIONs with the diameter below 20 nm and a narrow size-distribution was applied.^[8] Therefore, iron acetylacetonate was used as the iron-source in combination with surfactants oleic acid (OA) and oleylamine (OLA) dissolved in organic solvent (diphenyl ether) (Figure 3.3). The heating rate and the temperature maintenance at $200\text{ }^\circ\text{C}$ for 2 hours is crucial for a proper nucleation process, as the immediate reflux could lead to a wide size-distribution of the resulting SPIONs.^[22] Figure 3.4A shows TEM images of SPIONs-OA produced by thermal decomposition with the calculated size of 6 nm. The presence of oleic acid at the surface of nanoparticles was

confirmed by FTIR analysis (Figure 3.4B) demonstrating Fe-O stretching band at 600 cm^{-1} as well as the $-\text{CH}_2$ and $-\text{CH}_3$ stretching bands originating from the oleyl residues at 2852 and 2918 cm^{-1} , respectively.

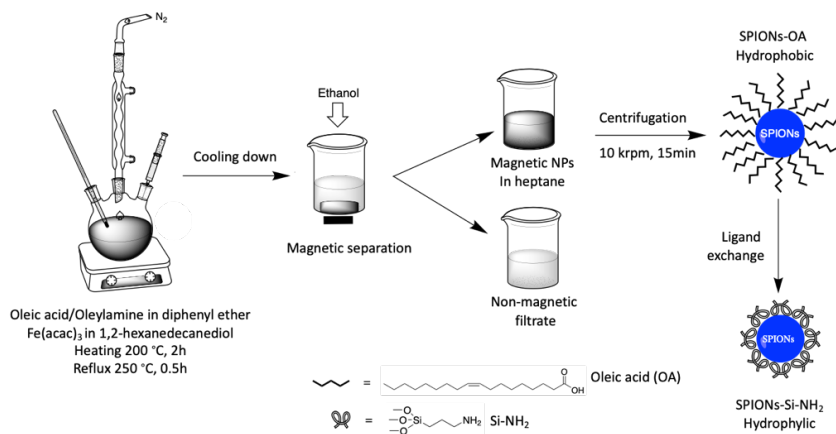


Figure 3.3. Preparation scheme of SPIONs via thermal decomposition with the surface coated with hydrophobic oleic acid (SPIONs-OA) and exchanged with hydrophilic 3-aminopropyl-3-methoxysilane (SPIONs-Si-NH₂).

Surfactants as oleic acid and oleylamine are known to help stabilizing and preventing agglomeration of the nanoparticles during the thermal decomposition process. Thereby, OA shows a higher ability to attach to the surface of nanoparticles due to the presence of carboxylic groups compared to the OLA.^[23]

To enable further conjugation of the surface SPIONs with envisioned functional groups, the hydrophobic OA-layer had to be converted to a hydrophilic one (Figure 3.3) by using APTMS.^[21] The TEM image (Figure 3.4A) shows a slight increase of the diameter to 6.6 nm and ζ -potential to $+19.8\text{ mV}$ (Table 3.1), caused by the NH_2 -groups present on the surface of nanoparticles.

Table 3.1. Characterization of SPIONs synthesized via co-precipitation and thermal decomposition methods.

Method	Coating	Functionalization	Size (nm)	ζ -potential (mV)
Co-precipitation	-	-	11	-17.70 ± 5.58
	Silica	-	14	-38.10 ± 5.29
	Silica	$-\text{NH}_2$	22	$+0.05 \pm 5.00$
Thermal decomposition	Oleic acid	-	6	-4.10 ± 3.90
	Silica	$-\text{NH}_2$	7	$+19.80 \pm 4.33$
	Silica	$-\text{N}_3\text{-FA}$	8	-0.28 ± 4.56
	Silica	$-\text{PEG-N}_3\text{-FA}$	8	-0.18 ± 4.67

The FTIR analysis further confirmed the presence of amino-groups on the surface of SPIONs (Figure 3.4D) by appearance of new bands corresponding to alkyl chain of APTMS (2926 and 2859 cm^{-1}), Si-O-Fe (1028 cm^{-1}), and protonated amino-groups (1525 and 621 cm^{-1}).^[24] Finally, the confirmation and quantification of ligand exchange was assessed by the thermogravimetric analysis (TGA), attributing the weight-loss of 23% observed for SPIONs-OA between 200 and 400 $^{\circ}\text{C}$ to the removal of oleic acid from the surface (Figure 3.5A).

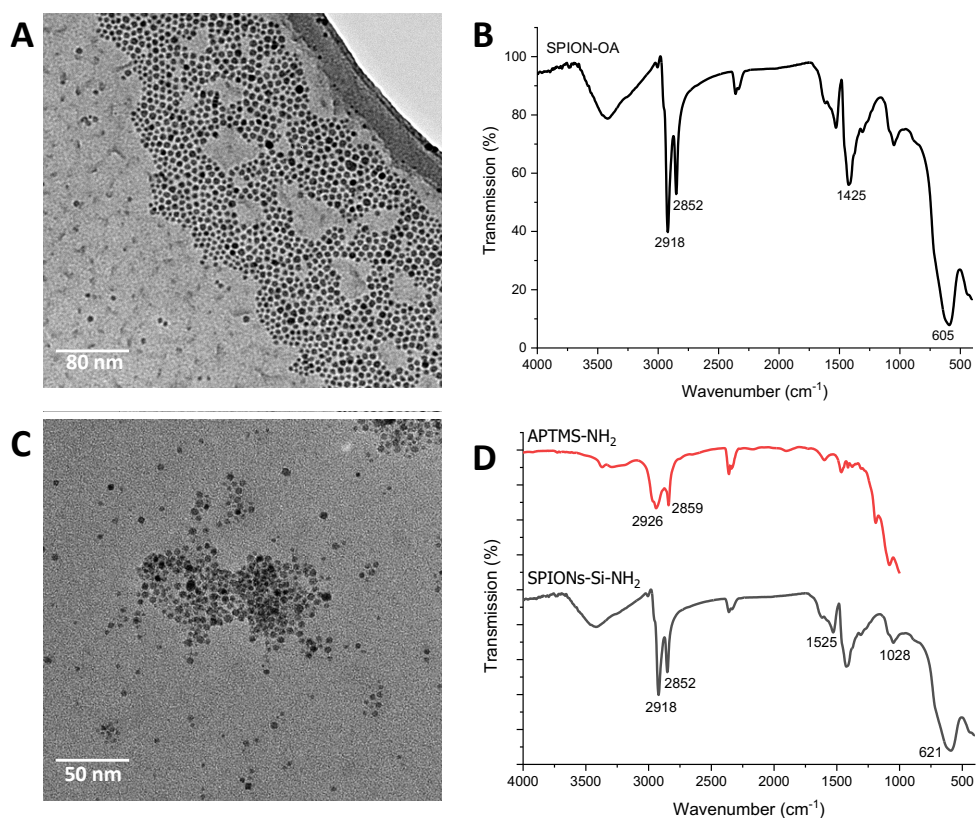


Figure 3.4. Characterization of SPIONs synthesized via thermal decomposition method by TEM (A and C, scale bar 100nm) and FTIR (B and D) before (red) and after (grey) ligand exchange between OA and NH₂-groups.

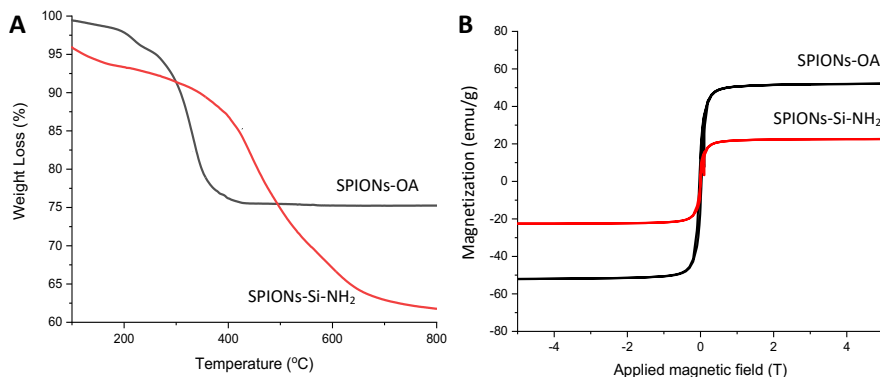


Figure 3.5. TGA profiles (A) and magnetization curves (B) of SPIONs covered by oleic acid (SPIONs-OA) (black) compared to SPIONs functionalized by amino groups (SPIONs-Si-NH₂) (red).

Magnetic properties of SPIONs were studied by Superconducting Quantum Interference Device (SQUID) magnetometer, which measures magnetic moments of the materials in response to an increasing magnetic field. As demonstrated in Figure 3.5B, saturation magnetization (M_s) of the SPIONs occurs already at 1T, reaching 52 to 22 emu/g for SPIONs-OA and SPIONs-Si-NH₂, respectively. The lower M_s of the latter nanoparticles can be explained by the additional mass contribution of diamagnetic material (APTMS) present at the surface after ligand exchange.^[25] Nevertheless, magnetic properties of SPIONs-Si-NH₂ can be considered sufficient for the envisioned MRI applications.

Overall, the thermal decomposition method proved to be the most efficient for the synthesis of small diameter (6 nm) SPIONs. The positive ζ -potential value generated by the ligand exchange from oleic acid to APTMS on the surface of SPIONs in turn increased the monodispersity. Therefore, these nanoparticles were utilized for further functionalization, physical characterizations, and biological evaluations.

Strategy of surface functionalization of SPIONs

As mentioned above, the introduction of amino groups at the surface of SPIONs allows their further conjugation with various functional molecules, which in this study are folic acid (FA), polyethylene glycol (PEG) and azide (N₃). To enable biological evaluations of the *in vitro* behavior of the designed SPIONs by means of confocal microscopy, their surface was

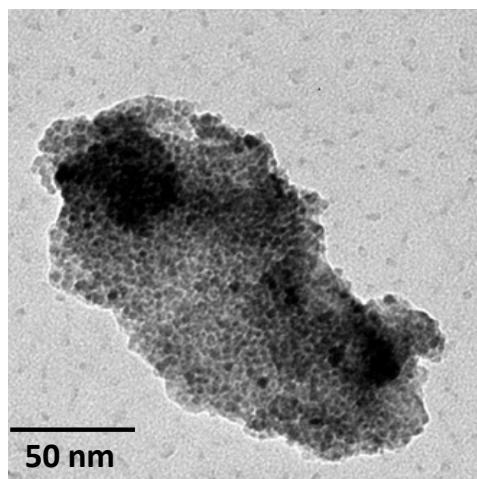
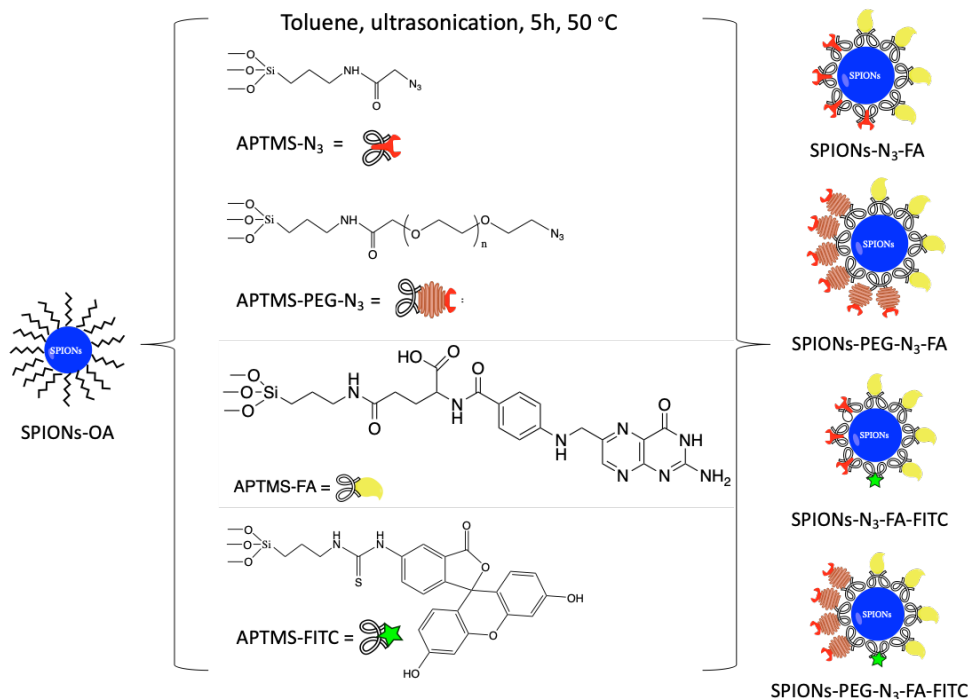


Figure 3.6. TEM image of SPIONs functionalized *via* direct conjugation of N₃- and FA- molecules.

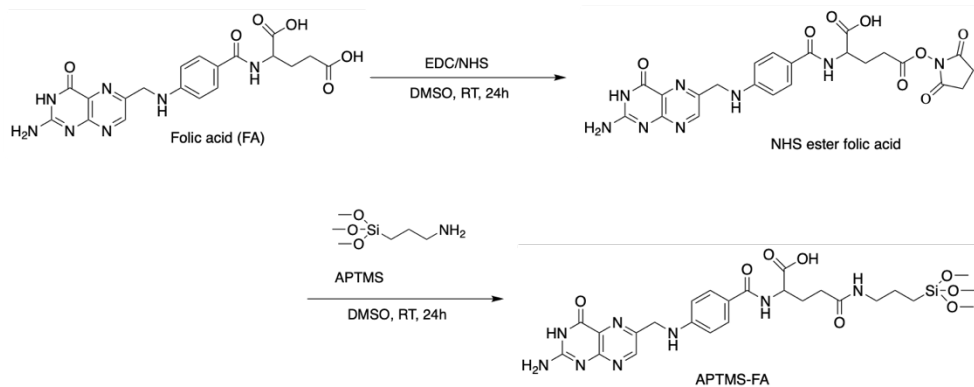
additionally modified with a small optical tag, fluorescein isothiocyanate (FITC) (Scheme 3.1). However, direct conjugation of functional moieties via APTMS results in a stronger agglomeration of the SPIONs (Figure 3.6) and the inability to ensure that all functional groups are sufficiently attached to the surface. Therefore, functionalization of SPIONs was performed with initially prepared APTMS-conjugates (see below), which were then attached to the surface of nanoparticles with the advantage of better control over the process in general, and the amounts of added conjugates, in particular. To realize this strategy, SPIONs-OA were used, and the exchange of hydrophobic groups was carried out in the same step of functionalization.

Folic acid APTMS conjugate (APTMS-FA)

Preparation of APTMS-FA started with activation of the carboxylic groups of FA through a reaction with N-hydroxysuccinimide (NHS) in the presence of a coupling reagent 1-ethyl-3-(3-dimethylaminopropyl)carbodiimide (EDC) (Scheme 3.2).^[26] APTMS was added after successful formation of the NHS ester was confirmed by NMR, after which the reaction mixture was kept under stirring at room temperature for 24hr. The final product APTMS-FA was characterized by NMR and FTIR and used for the conjugation with SPIONs prepared via thermal decomposition method described above.



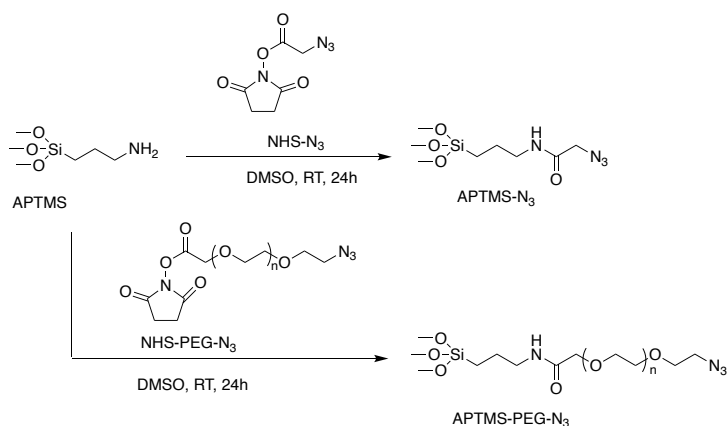
Scheme 3.1. Schematic representation of functionalized SPIONs used in this study.



Scheme 3.2. Folic acid conjugation to APTMS (APTMS-FA) via activation of FA with NHS ester (FA-NHS).

APTMS-azide conjugates (APTMS-N₃ and APTMS-PEG-N₃)

Two strategies of introduction of azides were investigated: i) directly to the surface of SPIONs via a methoxysilane linker and ii) as a terminal group of the PEG molecules. The latter option was considered seeing the possibility of bulky PEG-chains to cover the azide group making it not assessible for click-reactions. The reactions to convert APTMS to APTMS-N₃ and APTMS-PEG-N₃ were performed by using either NHS-N₃ or NHS-PEG-N₃ as the reactants in a molar excess (Scheme 3.3). The products were analyzed by NMR and FTIR in which the presence of N≡N stretching for APTMS-N₃ and APTMS-PEG-N₃ was confirmed by the peaks at 2104 cm⁻¹ and 2160 cm⁻¹, respectively (Figure 3.7).



Scheme 3.3. Reaction scheme of formation of APTMS-N₃ and APTMS-PEG-N₃ conjugates.

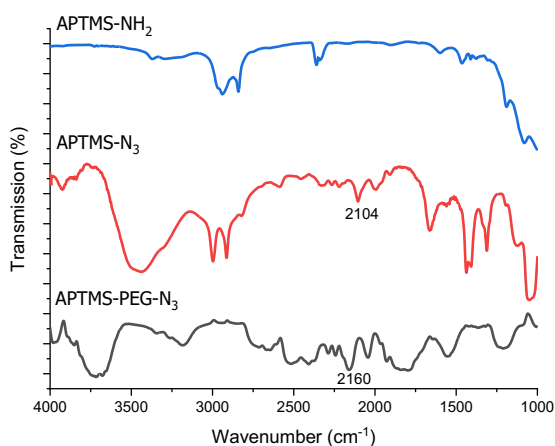


Figure 3.7. FTIR-spectra of APTMS-N₃-conjugates.

Functionalization and characterization of SPIONs

Conjugation of functional groups to the surface of nanoparticles was accomplished by using SPIONs-OA in a direct ligand-exchange method^[25] with the abovementioned APTMS-conjugates as depicted in Scheme 3.1. TEM measurements were performed to confirm the good monodispersity and determine the diameter of SPIONs (Figure 3.8A and B). After functionalization of SPIONs-OA with azide- and FA-groups the diameter increased from 6 nm to 7.5 and 8.1 nm for SPIONs-N₃-FA and SPIONs-PEG-N₃-FA, respectively. Characteristic N≡N stretching bands at 2106 and 2112 cm⁻¹ in the FTIR spectra confirmed successful functionalization of nanoparticles (Figure 3.8C). In addition, based on the FTIR quantification, it was also found that 1 mg of SPIONs contain 0.0238 ± 0.0047 mmol azide molecules.

The TGA-profiles (Figure 3.8D) measured on the functionalized SPIONs demonstrate a significant weight loss of about 70% after conjugation with azide- and FA-groups suggesting decomposition of FA at the surface of nanoparticles. The presence of azide- and FA- groups was also confirmed with ζ-potential measurements showing decreased surface charges of SPIONs-N₃-FA and SPIONs-PEG-N₃-FA to -0.28 and -0.18 mV, respectively, compared to SPIONs before the conjugation (Table 3.1).

Magnetic properties SPIONs before and after functionalization were investigated by measuring the magnetic moments with a SQUID-based magnetometer. A significant decrease of the values upon functionalization from 52 to 10-11 emu/g could be attributed to the introduction of a nonmagnetic mass on the surface of SPIONs, which in case of silanes has a greater impact due to polymerization leading to a multilayer compared to OA forming a monolayer.

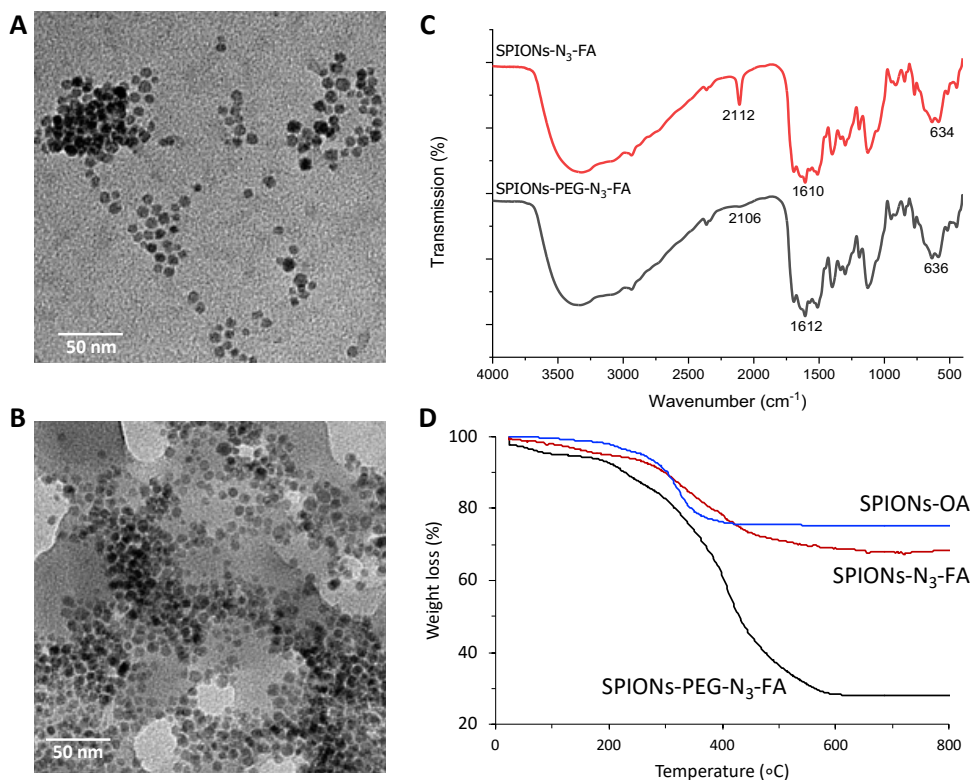


Figure 3.8. Characterization of SPIONs functionalized with APTMS- N_3 -PEG and APTMS-FA by TEM (**A**): SPIONs- N_3 -FA and **B**: SPIONs-PEG- N_3 -FA, scale bar 80 nm; FTIR (**C**) and TGA-profiles (**D**).

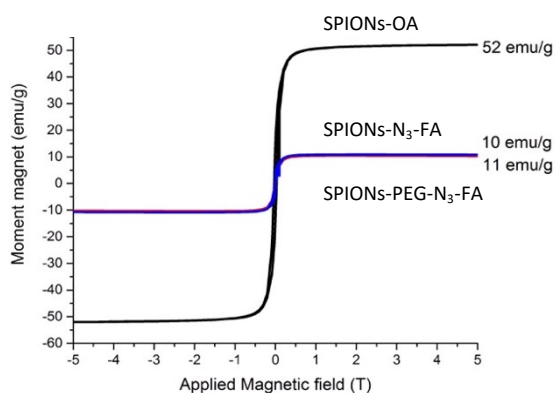


Figure 3.9. SQUID-curves obtained with SPIONs before (SPIONs-OA) and after (SPIONs- N_3 -FA and SPIONs-PEG- N_3 -FA) functionalization.

To assess the suitability of the functionalized SPIONs to perform as MRI CAs, the T_2 -relaxation was measured with ^1H NMR. CPMG (Carr-Purcell-Meiboom-Gill) pulse sequence measuring the spin echo coefficient was applied. Transversal relaxation rates ($1/T_2$) were plotted as a function of iron concentrations, expressed in mM of iron, and transversal relaxivities (r_2) were obtained from the slope of the fitting line (Figure 3.10A). Prior to the measurements, the suspensions of SPIONs were stabilized with 1% of xanthan in aqueous solution (Figure 3.10B) in order to slow the precipitation of nanoparticles. Apparently, for the higher concentrations this stabilization was not sufficient as evidenced from the last point (0.5 mM) deviating slightly from the straight line despite the addition of xanthan. Furthermore, lower relaxivity found for the PEG-functionalized SPIONs can be explained by the effect of long chains that are shielding the magnetic core from the bulk water, as described in the literature.^[27]

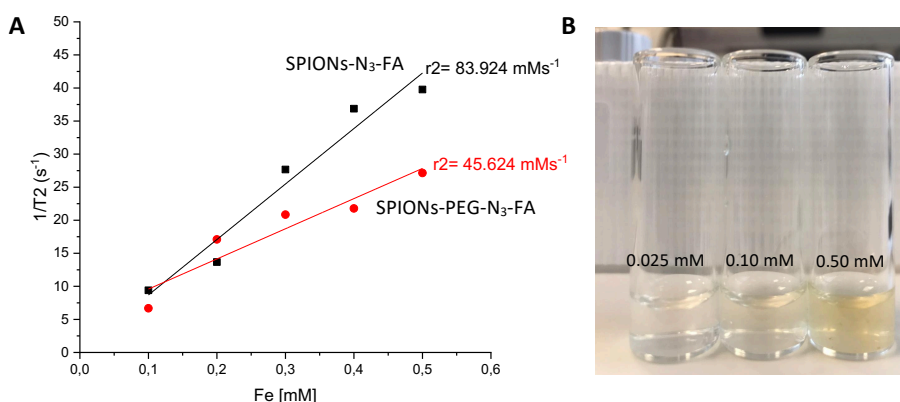


Figure 3.10. T_2 -relaxivity measurements of functionalized-SPIONs (A) and the dispersion of functionalized-SPIONs; 1% xanthan was added as nanoparticles dispersant. NMR measurements were performed at 9.4T, 25°C and pH 7.

To identify the Fe phases as the basis of magnetic properties of SPIONs, the Mössbauer spectroscopy technique was used relying on the sufficiently abundant ^{57}Fe isotope with low energy γ -ray characteristics.^[28] The method allows to examine the valence state of iron, which is found in nature as metallic (Fe^0) and ionic (Fe^{2+} and Fe^{3+}) as well as to determine the type of polyhedron formed by the iron atoms (trigonal, tetrahedral, octahedral, etc).

From the Mössbauer spectra it is evident that SPIONs-OA are mainly composed of tetrahedral and octahedral Fe^{3+} -species and the small quadrupole splitting value indicates the formation of maghemite-like ($\gamma\text{Fe}_2\text{O}_3$) structures (Figure 3.11 and Table 3.2). The stoichiometric ratio of the octahedral and tetrahedral Fe^{3+} ions is slightly different from the bulk maghemite (~ 1.5 vs. 1.67) due to the very small particle size of the measured structures. Small amounts (3%) of very disperse, superparamagnetic Fe^{3+} -structures were also observed. However, after the ligand exchange and functionalization process, the measured spectral area almost doubles, showing that the surrounding lattice of the Fe structures becomes more rigid in SPIONs- NH_2 , SPIONs- N_3 -FA and SPIONs-PEG- N_3 -FA. It also shows some partial reduction of the tetrahedral Fe^{3+} to metallic $\text{Fe}(0)$ species for SPIONs after functionalization due to the increasing the length of the ligands attached to the nanoparticles, while their superparamagnetic properties are retained.

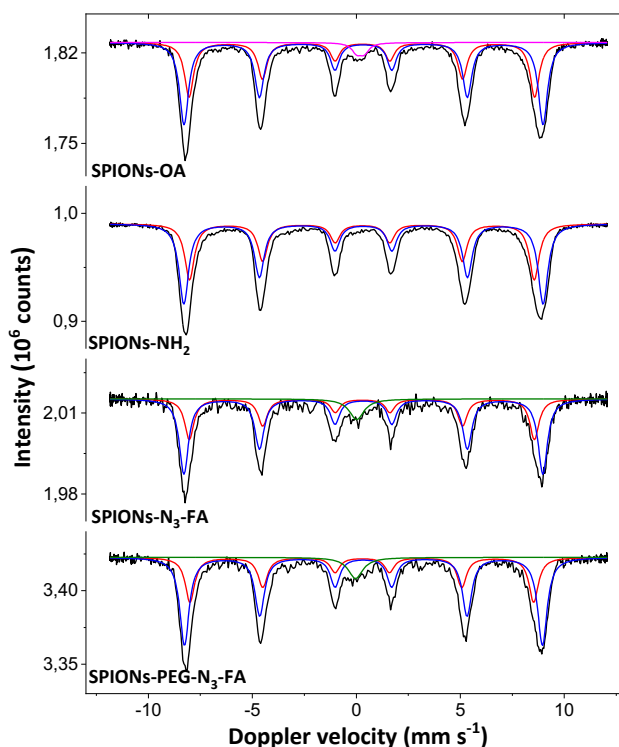


Figure 3.11. Mössbauer measurements SPIONs before and after functionalization performed at 4.2 K. Colors correspond to the isomer shift (black) of the typical Fe phases. Fe^{3+} tetrahedral (red), Fe^{3+} octahedral (blue), Fe^{3+} (purple), and Fe^0 (green).

Table 3.2. The Mössbauer fitted parameters of SPIONs before and after functionalization obtained at 4.2 K.*

	I.S (mm s ⁻¹)	Q.S (mm s ⁻¹)	Hyperfine field (T)	Γ (mm s ⁻¹)	Phase	Spectral contribution (%)
SPION-OA	0.28	-0.02	51.6	0.53	Fe ³⁺ tet.	39
	0.34	0.01	53.6	0.53	Fe ³⁺ oct.	58
	0.20	0.37	-	0.55	Fe ³⁺	3
SPIONs-NH ₂	0.28	-0.02	51.5	0.56	Fe ³⁺ tet.	41
	0.34	0.00	53.7	0.56	Fe ³⁺ oct.	59
SPIONs-N ₃ -FA	0.28	-0.02	51.6	0.54	Fe ³⁺ tet.	33
	0.34	0.00	53.6	0.54	Fe ³⁺ oct.	61
	0.01	-	-	0.85	Fe ⁰	6
SPIONs-PEG-N ₃ -FA	0.28	-0.02	51.4	0.54	Fe ³⁺ tet.	32
	0.34	0.00	53.5	0.54	Fe ³⁺ oct.	62
	0.01	-	-	0.85	Fe ⁰	6

*Experimental uncertainties: Isomer shift (I.S.) ± 0.02 mm s⁻¹; Quadrupole splitting (Q.S) ± 0.02 mm s⁻¹; Line width (Γ) ± 0.03 mm s⁻¹; Hyperfine field ± 0.1 T; Spectral contribution ± 3%.

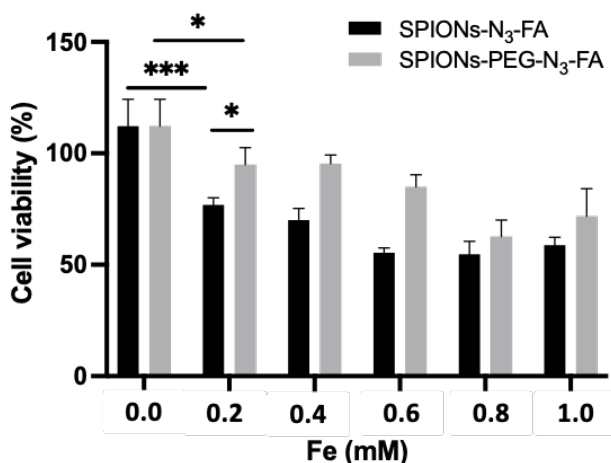


Figure 3.12. HeLa cells viability assay by CCK-8 after treatment with SPIONs-N₃-FA (black) and SPIONs-PEG-N₃-FA (grey) for 24h at Fe concentrations of 0.0-1.0 mM (n=5); *P < 0.05; *** P < 0.001.

In vitro studies on functionalized SPIONs

Cytotoxicity

The cytotoxicity of azide- and folic acid functionalized SPIONs with and without PEG (SPIONs-N₃-FA and SPIONs-PEG-N₃-FA) were investigated by using CCK-8 viability assay.^[29]

Therefore, HeLa cells were incubated for 24h with the above-mentioned nanoparticles at

the concentration range from 0.2 to 1 mM of iron. The importance of the PEGylation of nanoparticles is evident from Figure 3.12, which shows that SPIONs without PEG molecules (SPIONs-N₃-FA) decrease the viability of the cells to 78% already at the concentration of 0.2 mM. In contrast, the viability of the cells incubated with SPIONs-PEG-N₃-FA decreases to 80% only at the concentration of 0.6 mM. Based on these results, the concentration of SPIONs in further *in vitro* studies was chosen to be below 0.2 mM of Fe.

***In vitro* evaluation of functionalized-SPIONs on HeLa cells**

HeLa cell line derived from the human cervical carcinoma was used to evaluate the biological behaviour of SPIONs functionalized with folic acid as targeting vector, as well as with azide-group envisioned for the follow-up click-reaction. Furthermore, the nanoparticles carried a fluorescent tag (FITC) that appears as green color in confocal microscopy images under excitation/emission at approximately 495/519 nm.^[30] To evaluate cellular affinity and possible internalization of both, PEGylated (SPIONs-PEG-N₃-FA) and non-PEGylated (SPIONs-N₃-FA) nanoparticles by the cancer cells, they were added to a HeLa cell culture grown as a monolayer. Cell membranes and nuclei were stained with Red-Cellbrite 568/580 and blue 4',6-diamidino-2-phenylindole (DAP), respectively.

The confocal images demonstrate that the binding of the nanoparticles to the cells starts already after 2h of incubation and increases significantly after 24h (Figure 3.13). The small size of the nanoparticles (<10 nm) is known to be stimulating for the cellular uptake.^[31] However, a greater part of this affinity can be attributed to the interaction of the targeting vector FA present at the surface of SPIONs with the cell membrane through the binding with FAR, and possibly, induced receptor-mediated endocytosis.^[32]

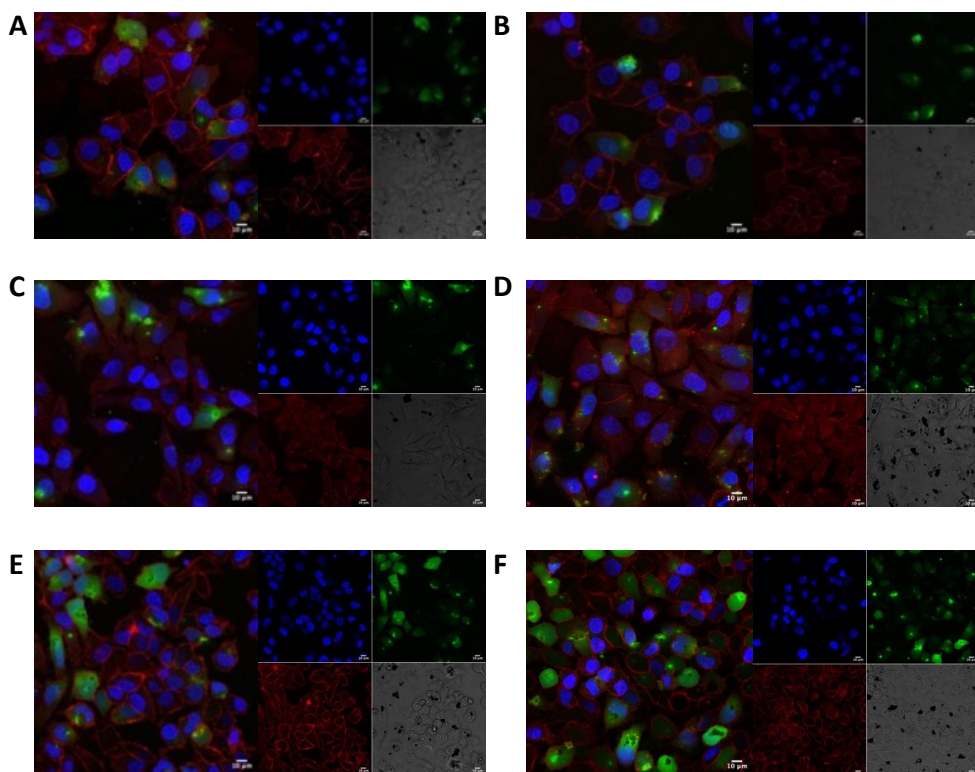


Figure 3.13. Fluorescence confocal microscope imaging of HeLa cells incubated with SPIONs-N₃-FA-FITC (left column) and SPIONs-PEG-N₃-FA-FITC (right column) for 2h (A-B), 4h (C-D) and 24h (E-F). The colors correspond to: SPIONs labeled with FITC (green), nuclei stained with DAPI (blue), and membranes stained with Red-Cellbrite (red), overlaid in the left images. Insets represent brightfield images; scale bar 10 μ m.

To proof this hypothesis, a competition binding experiment was conducted to observe the effect of FA targeting vector. Firstly, HeLa cells were incubated with FA for 24h to saturate the folic acid receptors, after which FA-functionalized SPIONs were added and incubated for another 4h. Figure 3.14A clearly shows a decrease in cellular uptake (internalized + membrane bound) when cells are pre-treated with the free FA, compared to the analogous experiment without saturation with FA (Figure 3.13C and D). However, Figure 3.14B still demonstrates a slight higher number nanoparticles uptaken by HeLa cells despite the FA competition binding experiment. This result suggests that FA plays a less important role in the internalization of the PEGylated nanoparticles.

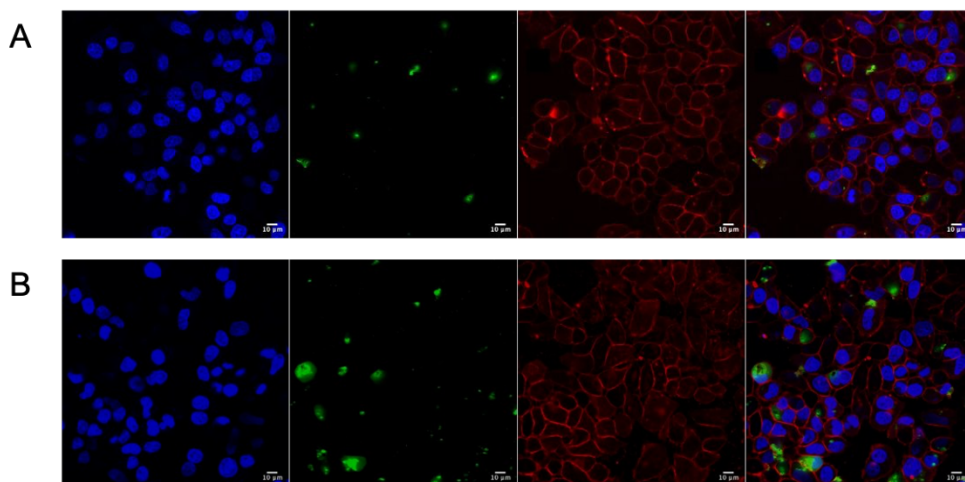


Figure 3.14. Fluorescence confocal microscope imaging of HeLa cells incubated first with folic acid (FA) for 24h and then with SPIONs-N₃-FA-FITC (A) and SPIONs-PEG-N₃-FA-FITC(B) for 4h. The colors correspond to: NPs labeled with FITC (green), nuclei stained with DAPI (blue) and membranes stained with Red-Cellbrite (red). Overlaid in the right images; scale bar 10 μm.

A significant number of SPIONs was also found around the cellular membrane after 4h, as it can be seen in the brightfield images (Figure 3.13). This is an important observation, since the presence of azide-functionalized SPIONs at the cell membrane is necessary for the envisioned click-reaction with the cyclooctyne-modified radiotherapeutic agent (see next chapter) to take place. To get more insight into feasibility of this approach and distinguish/quantify both, the internalized and membrane-bound SPIONs, a glycine treatment was applied after each incubation time to cleave the latter nanoparticles.^[33] After this, the membrane-bound fractions were collected, the cells were treated with a base to disrupt the membranes and release the internalized content, and the samples were measured by ICP-OES to determine the concentration of iron. The results indicate a higher uptake in the case of nonPEGylated nanoparticles in comparison with the PEGylated analogues, which can most likely be explained by steric hindrance of FA caused by the bulky PEG-chains (Figure 3.15). However, the fraction of membrane bound PEGylated nanoparticles is as twice as high compared to the nonPEGylated ones (0.09:0.2). Seeing the

general importance of PEG for the *in vivo* behavior of nanoparticles discussed earlier, this result can be considered promising for the intended application.

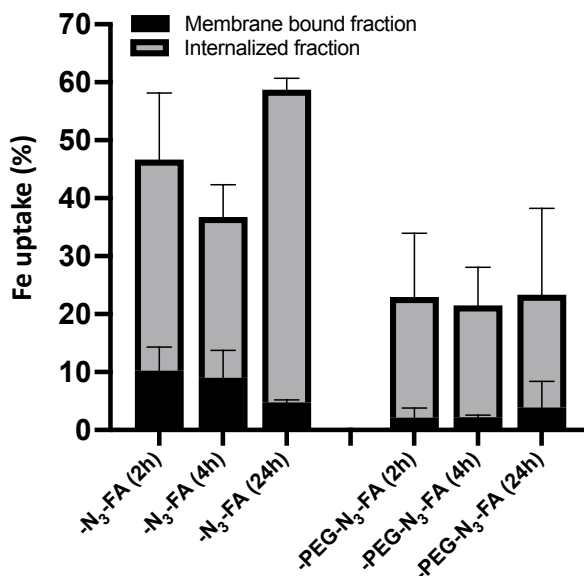


Figure 3.15. Uptake of functionalized SPIONs by the HeLa cells at different incubation times (2, 4 and 24h) determined by ICP-OES. The colors represent: internalized (grey) and membrane-bound fractions (black).

Conclusions

Comparing the two typically applied methods for the manufacturing of SPIONs, thermal decomposition procedure proved the most suitable for the preparation of monodispersed nanoparticles compared to the co-precipitation method. In addition to the small size (6 nm), the resulting nanoparticles showed efficient magnetization, typical for the maghemite-like crystal structures, which in this case was found to be composed of Fe³⁺ ions in tetrahedral and octahedral configuration. The r_2 -relaxivities (85 and 45 mM⁻¹s⁻¹) and magnetic moments (10-11 emu) of the functionalized SPIONs are in agreement with the determined γ -Fe₂O₃ composition.

Conjugation of functional molecules at the surface of SPIONs appeared more efficient when done in two steps: all functional groups were first modified with an APTMS-linker and then

grafted onto the surface of nanoparticles. This strategy not only enables better control over the amounts of each functional molecule on the surface, but also prevents aggregation of the nanoparticles during the surface functionalization. After surface modification, the size of the SPIONs increased only by 2 nm and the resulting positive charges were convenient to maintain a good dispersity.

The preliminary *in vitro* study demonstrated the effect of folic acid on the targeting ability of the SPIONs. Additionally, the presence of PEG-molecules on the surface of nanoparticles was associated with lower cytotoxicity and higher accumulation at the tumor cells compared with the non-PEGylated analogues.

These preliminary results indicate the potential of the designed nanoparticles for image-guided cell targeting and the subsequent click-reaction with the cyclooctyne-functionalized therapeutic as the final goal. Studies further demonstrating the feasibility of this approach are described in the following chapter.

Experimental details

Materials. All reagents and solvents used were of analytical grade, purchased from Sigma-Aldrich. “H₂O” pure was obtained from a Milli-Q System.

Methods. Transmission electron microscopy (TEM) was performed on TEM JEOL JEM-2100 by dispersing samples in ethanol and evaporation over a 400-mesh copper grid. Thermogravimetric analysis (TGA) was conducted by using a Perkin Elmer Thermogravimetric Analyzer from 30 to 850 °C (10 °C/min) under air atmosphere. Dynamic light scattering (DLS) and zeta-potential (ζ) measurements were carried out on Malvern Zetasizer NanoZS. UV Spectra were measured on UV-6300PC VWR Double Beam Spectrophotometer and Fourier-Transform Infrared (FTIR) spectroscopy was performed on FTIR-380 Shimadzu by preparation of samples in KBr pallets. ¹H and ¹³C NMR spectra were acquired with Agilent 400-MR DD2, operating at the frequencies of 399.7 and 100.5 MHz, respectively. Samples were prepared in D₂O or DMSO-d₆ in 5mm NMR tubes. Chemical shifts are reported in ppm referenced to *t*-BuOH (1.2 ppm for ¹H NMR and 31.0 ppm for ¹³C NMR) and TMS (0 ppm), respectively. *T*₂-relaxivity studies were performed using Carr-Purcell-

Meiboom-Gill (CPMG) pulse sequence with variable length if spin-echo train and echo time of 0.5 ms. The obtained spectra were analyzed by three-parameters exponential fit on MNOVA-software. Magnetic studies of functionalized-SPIONs were obtained with a Quantum Design MPMS-XL5 5S SQUID-magnetometer (5T magnet, T = 2-380 K). Additionally, to differentiate between Fe²⁺ and Fe³⁺, Mossbauer Spectrometry was performed. Transmission ⁵⁷Fe Mossbauer spectra were collected at 4.2 K and fitted using the Mosswin 4.0 program. The fluorescence was measured with a confocal fluorescence microscope (Nikon A1R confocal) with 20× magnification and the obtained data was analyzed with FIJI by Image-J software.

Synthesis

Preparation of Si-coated SPIONs (SPIONs-Si). 5 mL of 1M FeCl₃·6H₂O solution were mixed with 1.25 mL of 2M solution of FeCl₂·4H₂O and the mixture was stirred. The initial pH 3 was increased to pH 13 by the addition of 10.5 mL of tetramethylammoniumhydroxide. The obtained mixture was stirred for 20 min while a colour change from orange to black was observed. The finally formed black precipitate was separated using Nd-magnet and washed with Milli-Q water (3×) until pH neutral was reached. The nanoparticles were obtained as a powder by freeze-drying of the final suspension.

0.5785 g of as-prepared SPIONs were dispersed in 20 mL of ethanol and the suspension was sonicated for 1h. Then 0.84 mL of ammonia solution (25%) in 1.875 mL Mili-Q water and 0.14 mL of tetraethylorthosilicate were added to the mixture. Subsequently, vigorous stirring was applied for 2h followed by sonication for 1h. The nanoparticles were separated using a Nd-magnet, dispersed in ethanol and kept for 6h in a water bath at 60 °C. Finally, the coated nanoparticles were again separated with the magnet, washed with ethanol and dried in a desiccator under vacuum over 1 day.

Preparation of oleic acid coated SPIONs (SPIONs-OA). Iron acetylacetonate (Fe(acac)₃) (4 mmol), 1,2-hexadecanediol (20 mmol), oleic acid (12 mmol), oleylamine (12 mmol), and phenyl ether (40 mL) were mixed and magnetically stirred under a flow of nitrogen. The mixture was heated to 200 °C for 2h, then refluxed at 250 °C for another 30 min. The black suspension was cooled to room temperature. Then ethanol (160 mL) was added to the

mixture, and the black precipitate was separated by a Nd-magnet. The product was resuspended in 20 mL of heptane in the presence of oleic acid (50 μ l) and centrifuged (10 krpm, 15 min) to remove any undispersed residue. To get a black solid material, the heptane dispersed nanoparticles were precipitated with ethanol (100 mL), then separated with a Nd-magnet and rinsed with ethanol (3 \times). The final product was dried in a desiccator under vacuum for 2 days.

Preparation of folic acid-APTMS conjugate. Folic acid (44 mg, 0.1 mmol) was dissolved in 1 mL of dry DMSO and 1-ethyl-3-(3-dimethylaminopropyl) carbodiimide hydrochloride (EDC, 38.2 mg, 0.2 mmol) was added to the solution. The mixture was stirred for 3h after which N-hydroxysuccinimide (NHS, 11.5 mg, 0.1 mmol) was added. The mixture was stirred for 24h. After formation of FA-NHS was confirmed (^1H NMR = 2.57 (t, 2H) and ^{13}C NMR = 40.8 and 166.72 ppm), 18 μ L of (3-aminopropyl)trimethoxysilane (APTMS) was added to the solution. The reaction mixture was stirred for 24h at room temperature. The obtained product was analyzed by NMR.

^1H NMR (399.7 MHz, DMSO- d_6): 0.96 (t, 2H), 1.70 (m, 2H), 2.30 (t, 2H), 2.85 (t, 2H), 4.35 (m, 1H), 4.55 (m, 1H), 6.66 (d, 2H), 6.95 (t, 2H), 7.10 (s, 1H), 7.67 (d, 2H), 7.88 (s, 1H), 8.16 (d, 1H), 8.67 (s, 1H), 10.65 (s, 1H). ^{13}C NMR (100.5 MHz, DMSO- d_6): 16.10, 25.60, 26.26, 34.56, 36.92, 40.81, 43.08, 55.34, 111.64, 121.85, 128.34, 129.44, 149.00, 151.18, 154.46, 166.90, 173.20, 174.54, 174.60.

Preparation of azide-APTMS conjugate. 19.8 mg (0.1 mmol) of azido acetic acid NHS ester were dissolved in 0.5 mL of DMSO to which 9 μ L (0.05 mmol) of APTMS were added. The mixture was stirred at room temperature for 18-24h. The obtained product was analyzed by NMR.

^1H NMR (399.7 MHz, DMSO- d_6): 0.35 (t, 2H), 1.49 (m, 2H), 2.08 (s, 2H), 3.10 (t, 2H), 3.20 (s, 9H), 7.75 (s, 1H). ^{13}C NMR (100.5 MHz, DMSO- d_6): 6.04, 26.07, 31.08, 44.77, 50.18, 173.50. 15.4 mg (0.01 mmol) of PEG₃₅₀₀ azide NHS ester were dissolved in 0.5 mL of DMSO and 1.8 μ L (0.004 mmol) of APTMS were added. The mixture was stirred at room temperature for 18-24h. The obtained product was analyzed by NMR.

^1H NMR (399.7 MHz, DMSO-d_6): 0.55 (t, 2H), 1.40 (m, 2H), 2.10 (s, 2H), 3.15 (s, 4H), 3.4 (t, 2H), 3.50 (t, 9H); ^{13}C NMR (100.5 MHz, DMSO-d_6): 6.04, 25.00, 31.00, 47.77, 49.18, 70, 18, 170.50.

Attachment of azide- and folic acid- APTMS-conjugates to NPs. 10 mg of iron-oleate (in 100 μL of heptane) were mixed with 10 mL of toluene. To this mixture, 500 μL of TEA, 10 μL of Milli-Q water and APTMS-conjugates were added, and the reaction mixture was placed in an ultrasonication bath for 5h at 50 $^\circ\text{C}$. After that, 10 mL of heptane were added, and the functionalized nanoparticles were separated by using a Nd-magnet. The obtained nanoparticles were then washed with acetone (3 \times) and dried overnight in a desiccator placed under vacuum.

The number of azide-moieties at the surface of nanoparticles was determined by FTIR using a typical azide-stretching absorption at 2100 cm^{-1} . The measurements were calibrated using sodium azide as a standard material. Folic acid was quantified using UV-spectroscopy by measuring typical peaks at 280 and 360 nm.

Cell culture. HeLa cells (obtained from Erasmus Medical Centre, Rotterdam, The Netherlands) were cultured regularly in T-75 flask using Dulbecco's Modified Eagle Medium (DMEM) containing 10% Fetal Bovine serum (FBS) and 1% Penicillin-Streptomycin (10 mg/mL) until 90% of confluence was reached (5-7 days).

Cytotoxicity assay. HeLa cells (1×10^4 cells per well) in 200 μL of DMEM medium were seeded into a 96-well plate for one day. The next day, the medium in each well was replaced for a fresh medium containing functionalized SPIONs (SPIONs- N_3 -FA and SPIONs-PEG- N_3 -FA) with different concentrations (0-1 mM) and then incubated at 37 $^\circ\text{C}$ with 5% CO_2 for 24h. After the incubation time, 10 μL of CCK-8 solution were added to each well and cells were incubated for another 4h. The absorbance of each well was measured at 460 nm by using a microplate reader (n=5).

Cellular uptake study. HeLa cells (1×10^4 cells per dish) in 250 μL of DMEM medium were seeded into a 35 mm cell culture dish with a glass coverslip (with 15 mm surface area) for 24h. After that, the medium was removed and another fresh medium containing either only phosphate buffered saline (PBS) as control or functionalized SPIONs (at Fe concentration of

0.1 mM) were added to each dish. Cells were incubated at 37 °C with 5% CO₂ for 2, 4 and 24h. Eventually, the cells were washed with PBS (4×) and incubated with CellBrite 568/580 (1:1000×) at 37 °C with 5% CO₂ for 5 min. Membrane staining dye was aspirated out and cells were washed with PBS three times, fixed with 4% paraformaldehyde, and washed again with PBS (3×). 4',6-diamidino-2-phenylindole (DAPI) nucleus staining dye in 1 mL of PBS was added 15-30 min prior to the microscope observation. Subsequently, the uptake of nanoparticles was observed by confocal fluorescence microscope using laser set to 405 nm for DAPI, 488 nm for FITC, and 561 nm for CellBrite 568/580. For the folic acid competition assay, the HeLa cells were incubated first with FA (160 nM) after which the functionalized SPIONs were added, and the above-mentioned uptake evaluations were applied. The fractions of membrane-bound and internalized nanoparticles were determined after incubation of the functionalized SPIONs with the HeLa cells for 2, 4 and 24 h, aspiration of the incubation medium containing nanoparticles and washing the cells with PBS (3×). Subsequently, solution of glycine-HCl (50 mM) at pH 2.8 was added and the cells were incubated for 5 min. Then the glycine fraction was removed and 0.1 M NaOH was added to the cells for another 5 min to disrupt them and release the internalized SPIONs. Both, 'glycine' and 'NaOH' fractions were collected, and the iron content was determined by ICP-OES. Samples were destructed with 1 mL of concentrated HNO₃ (70%). The calibration curve was obtained using Fe absorption standard solutions in the range 0.1-5 mg/mL (n=3).

Acknowledgement

Thanks are due to Dr. Iulian Dugulan and Anton Levering from the Department of Radiation Science and Technology, Delft University of Technology for the Mössbauer spectroscopy and SQUID-based magnetometer measurements, respectively.

References

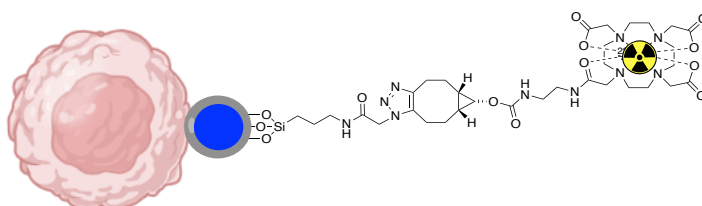
- [1] P. Caravan, *Chemical Society Review* **2006**, *35*, 512-523.
- [2] P. Hermann, J. Kotek, V. Kubicek and I. Lukes, *Dalton Trans* **2008**, 3027-3047.
- [3] D. J. Grootendorst, J. Jose, R. M. Fratila, M. Visscher, A. H. Velders, B. Ten Haken, T. G. Van Leeuwen, W. Steenbergen, S. Manohar and T. J. Ruers, *Contrast Media Molecular Imaging* **2013**, *8*, 83-91.
- [4] Z. R. Stephen, F. M. Kievit and M. Zhang, *Materials Today* **2011**, *14*, 330-338.
- [5] J. Li, Y. Hu, J. Yang, W. Sun, H. Cai, P. Wei, Y. Sun, G. Zhang, X. Shi and M. Shen, *Journal of Materials Chemistry B* **2015**, *3*, 5720-5730.
- [6] M. Arruebo, R. Fernández-Pacheco, M. R. Ibarra and J. Santamaría, *Nano Today* **2007**, *2*, 22-32.
- [7] F. Y. Cheng, C. H. Su, Y. S. Yang, C. S. Yeh, C. Y. Tsai, C. L. Wu, M. T. Wu and D. B. Shieh, *Biomaterials* **2005**, *26*, 729-738.
- [8] J. Park, K. An, Y. Hwang, J. G. Park, H. J. Noh, J. Y. Kim, J. H. Park, N. M. Hwang and T. Hyeon, *Nature Materials* **2004**, *3*, 891-895.
- [9] R. Hachani, M. Lowdell, M. Birchall, A. Hervault, D. Mertz, S. Begin-Colin and N. T. Thanh, *Nanoscale* **2016**, *8*, 3278-3287.
- [10] R. G. López, M. G. Pineda, G. Hurtado, R. D. d. León, S. Fernández, H. Saade and D. Bueno, *International Journal of Molecular Sciences* **2013**, *14*, 19636-19650.
- [11] S. Ge, X. Shi, K. Sun, C. Li, J. R. Baker, M. M. Banaszak Holl and B. G. Orr, *J Phys Chem C Nanomater Interfaces* **2009**, *113*, 13593-13599.
- [12] L. Chen, F. Zang, H. Wu, J. Li, J. Xie, M. Ma, N. Gu and Y. Zhang, *Nanoscale* **2018**, *10*, 1788-1797.
- [13] J. Fang, H. Nakamura and H. Maeda, *Advanced Drug Delivery Reviews* **2011**, *63*, 136-151.
- [14] Y. Chao, G. Chen, C. Liang, J. Xu, Z. Dong, X. Han, C. Wang and Z. Liu, *Nano Letters* **2019**, *19*, 4287-4296.
- [15] R. D. Piazza, W. R. Viali, C. C. dos Santos, E. S. Nunes, R. F. C. Marques, P. C. Morais, S. W. da Silva, J. A. H. Coaquira and M. Jafelicci, *Materials Research Express* **2020**, *7*.

- [16] C. Chen, J. Ke, X. E. Zhou, W. Yi, J. S. Brunzelle, J. Li, E. L. Yong, H. E. Xu and K. Melcher, *Nature* **2013**, *500*, 486-489.
- [17] A. Ali, H. Zafar, M. Zia, I. Ul Haq, A. R. Phull, J. S. Ali and A. Hussain, *Nanotechnology Science Applications* **2016**, *9*, 49-67.
- [18] Y. S. Li, J. S. Church, A. L. Woodhead and F. Moussa, *Spectrochimica Acta Part A* **2010**, *76*, 484-489.
- [19] Y. Han, Z. Lu, Z. Teng, J. Liang, Z. Guo, D. Wang, M. Y. Han and W. Yang, *Langmuir* **2017**, *33*, 5879-5890.
- [20] Y. C. Park, J. B. Smith, T. Pham, R. D. Whitaker, C. A. Sucato, J. A. Hamilton, E. Bartolak-Suki and J. Y. Wong, *Colloids Surf B Biointerfaces* **2014**, *119*, 106-114.
- [21] L. Wortmann, S. Ilyas, D. Niznansky, M. Valldor, K. Arroub, N. Berger, K. Rahme, J. Holmes and S. Mathur, *ACS Applied Materials Interfaces* **2014**, *6*, 16631-16642.
- [22] S. H. Z. D. B. R. S. R. P. M. R. Sun and S. X. W. a. G. Li, *Journal of the American Chemical Society*. **2004**, *126*, 273-279.
- [23] R. A. Harris, P. M. Shumbula and H. van der Walt, *Langmuir* **2015**, *31*, 3934-3943.
- [24] M. Bloemen, W. Brullot, T. T. Luong, N. Geukens, A. Gils and T. Verbiest, *Journal of Nanoparticle Reserach* **2012**, *14*, 1100.
- [25] S. P. Randy De Palma, Margriet J. Van Bael, Heidi Van den Rul, and W. L. Kristien Bonroy, Jules Mullens, Gustaaf Borghs, and Guido Maes, *Chemistry of Materials* **2007**, *19*, 1821-1831.
- [26] G. T. Hermanson in *Chapter 3 - The Reactions of Bioconjugation*, (Ed. G. T. Hermanson), Academic Press, Boston, **2013**, pp. 229-258.
- [27] B. Thapa, D. Diaz-Diestra, J. Beltran-Huarac, B. R. Weiner and G. Morell, *Nanoscale Research Letters* **2017**, *12*, 312.
- [28] P. Burnham, N. Dollahon, C. H. Li, A. J. Viescas and G. C. Papaefthymiou, *Journal of Nanoparticles* **2013**, *2013*, 1-13.
- [29] U. S. Patil, S. Adireddy, A. Jaiswal, S. Mandava, B. R. Lee and D. B. Chrisey, *International Journal of Molecular Sciences* **2015**, *16*, 24417-24450.
- [30] K. Mohammad E, *International Journal of Nanomaterials, Nanotechnology and Nanomedicine* **2017**, 044-050.

- [31] L. Shang, K. Nienhaus and G. U. Nienhaus, *Journal of nanobiotechnology* **2014**, *12*, 5-5.
- [32] G. L. Zwicke, G. A. Mansoori and C. J. Jeffery, *Nano Reviews* **2012**, *3*.
- [33] S. U. Dalm, J. Nonnekens, G. N. Doeswijk, E. de Blois, D. C. van Gent, M. W. Konijnenberg and M. de Jong, *The Journal of Nuclear Medicine* **2016**, *57*, 260-265.

***In vitro* Evaluation of Click-reaction
between Azide-functionalized SPIONs
and DOTA-cyclooctyne**

4



Introduction

Radiotherapy is one of the most effective ways to treat cancer because of its minimally invasive properties and certain flexibility in dose adjustment and, depending on the stage of the disease. However, challenges in the clinical application of internal radionuclide therapy in particular, originate from the immaturity of the radiotherapeutic agents in terms of prompt and exclusive delivery to the tumor site. This requirement becomes especially relevant in the case of short-range-high-energy alpha-emitters, which have great potential for DNA-damage when delivered in close proximity of the cells, both cancerous and healthy.^[1] This is why research into efficient, and above all, safe radiotherapeutics is receiving a lot of attention from scientists. The therapeutic response of the tissues to radiation exposure is complex, and therefore, the accurate delivery of radiotherapeutics is of the utmost concern. Logically, the agents carrying such radionuclides need to have the highest specificity to the tumor cells and high tumor uptake.^[2] It is not surprising that one of the strategies to achieve high-precision radionuclide-therapy is the integration of an imaging modality into the design of targeted treatment. Such an approach, combining imaging and therapeutic components is called *theranostic*.^[3]

Of the various diagnostic modalities available in the clinic, magnetic resonance imaging (MRI) is the most interesting for use in image-guided therapy due to its high soft tissue resolution and lack of ionizing radiation. The latter is especially important in cases where treatment planning requires repeated scans. The principle of MRI is based on the observation of the protons abundant in tissues that differ in terms of density and relaxation behavior when subjected to short radiofrequency pulses in the presence of a strong magnetic field. Therefore, acquisition of an MRI scan is in principle possible without the use of contrast agents (CAs). However, image-guided therapy relies on the *in-situ* confirmation of the presence of the therapeutic probe at the site of interest, which basically means that delivery should be visualized by means of local contrast enhancement. This can be realized by using CAs that alter the relaxation times of the protons in their vicinity. Superparamagnetic iron oxide nanoparticles (SPIONs) are known to shorten the transversal relaxation times (T_2) resulting in negative (dark) contrast.^[4] An additional advantage of

SPIONs, is the possibility to exploit their surface for conjugation with functional molecules, such as tumor receptor-binders^[5] and polyethylene glycol (PEG) that suppresses the immune response.^[6] Synthesis and characterization of SPIONs with the specificity for tumors overexpressing folic acid receptors (FAR) as well as the importance of PEGylation for the cellular uptake are described in Chapter 3. However, the ultimate design of these nanoparticles concerns their application for *in vivo* click-reaction with a small radiotherapeutic molecule. Therefore, the prepared SPIONs were additionally provided with azide- and folic acid (FA) functional groups: SPIONs-FA-N₃ and SPIONs-PEG-FA-N₃.

Fundamentally, click-reactions are featured by several advantages compared to traditional reactions, i.e. fast kinetics in aqueous media and minimal by-products.^[7] An additional property, especially important for biomedical applications, is the bioorthogonality,^[8] meaning that reagents undergo a reaction without competing with endogenous functional groups. A classic representation of a click-reaction is copper catalyzed alkyne-azide cycloaddition (CuAAC).^[9] However, the use of toxic copper as catalyst *in vivo* is ruled out and therefore, utilization of highly strained cyclooctyne derivatives has been presented as an alternative compatible with living organisms.^[10]

In this study, the aforementioned advantages of click-reaction in combination with the tumor specificity of the prepared MRI-active SPIONs were exploited for the design of a two-step tumor targeting approach intended for alpha-radionuclide therapy. The proposed process starts with pretargeting of tumor cells with azide-functionalized SPIONs (step 1), whose delivery to the cell membranes is for now demonstrated by confocal microscopy (Chapter 3), and will eventually be visualized by MRI. After a sufficient amount of nanoparticles has reached the tumor, the radiolabeled cyclooctyne-modified molecule will be injected intravenously (step 2) to undergo a click-reaction with the nanoparticles. This is expected to decrease the radioactive exposure of the healthy organs and minimize the side-effects.^[11] Illustration of this two-step tumor targeting concept is presented in Figure 4.1, along with the molecules involved in the proposed cell recognition mechanism.

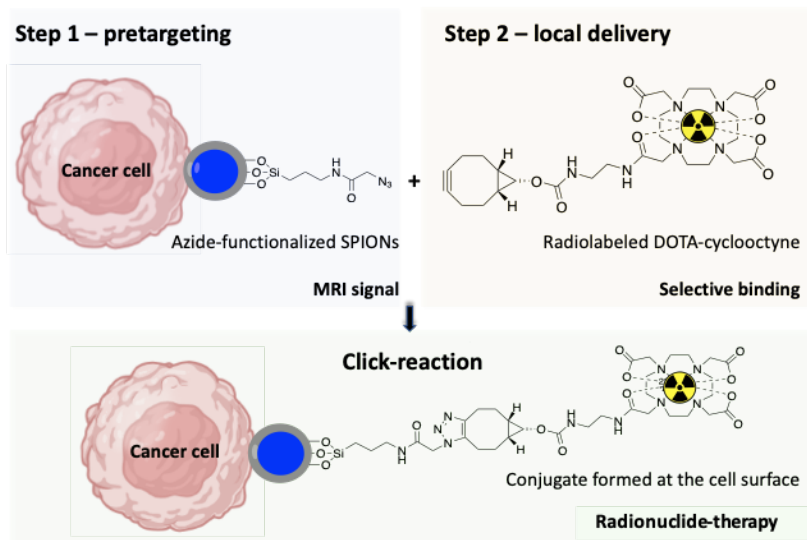


Figure 4.1 Schematic representation of the click-reaction at the surface of azide-functionalized SPIONs with a radiolabeled DOTA-cyclooctyne.

To proof the feasibility of the proposed tumor treatment, the click-reaction was initially tested with 1,4,7,10-Tetraazacyclododecane-1,4,7,10-tetraacetate (DOTA) modified with cyclooctyne (BCN) and complexed with either europium (Eu) or gadolinium (Gd) and 3-aminopropyl triethoxysilane (APTMS) conjugated with an azide-group (APTMS-N₃), as a model for azide-functionalized SPIONs. The goal of this experiment was to confirm the occurrence of the reaction and determine its kinetics using NMR- and UV-monitoring.^[12] Next, the click reaction was performed *in vitro* for which SPIONs were first incubated with U87 glioblastoma cells grown as 3D spheroids, known to closely resemble the actual *in vivo* conditions.^[13] Similar to *in vivo* tumor models, spheroids exhibit an inhomogeneous cell proliferation on the outside and a quiescent central necrotic core, where oxygen and nutrients demand is lower.^[14] After the uptake of SPIONs by the tumor cells had occurred, the ¹¹¹In-DOTA-BCN (¹¹¹In $t_{1/2}$ = 2.8 days) was added, and the radioactivity that remained after the click-reaction on the cell surface was used as a yield indicator for the click-reaction. Additionally, the same experiment was repeated using DOTA-BCN complexed with two radionuclides, ¹¹¹In and ¹⁷⁷Lu ($t_{1/2}$ = 6.7 d) due to their gamma photons (175 and 254 KeV)^[15] and (113 and 208 KeV) are conveniently used for gamma quantification. The latter was used

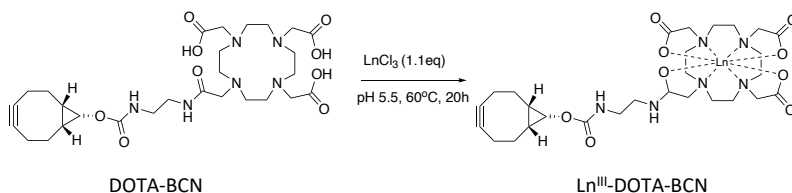
to investigate the therapeutic efficacy and estimate the potential of the proposed two-step targeting approach for the intended alpha-therapy.

Results and Discussion

Progress monitoring of the click-reaction

To investigate the occurrence of copper-free click-reaction in aqueous solution, APTMS- N_3 was used as a model compound for azide-functionalized SPIONs for the reaction with DOTA-cyclooctyne (DOTA-BCN). DOTA-macrocycle was chosen for the complexation of metal-ions due to its high thermodynamic and kinetic stability compared to the linear analogues,^[16] while the complexation as such was necessary to avoid possible charge interferences originating from the free carboxylic groups. Aiming at the final application with an alpha-emitting radioisotope, in this exploratory study DOTA-BCN was complexed with two lanthanides (Ln), Eu and Gd, which enabled NMR- and UV-spectroscopies to be used to monitor the reaction progress.

The complexation of DOTA-BCN (1 eq) with either Eu or Gd (1.1 eq) was done keeping the solution pH at 5.5 and 60 °C for 20h (Scheme 4.1).^[17] The slight excess of Ln-ions, necessary to ensure complete complexation, was removed with Dowex 50w-X8, and the absence of free Ln-ions was confirmed by means of xylenol orange test.^[18] Being a paramagnetic Ln, Eu induces large NMR hyperfine shifts of the protons in a complex with the result that the signals corresponding to the product are accommodated in a large spectral window and can therefore be better identified.^[19] This can be seen in the 1H NMR spectra of both, DOTA-BCN and Eu^{III} -DOTA-BCN depicted in Figure 4.2. The peaks belonging to the DOTA-chelate accommodate within 4 ppm (0.5 to 4.5 ppm, Figure 4.2A), while those of the corresponding Eu-complex are distributed between -18 and 32 ppm (Figure 4.2B).



Scheme 4.1. Complexation reaction between DOTA-cyclooctyne (DOTA-BCN) and $LnCl_3$ (Ln = Eu/Gd).

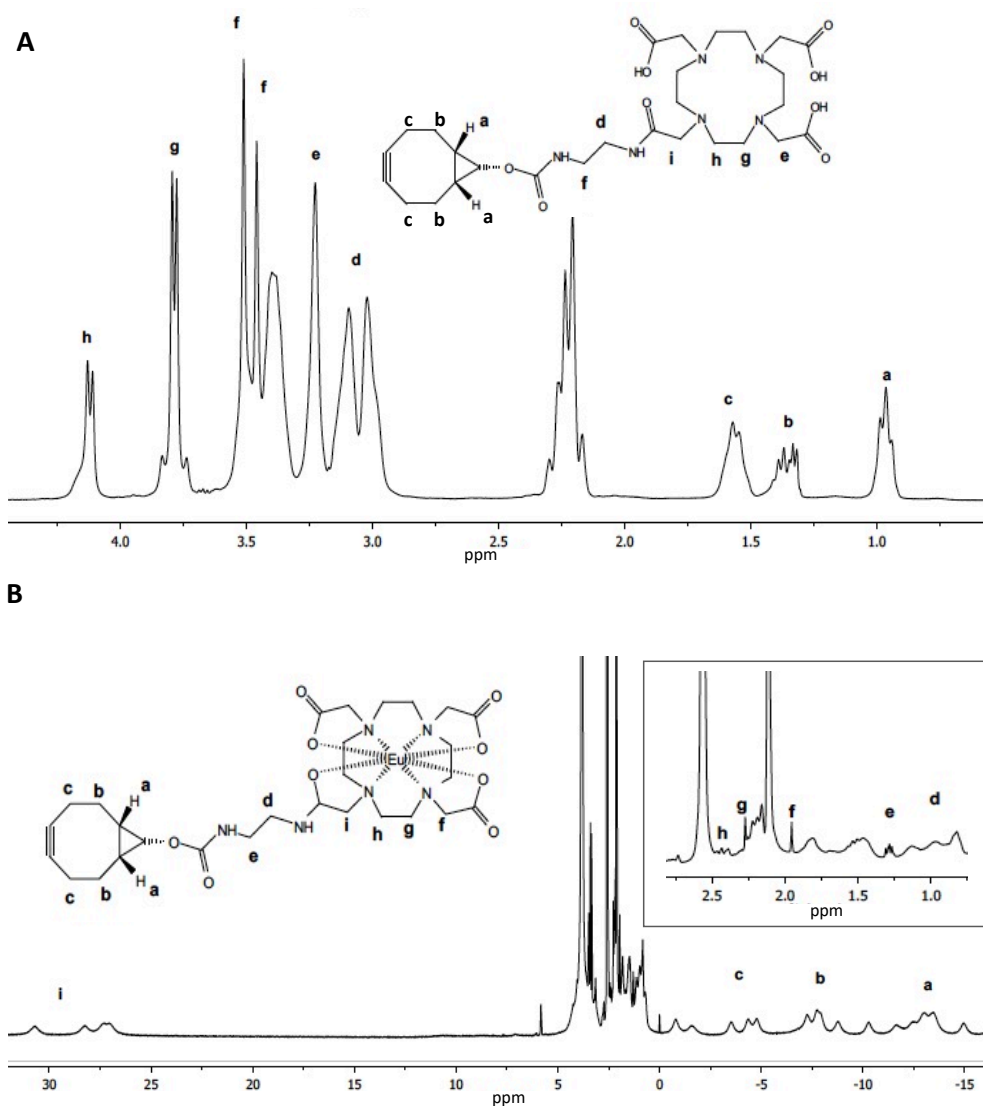


Figure 4.2. ^1H NMR spectra of DOTA-BCN (A) and Eu^{III} -DOTA-BCN (B) in a $\text{D}_2\text{O}/\text{DMSO-d}_6$ mixture.

In the following, the prepared Eu^{III} -DOTA-BCN complex was used in a click-reaction with APTMS- N_3 (Figure 4.3A) at room temperature in a mixture of deuterated water (D_2O) with addition of 5% DMSO-d_6 to enhance the solubility of the reactants. The reaction took place in an NMR tube and formation of the APTMS- Eu^{III} -DOTA-BCN adduct was monitored *in-situ*

by ^1H NMR in the time range from 1 to 240 min (Figure 4.3B). The first spectrum, obtained within 5 min after addition of Eu^{III} -DOTA-BCN, showed the newly appeared peak at 3.0 ppm attributed to the CH_2 group adjacent to the triazole-ring (marked with asterisk, Figure 4.3B). The intensity of the peak continued increasing up to ± 180 min, therefore, this time-range was applied for UV-spectroscopic monitoring.

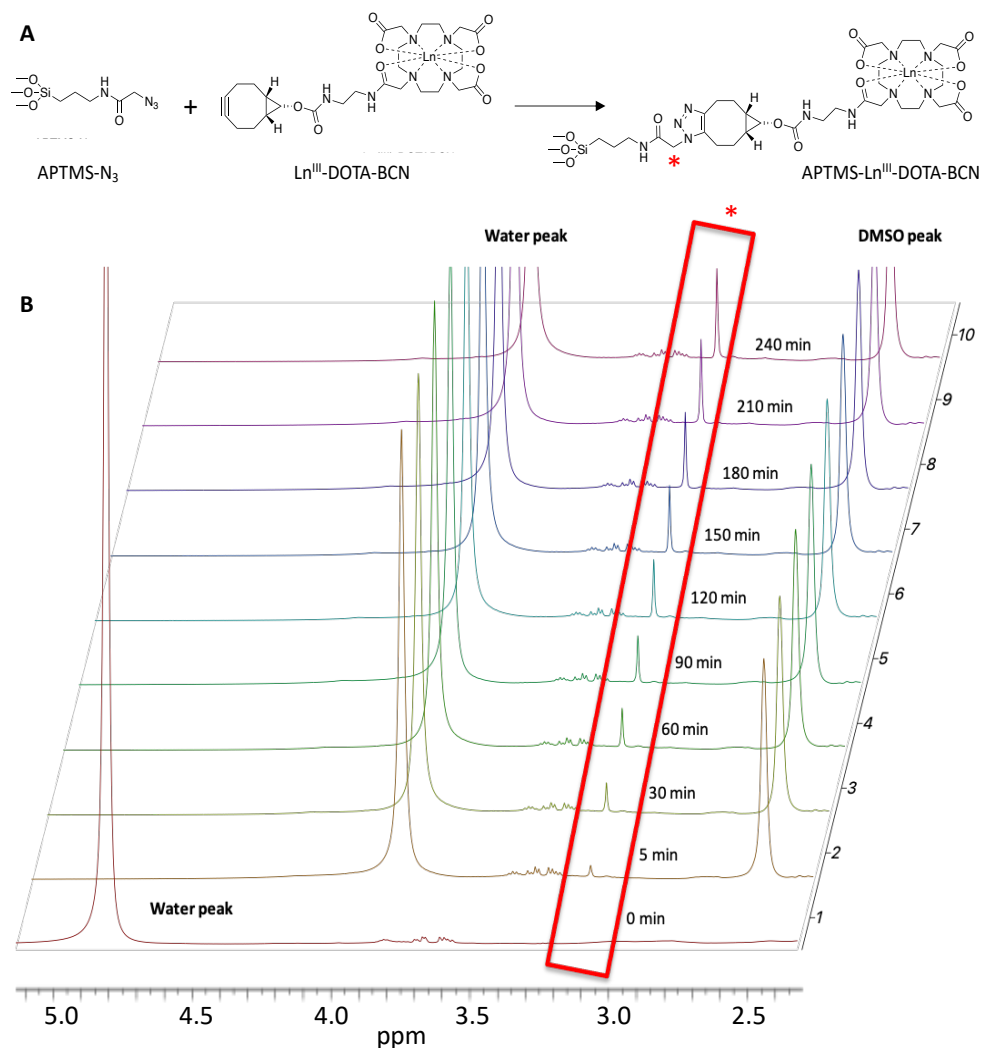


Figure 4.3. ^1H NMR spectra of the click-reaction between APTMS- N_3 and Eu^{III} -DOTA-BCN in $\text{D}_2\text{O}/\text{DMSO-d}_6$ taken in NMR tube at 9.4 T at room temperature.

Advantage of exploiting the UV-absorbance in kinetic studies, is the possibility to acquire spectra with time intervals as small as 1 min. The UV-absorbance spectra of Eu^{III} -DOTA-BCN and APTMS- N_3 are significantly different from that of the reaction product APTMS- Eu^{III} -DOTA-BCN (Figure 4.4). Therefore, shifting of the absorbance curve to lower wavelengths could be attributed to the occurrence of the click-reaction, which was observed already after 1 min (Figure 4.4).

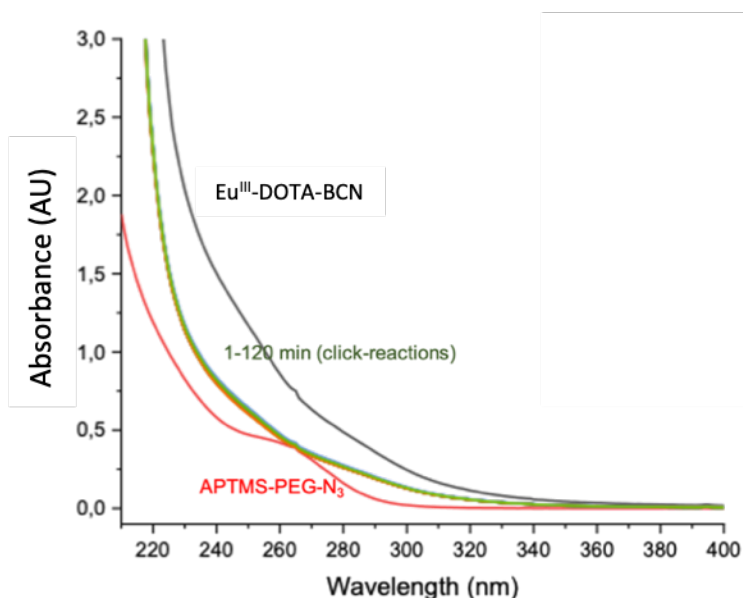


Figure 4.4. UV-absorbance spectra of the click-reaction between APTMS- N_3 and Eu^{III} -DOTA-BCN.

To get insight into the efficiency of the click-reaction in the proposed two-step theranostic system, relaxation behavior of both components separately and after the click-reaction were investigated. Therefore, DOTA-BCN was complexed with paramagnetic Gd and both, the longitudinal (T_1) and transversal (T_2) relaxation times were measured by ^1H NMR at 9.4 T and room temperature. The relaxation rate enhancement relaxivity was expressed as relaxivity ($r_{1/2}$) per mM of paramagnetic substance per second. The same experiment was repeated for the azide-functionalized SPIONs. The Gd-concentration was determined by bulk magnetic susceptibility (BMS) method using a co-axial tube containing $\text{D}_2\text{O}/\text{tBuOH}$ that

was inserted into an NMR-tube containing the sample.^[20] The chemical shift of CH₃-groups of tBuOH present in the sample as well as in the inner tube were measured and inserted in the Eq.4.1 to calculate the Gd-concentration in mM.

$$\Delta_x = \frac{4\pi c S}{T} \left(\frac{\mu_{eff}}{2.84} \right)^2 \times 10^3 \quad 4.1$$

where *C* is the Gd-concentration in mM, *T* is the temperature, *S* is geometrical factor, which is equal to 1/3 in a cylinder parallel to the applied magnetic field, and μ_{eff} is effective magnetic moment of Gd, equal to 7.94.^[21]

Samples containing both PEGylated and non-PEGylated azide-functionalized SPIONs (synthesis described in Chapter 3) were prepared in water containing 0.5% of xanthan as stabilizing medium. Concentration of iron in these samples was determined by ICP-OES. Finally, both components (Gd^{III}-DOTA-BCN and SPIONs) were mixed in a 5 mm NMR tube and *T*₁/*T*₂-relaxation times were measured. The relaxivities corresponding relaxivities were calculated based on Gd and Fe concentrations obtained by BMS and ICP-OES, respectively, used in the Eqs. 4.2 and 4.3, where *T*₁ and *T*₂ are expressed in seconds and Fe/Gd concentrations in mM, thus *r*₁ and *r*₂ are expressed as mM⁻¹s⁻¹. The obtained data is summarized in Table 4.1.

$$\frac{1}{T_1} = r_1 \times [Gd] \quad 4.2$$

$$\frac{1}{T_2} = r_2 \times [Fe] \quad 4.3$$

Table 4.1. *T*₁/*T*₂ relaxivity study of Gd and Fe, as Gd^{III}-DOTA-BCN and azide-functionalized SPIONs, respectively. Before and after click-reaction^a.

Samples	Before click-reaction		After click-reaction	
	<i>r</i> ₁ (mM ⁻¹ s ⁻¹) ^a	<i>r</i> ₂ (mM ⁻¹ s ⁻¹)	<i>r</i> ₁ (mM ⁻¹ s ⁻¹)	<i>r</i> ₂ (mM ⁻¹ s ⁻¹)
1 Gd ^{III} -DOTA-BCN	3.83 ± 0.18	5.03 ± 0.08	6.09 ± 0.09	35.70 ± 1.98
SPIONs-FA-N ₃	1.07 ± 0.01	44.30 ± 1.20		
2 Gd ^{III} -DOTA-BCN	3.83 ± 0.18	5.03 ± 0.08	5.21 ± 0.09	53.53 ± 2.27
SPIONs-PEG-FA-N ₃	1.19 ± 0.01	51.07 ± 7.77		

^a *r*₁ and *r*₂ relaxivities were calculated using the concentrations of Gd and Fe, respectively, as determined by ICP-OES.

The initial r_1 and r_2 values of Gd^{III}-DOTA-BCN of 3.83 mM⁻¹s⁻¹ corresponds well to that of Gd^{III}-DOTA, which is a typical MRI T_1 CA known as Dotarem®.^[22] The same is true for PEGylated and non-PEGylated SPIONs whose r_1 values are very low (around 1 mM⁻¹s⁻¹) and the r_2 values of 44 and 51 mM⁻¹s⁻¹, respectively, are typical for the iron oxide nanoparticles of the sizes around 20 nm,^[23] especially measured at high magnetic fields.^[24] 30 min after the two components were mixed in an NMR tube, the relaxivities were measured again and the results were ascribed to the effect of the adducts formed in the click-reaction on the protons in the solution. The expected increase of the r_1 values was rather modest but could still be explained by the dynamics of the complex slowing down upon binding with the bulky nanoparticle. On the other hand, the r_2 values after click-reaction shows a slight increase of number attributed to the magnetic iron nanoparticles. However, it also observed that the precipitation which occurred after click-reaction with non-PEGylated nanoparticles resulted in a slight decrease of r_2 values. As further increase in the relaxivities was not significant even after 24h, it was decided to implement 30 min reaction time for the following *in vitro* investigations.

Radiolabeling of DOTA-BCN with ¹¹¹In and ¹⁷⁷Lu

The idea to implement alpha-emitting particles was first investigated by using two alternative radioisotopes, ¹¹¹In and ¹⁷⁷Lu, whose decay schemes are depicted in Figure 4.5. As gamma energies of these radionuclides can be easily detected by the automated gamma-counter, their complexes with DOTA-BCN were used to proof the concept of the *in vitro* two-step tumor targeting that is demonstrated further on in Chapter 5 with actinium (²²⁵Ac) as an alpha-emitter.

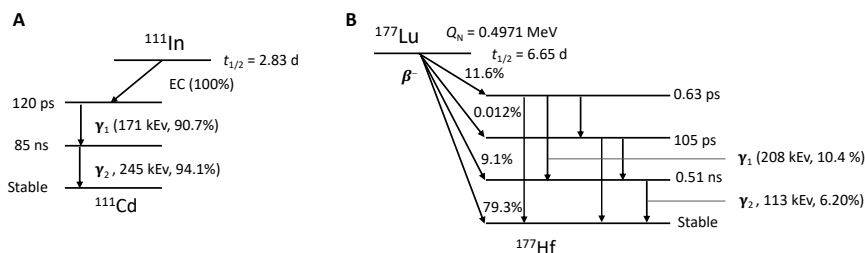
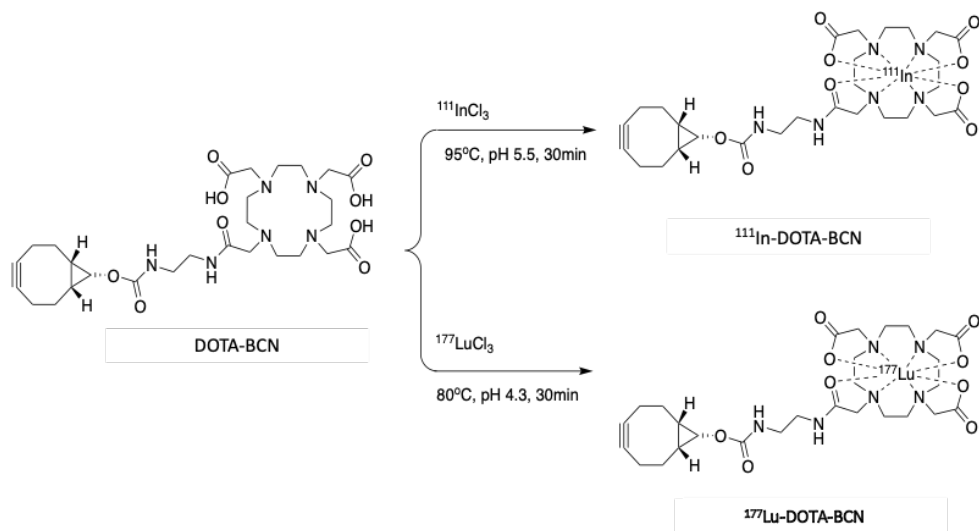


Figure 4.5. The decay schemes of ¹¹¹In (A) and ¹⁷⁷Lu (B).



Scheme 4.2. Radiolabeling of DOTA-BCN with ^{111}In and ^{177}Lu .

Radiolabeling with both, ^{111}In and ^{177}Lu (Scheme 4.2) was performed considering the potential presence of stable decay products ^{111}Cd and ^{177}Hf , respectively, that can interfere with the DOTA-BCN complexation process.^[25] This means that the radiolabeling should be done as close as possible in time to the production of the radioisotope, which is often difficult to realize in practice. Another possibility to avoid such a competition in the complex formation is to increase ligand to radioisotope ratio.^[26] The optimum for ^{111}In radiolabeling was determined experimentally by varying the DOTA-BCN to radiolabel ratios under pH 5.5 and 95°C for 30 min and determining the radiolabeling yields. As it can be seen from Figure 4.6, an excess of the ligand as high as 50:1 should be used for an effective labeling of >95%.

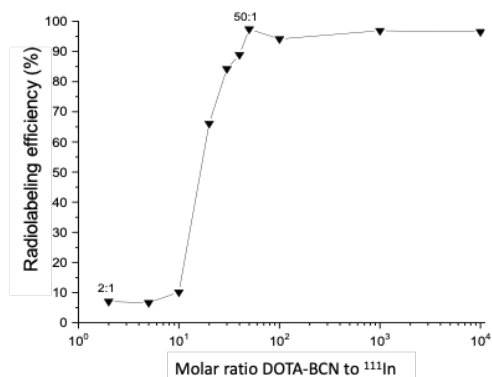


Figure 4.6. The radiolabeling efficiency as a function of the molar ratio of DOTA-BCN to ^{111}In .

Similar concerns are also valid for the labeling of DOTA-BCN with ^{177}Lu since stable ^{177}Hf can act as a competitor during the complexation.^[27] In addition, for the optimum ^{177}Lu -DOTA-BCN radiolabeling, pH 4.3 was applied instead of 5.5^[28] and 1000 times higher DOTA-BCN ligand was used to obtain >95% radiolabeling efficiency.

***In vitro* click-reaction investigated with 3D spheroids**

Overexpression of folic acid receptors (FAR) up to 90% found in brain tumors^[29] has already been demonstrated to be suitable for targeted nanoparticles delivery.^[30] Therefore, in this study, glioblastoma cancer cells (U87) were grown as a 3D spheroidal model and used for the incubation with azide-functionalized SPIONs (step 1) followed by the click-reaction with radiolabeled DOTA-BCN (step 2). As mentioned previously (Chapter 3), advantages of 3D spheroids used in cancer therapeutic studies compared to 2D cell cultures are better mimicking of the actual *in vivo* conditions^[13] and the higher resemblance to primary tumors.^[31]

The concentration of SPIONs that can be tolerated by 3D glioblastoma U87 spheroids was determined by using a Celltiter Glo3D assay, measuring the adenosine triphosphate (ATP) expressed by the viable cells.^[32] Therefore, U87 cells were seeded into a 96-round bottom plate for several days to result in spheroids with sizes of 400-600 μm ^[33]. Different amounts of SPIONs (50-200 $\mu\text{g}/\text{mL}$) with the corresponding Fe-concentrations of 0.1-0.5 mM (based on the ICP-OES measurements) were added and incubated for 24h.

From Figure 4.7, it can be concluded that almost 80% of the U87 glioblastoma cells are still viable even at the concentration of SPIONs up to 200 $\mu\text{g/mL}$. Thereby, no differences in viabilities were detected for the SPIONs with and without PEG on their surface. Based on this viability experiment as well as on that conducted with HeLa cells (reported in Chapter 3), the click-reaction was performed using the concentration of 100 $\mu\text{g/mL}$ of SPIONs.

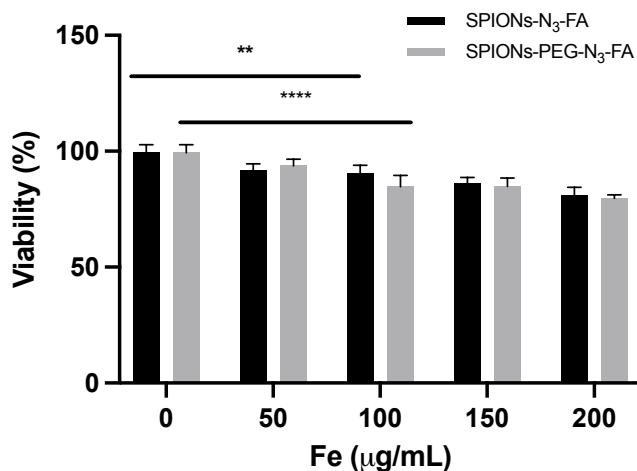


Figure 4.7. Viability study of glioblastoma spheroids by Celltiter Glo3D assay after 24h incubation with SPIONs with (grey) and without (black) PEG on the surface. ** $P < 0.01$; **** $P < 0.0001$.

Cell medium containing 100 $\mu\text{g/mL}$ of azide- and FA-functionalized SPIONs (SPIONs-N₃-FA and SPIONs-PEG-N₃-FA) was added to the spheroids and incubated for 4 and 24h (Figure 4.8A). The spheroids were washed to remove the non-uptaken SPIONs and the Fe content, both internalised and surface-associated, was measured by ICP-OES. About 20 and 40% of iron (100 $\mu\text{g/mL}$ SPIONs) were found in the spheroids after incubation time of 4h with PEGylated and non-PEGylated SPIONs, respectively (Figure 4.8B) and only a slight increase was seen at the longer timepoint of 24h.

Interaction of SPIONs equipped with a fluorescence tag (FITC) was studied with confocal fluorescence microscopy. Figure 4.9 suggests that the accumulation of non-PEGylated (A-B) and PEGylated (C-D) nanoparticles mainly occurs at the edges of the spheroids. Additionally, the data of Fe-uptake (Figure 4.8) indicates no significant differences for PEGylated vs. non-PEGylated SPIONs, especially after 24h of incubation time.

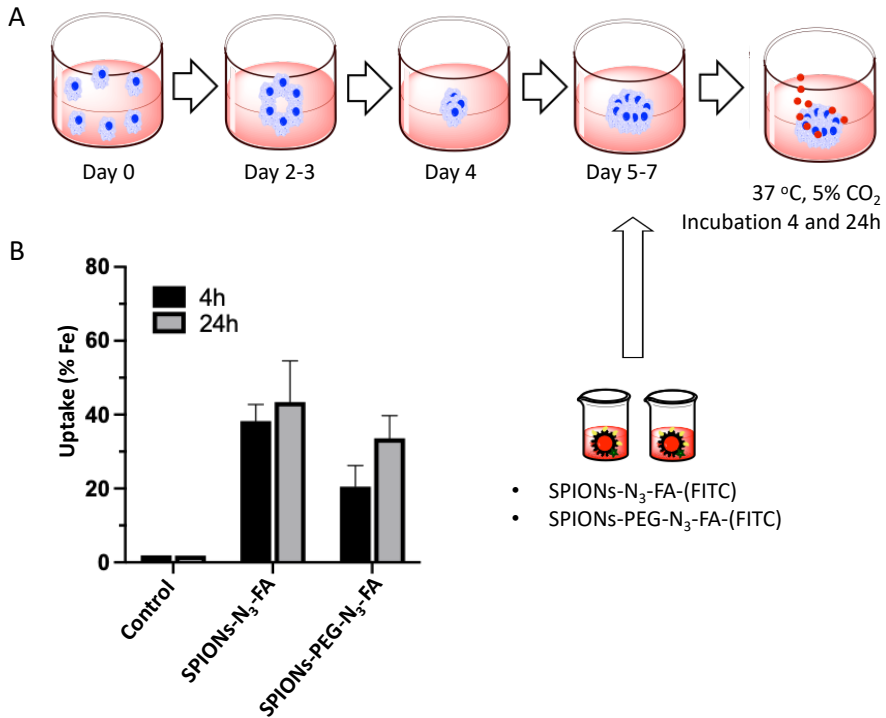


Figure 4.8. Schematic representation of U87 spheroid formation (400-500 μm) followed by incubation with SPIONs (A). Uptake of SPIONs by spheroids presented as percentage of Fe, measured by ICP-OES after 4 and 24h of incubation (B).

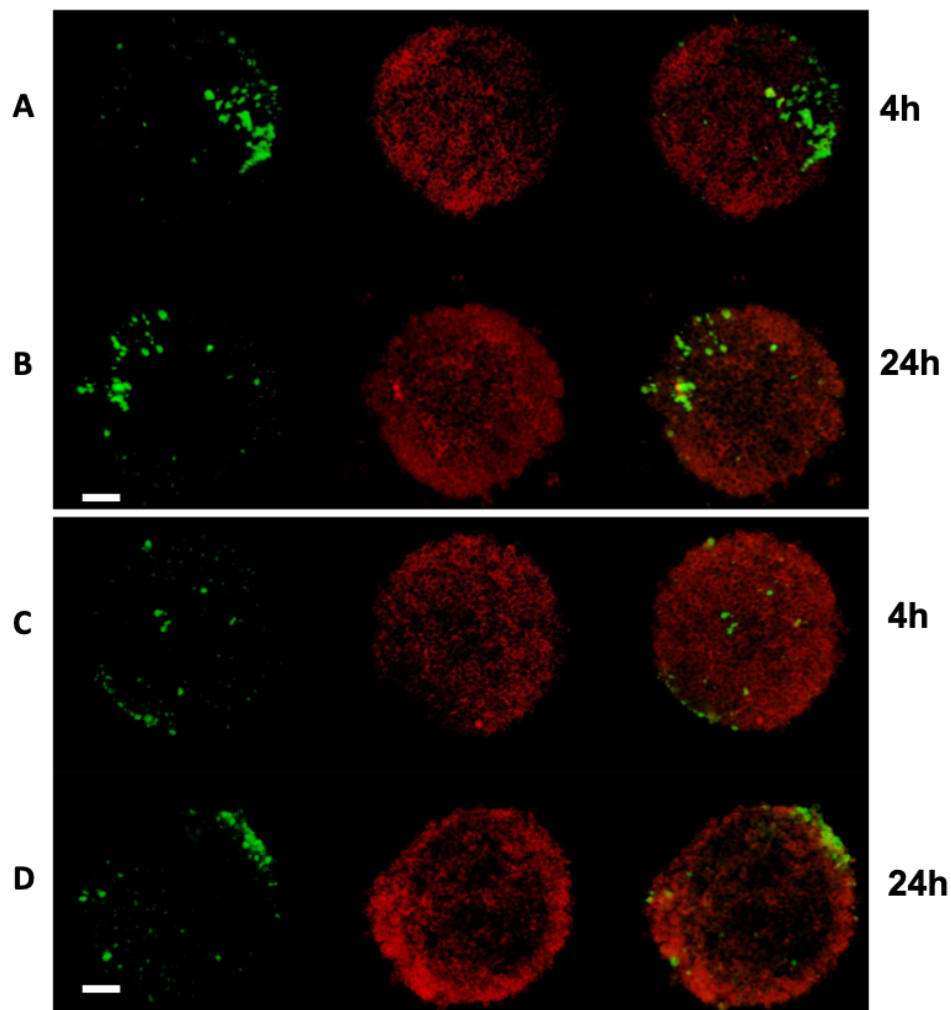


Figure 4.9 Confocal fluorescence microscope imaging of 3D U87 spheroids incubated with SPIONs-N₃-FA-(FITC) (**A-B**) and SPIONs-PEG-N₃-FA-(FITC) (**C-D**) for 4 and 24h. The colors correspond to: FITC (green) and membranes stained with Cellbrite (red), overlaid in the right images. Scale bar is 100 μ m.

To further investigate whether the nanoparticles penetrated to the inside of the spheroid, another batch of spheroids with the size of 400-600 μ m was prepared, incubated with functionalized SPIONs as described above, and after washing, cut by microtome to make slices of 14-20 μ m. A blue marker (DAPI) was added to stain the nucleus in each cryo-slice (Figure 4.10).

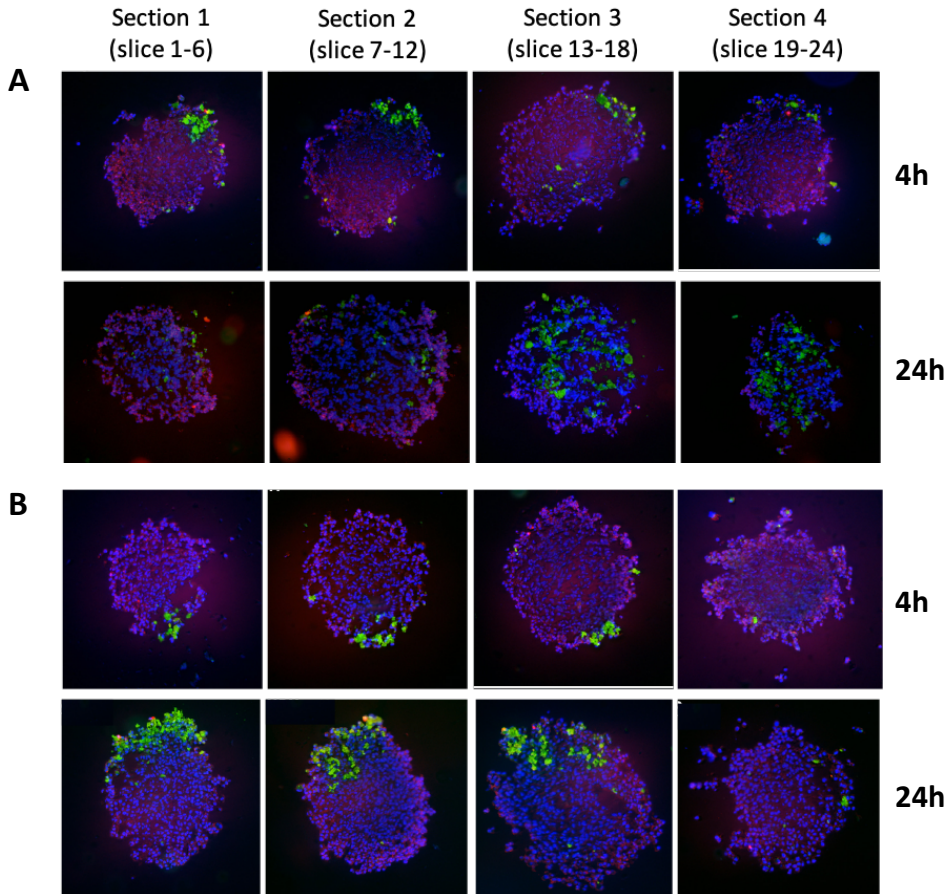


Figure 4.10 Fluorescence microscope imaging of 14-20 μm thick cryo-slices of 3D U87-spheroid incubated with SPIONs-N₃-FA-(FITC) (**A**) and SPIONs-PEG-N₃-FA-(FITC) (**B**) for 4 and 24h. The colors correspond to: FITC (green), nuclei stained with DAPI (blue) and membranes stained with Cellbrite (red).

This time, an extensive green intensity originating from SPIONs incubated for 24h was more evident in every section (1-4) not only at the edges but also in the central part of spheroid obtained in the cryo-slices. It was concluded that, with the longer incubation times some parts of nanoparticles already penetrated inside of the spheroid instead of staying on the outer surface, for both PEGylated and non-PEGylated nanoparticles. However, the character of the observed penetration is rather heterogeneous.

***In vitro* study of the click-reaction between azide-functionalized SPIONs and radiolabeled ^{111}In - and ^{177}Lu -DOTA-BCN**

Based on results obtained with fluorescence microscopy, 4h incubation time was applied to investigate *in vitro* click-reaction between azide-functionalized SPIONs (with and without PEG) and radiolabeled DOTA-BCN. After incubation of nanoparticles and washing out the material that was not taken up by the spheroids, a cell medium containing ^{111}In -DOTA-BCN was added and incubated for another 30 min (Figure 4.11). The percentage of ^{111}In (% relative activity (At/A0)) taken up by the spheroid was determined by automated-gamma counter. A similar *in vitro* of click reaction experiment was also performed for ^{177}Lu -DOTA-BCN to test the therapeutic potential of this approach. For comparison, the click-reactions under the same conditions were performed with 2D HeLa and U87 cells.

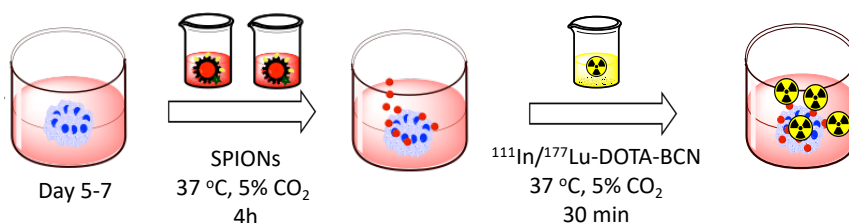


Figure 4.11. Schematic representation of *in vitro* click-reaction between azide-functionalized SPIONs attached to the U87-spheroid and ^{111}In - and ^{177}Lu -DOTA-BCN.

The results, obtained with 3D U87-spheroids demonstrate that 0.14 and 0.2% of ^{111}In - and ^{177}Lu -DOTA-BCN, respectively, stayed at the cell membranes after the click-reaction with the non-PEGylated azide-functionalized SPIONs incubated for 4h (Figure 4.12A). As expected, 24h of incubation of SPIONs results in more cell uptake, and therefore in a lower amount of the radiolabeled compound reacting with the nanoparticles. There appears to be no-significant difference of the accumulation of radiolabeled DOTA-BCN for non-PEGylated and PEGylated SPIONs. These results are in line with previous experiments showing that Fe-uptake in spheroids of non-PEGylated and PEGylated SPIONs are comparable.

On the other hand, the differences between PEGylated and non-PEGylated SPIONs in the click-reaction performed with both ^{111}In - and ^{177}Lu -DOTA-BCN in combination with 2D HeLa and U87 cells are more pronounced (Figure 4.12B). These results are also in accordance to previous experiments in 2D in which cell uptake was more pronounced for the PEGylated nanoparticles. These differences between 2D and 3D can be due to various reasons such as the microenvironment in tumor spheroids^[13] or the fact that the number of seeded cells was 5-fold in the case of a 2D system. In any case, the results demonstrate clearly that the click-reaction occurs within 30 min *in vitro*, which is a good indication of its feasibility for *in vivo* application.

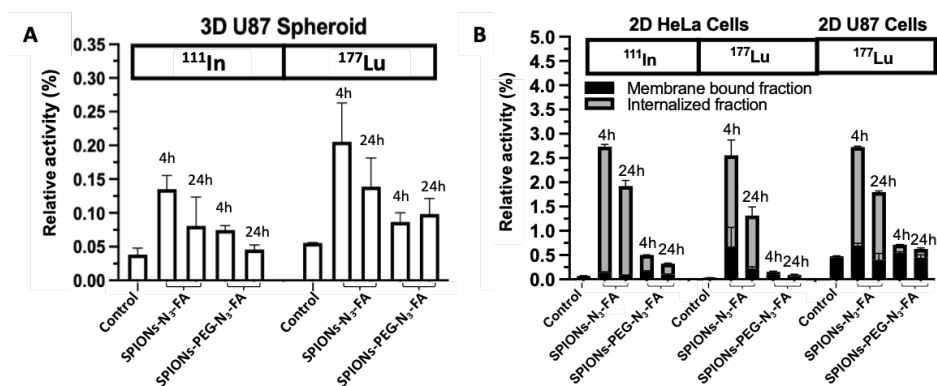


Figure 4.12. Relative activity of ^{111}In - and ^{177}Lu -DOTA-BCN after the click-reaction (30 min) with azide-functionalized SPIONs on the surface of 3D U87 glioblastoma spheroids (A) and 2D HeLa cervix and U87 cancer cells (B).

Therapeutic evaluation of ^{177}Lu -DOTA-BCN after the click-reaction

The next step was to evaluate the therapeutic potential of this approach by using a beta minus -emitter ^{177}Lu prior to its intended application to the alpha-emitter ^{225}Ac .

The therapeutic effect of ^{177}Lu to both, glioblastoma and HeLa cells, grown as 3D spheroids and 2D monolayers, respectively, was investigated by performing the click-reaction between radiolabeled DOTA-BCN offered to the cells at different activities after their incubation with non-PEGylated azide-functionalized SPIONs for 4h. After 30 min the reaction was stopped and the viability of the cells was assessed using Cell titerGlo-3D^[32] and CCK-8^[34] assays (Figure 4.13).

An effect is observed already from 0.1 MBq. At 1 MBq decrease of cell viability to 80% is achieved in 3D glioblastoma spheroid system (Figure 4.13A). However, the same increase in activity (to 1 MBq) resulted in decrease in viability to 40% in the case of 2D cell models, for both U87 and HeLa cells.

Figure 4.14 shows spheroids treated with 1 MBq of ^{177}Lu -DOTA-BCN for 30 min. Thereby, one spheroid did not contain any nanoparticles, while two others were pre-incubated with PEGylated and non-PEGylated azide-functionalized SPIONs. Consequently, the click-reaction took place in the latter two spheroids. The images, taken after washing, demonstrate the significant damage of spheroids treated with SPIONs 24h after the click-reaction occurred. This is evident from the loose cells surrounding the treated spheroids in comparison to the control. Such loose cells are not alive and detach from the spheroid.

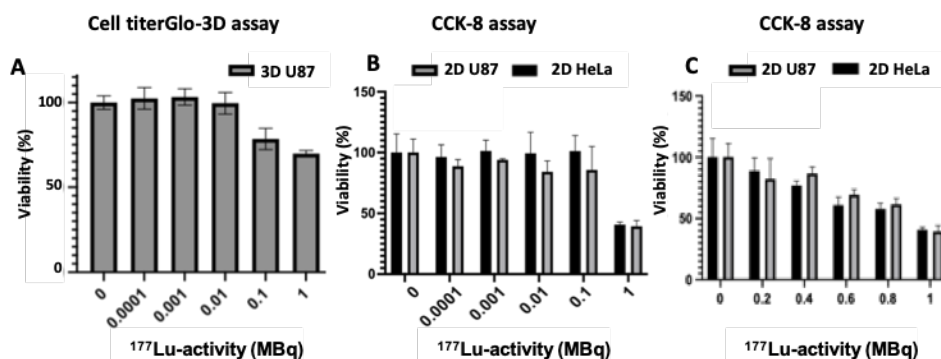


Figure 4.13. Cell viability expressed as percentage to control cells measured after 30 min click-reaction between ^{177}Lu -DOTA-BCN applied for ^{177}Lu activities ranging from 0 to 1 MBq and non-PEGylated azide-functionalized SPIONs pre-incubated for 24h with 3D U87 glioblastoma spheroids (A), and in 2D HeLa and U87 cancer cells (B-C).

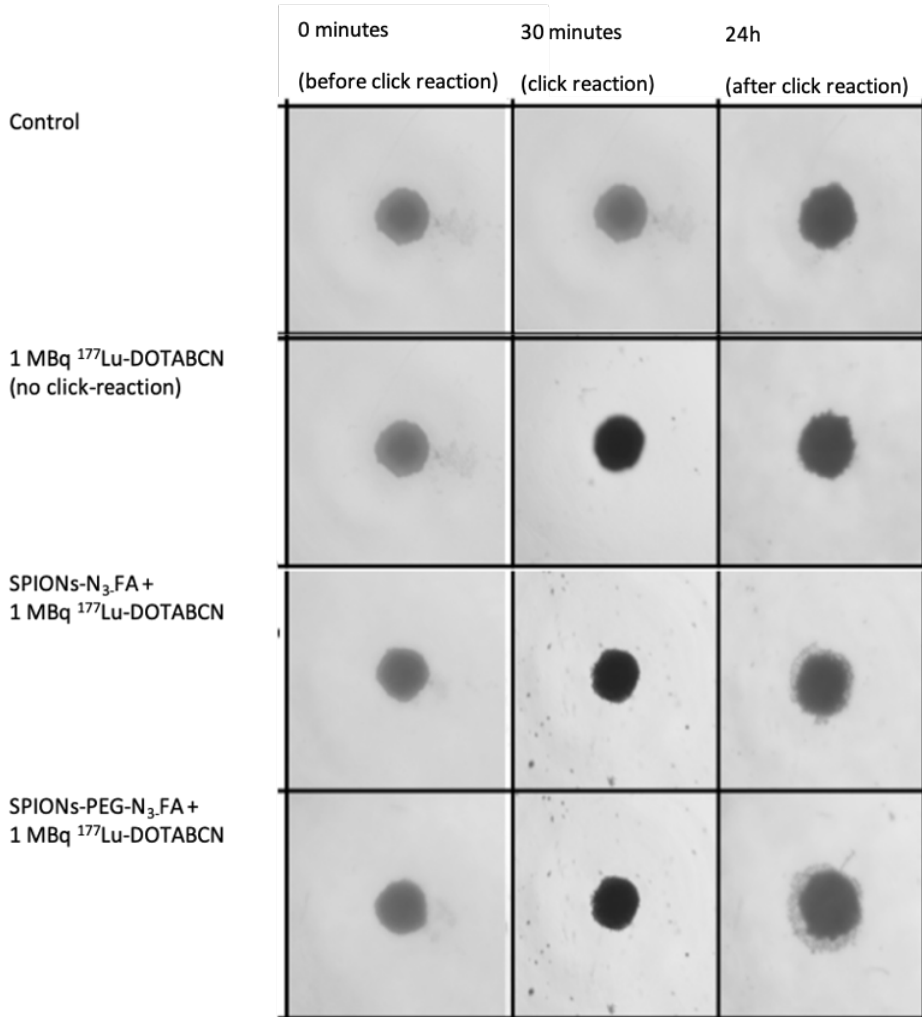


Figure 4.14. Microscope images of the 3D U87 glioblastoma spheroids (with and without pre-incubation with SPIONs) treated for 30 min and 24 h with 1 MBq of ^{177}Lu -DOTA-BCN. Non-treated spheroid is included as control.

Conclusions

The copper-free click-reaction between azide-functionalized SPIONs and radiolabeled DOTA-complexes modified with cyclooctyne moiety was demonstrated *in vitro* on both 3D glioblastoma spheroids and 2D HeLa cancer cells. From the results it can be concluded that the click-reaction occurred within 30 minutes and resulted in maximum radiolabeled-DOTA-BCN uptake of 0.2% and 0.1% in U87 spheroid, after click-reaction with both azide-functionalized SPIONs (SPION-N₃-FA and SPIONs-PEG-N₃-FA). However, this result is a bit different with the ¹¹¹In and ¹⁷⁷Lu uptake in 2D system, which found to be maximum at 2.75% and 0.5% after click-reaction with SPION-N₃-FA and SPIONs-PEG-N₃-FA, respectively.

In 3D tumor model, apparently there is no significant differences on the ¹¹¹In and ¹⁷⁷Lu uptake after the click-reaction with both PEGylated and non-PEGylated nanoparticles compared to different of ¹¹¹In and ¹⁷⁷Lu in 2D system. However, the 3D model resembles to the actual tumor *in vivo* which considers the real condition for the further *in vivo* therapeutic application

In addition, the presence of PEG molecules on the surface of NPs has to be considered in the final design of theranostic systems, since it is expected to improve the biocompatibility of the probes as well as increase their blood-circulation times, and facilitate tumor accumulation by enhanced permeability and retention (EPR) effect.^[35] The incubation time of SPIONs prior to the click-reaction is another point of attention. It was shown that 24h incubation stimulates penetration of the nanoparticles in the spheroid, decreasing the click-reaction yields.

Finally, the therapeutic effect of ¹⁷⁷Lu as a beta-emitter^[34] was evaluated by performing the click-reaction at different activities. The preliminary data suggests that activity of 1MBq is the minimum required for a significant cell damage and leads to a decrease in viability to $\pm 40\%$ level. From these results, we can conclude that this two-step tumor targeting concept is considered promising to be applied for the further radionuclide therapy which is the purpose of the next chapter of this thesis.

Experimental details

Materials and methods. All reagents and solvents used were of analytical and synthesis grade. 1,4,7,10-Tetraazacyclododecane-1,4,7,10-tetraacetate cyclooctyne (DOTA-BCN) was purchased from Chematech (Dijon, France), ammonium acetate (NH_4OAc), ethylenediaminetetraacetic acid (EDTA), gadolinium chloride hexahydrate ($\text{GdCl}_3 \cdot 6\text{H}_2\text{O}$), glycine, hydrochloric acid (HCl) and sodium hydroxide (NaOH) were purchased from Sigma-Aldrich. “ H_2O ” pure was obtained from a Milli-Q System. Iron oxide nanoparticles (SPIONs) were prepared and functionalized as described in Chapter 3.

^1H NMR was performed on Agilent 400-MR DD2, operating at the frequency of 399.7 MHz. Samples were prepared in D_2O or DMSO-d_6 in 5mm NMR tubes. Chemical shifts are reported in ppm referenced to *t*-BuOH (1.2 ppm). UV-spectra were measured with 3 cm quartz cuvettes.

The confocal microscope used was Nikon A1R confocal with 20× magnification and applying laser excitation at 488 and 568/580 nm for FITC and CellBrite, respectively. The obtained data was analyzed by Image-J software using FIJI.

The inverted microscope used was a SZ 45 B zoom Binocular stereo microscope 7x-45x and using 2x magnification. Images were taken using 12 MP camera and analyzed with Samplescan software.

The luminescence spectroscope used was Agilent Technologies Cary Eclipse Spectrophotometer (bio/chemiluminescence data mode) applied at integration time of 0.2–1 second. The emission wavelength and slit used were 600 and 20 nm, respectively.

The count rate of ^{111}In and ^{177}Lu was determined with a Perkin Elmer 2480 automated γ -counter WALLAC using the gamma photons of 175 and 254 KeV, and 113 and 208 KeV for ^{111}In and ^{177}Lu , respectively.

Cryosection of the spheroids was performed with a cryostat Leica CM1900. The cryostat was operated under the following conditions: cryostat temperature -25°C , cutting table temperature -20°C , cutting size was set to 10-20 μm , freezing medium PELCO Cryo-Embedding Compound was used to freeze the samples.

Preparation of Ln(III)-DOTA-BCN. Ln(III)-DOTA-BCN (Ln= Eu and Gd) complexes were synthesized by mixing a DOTA-BCN ligand solution (1 eq) and LnCl₃ solution (1.1 eq) in water. The pH of the mixture was adjusted to 5.5 using a 0.05N solution of NaOH. The reaction mixture was stirred at 60 °C overnight, after which Dowex 50W-X8 resin was added and the stirring was carried on for another 4h to separate the free Ln(III) ions. The absence of free Ln(III) was checked with xylenol orange indicator. The obtained Eu(III)-DOTA-BCN complexes structure were analyzed by ¹H NMR.

¹H NMR and UV click-reaction monitoring. Eu-DOTA-BCN and APTMS-N₃ were dissolved in D₂O and/or DMSO-d₆, transferred to 5 mM NMR tubes and 3 cm cuvettes. The progress of the reaction at room temperature was monitored *in situ* from 0 to 120 and from 0 to 240 min by UV and ¹H-NMR spectroscopies, respectively.

T₁/T₂ relaxation measurements. GdCl₃ in D₂O and 1% (v/v) tBuOH was added as an internal standard to prepared Gadolinium complex (Gd-DOTA-BCN). The Gd concentration was obtained by BMS method.^[20] SPIONs-N₃-FA and SPIONs-PEG-N₃-FA were suspended in water with addition of 0.5 wt% of xanthan at concentrations of 0.1 mg/mL and. To each of this solution 0.8 mmol of Gd-DOTA-BCN was added and the mixture was transferred to 5mm NMR tubes. T₁- and T₂-relaxivities studies were performed using inversion recovery (INVREC) and Carr-Purcell-Meiboom-Gill (CPMG) pulse sequence with variable length if spin-echo train and echo time of 0.5 ms. The obtained spectra were analyzed by three-parameters exponential fit on MNOVA-software (n=3).

Radiolabeling of DOTA-BCN with ¹¹¹In and ¹⁷⁷Lu. ¹¹¹InCl₃ and ¹⁷⁷LuCl₃ were kindly provided by Erasmus Medical Center, Rotterdam, The Netherlands. Radiolabeling of DOTA-BCN with both radionuclides was done in accordance with the previously published method.^[26] For the radiolabeling with ¹¹¹In, 100 μL of a solution containing 0.1 μg of DOTA-BCN in 250 mM NH₄OAc at pH 5.5 were added to 10 μL of an acidic solution of ¹¹¹InCl₃ (1.71 MBq/pmol). For the radiolabeling with ¹⁷⁷Lu, additions involved solution of 0.62 μg of DOTA-BCN (140 μL) dissolved in 250 mM NH₄ONa at pH 4.3 and 10 μL of ¹⁷⁷LuCl₃ (0.714 MBq/pmol). The mixtures were stirred during 30 min at 95 and 80 °C, for ¹¹¹In- and ¹⁷⁷Lu-labeling, respectively. The radiolabeling yield was determined by Thin Layer Chromatography (TLC)

using 0.1M EDTA and 0.1M NH₄OAc (1:1) as the mobile phase with R_f ¹¹¹In-DOTA-BCN and ¹⁷⁷Lu-DOTA-BCN = 0 and R_f ¹¹¹In^{III} and ¹⁷⁷Lu^{III} = 1. The radiolabeling yields were determined by automated γ -counter. XX mL of the solutions of ¹¹¹In-DOTA-BCN and ¹⁷⁷Lu-DOTA-BCN were diluted in PBS (until the desired activity) for *in vitro* click-reaction studies.

Cell cultures. HeLa cervix and U87 glioblastoma cell lines (obtained from Erasmus Medical Centre, Rotterdam, The Netherlands) were cultured regularly in T-75 flask using Dulbecco's Modified Eagle Medium (DMEM) containing 10% Fetal Bovine serum (FBS) and 1% Penicillin-Streptomycin (10 mg/mL) at 37 °C until they reached about 90% of confluency (5-7 days). For all studies, the cells were grown and kept in an incubator at 37 °C under 5% CO₂ atmosphere.

3D spheroid formation. U87 glioblastoma cells (2×10^3 cells per well) in 200 μ L of DMEM medium were seeded into a 96-round bottom well plate and placed in an incubator for 5-7 days to form spheroids. The size of the spheroid was determined by inverted microscopy.

3D Cellular uptake studies with SPIONs. After spheroid formation was confirmed by the inverted microscope, DMEM medium was aspirated out from the well and replaced with fresh medium containing 100 μ g/mL of functionalized-SPIONs (described in Chapter 3). The system was incubated for 4 and 24h. At each end point, the medium was removed, the cells were washed three times with PBS and incubated with Red-CellBrite 568/580 (1:1000 \times) for 5 min. After this, the membrane staining dye was aspirated out and cells were washed again three times with PBS and the iron uptake by spheroid was observed by confocal fluorescence microscope (n=3).

***In vitro* click-reaction between azide-functionalized SPIONs and ¹¹¹In-DOTA-BCN/¹⁷⁷Lu-DOTA-BCN.** U87 spheroids were first incubated for 4h with azide-functionalized SPIONs (see above) and then ¹¹¹In-DOTA-BCN (50 kBq/100 pmol) or ¹⁷⁷Lu-DOTA-BCN (50 kBq/100 pmol) were added and left for another 30 min. Subsequently, the spheroids were washed three times with PBS and collected by using membrane filter. The remaining activities of ¹¹¹In and ¹⁷⁷Lu were determined by automated γ -counter following the protocols established for each radionuclide (n=3).

2D HeLa cells treated with SPIONs were incubated with ^{111}In -DOTA-BCN (50 kBq/100 pmol) or ^{177}Lu -DOTA-BCN (50 kBq/100 pmol) for 30 min. The membrane bound- and internalized SPIONs fractions were determined by glycine treatment in which glycine-HCl (50 mM, pH 2.8) and NaOH 0.1 N were added to the cells consecutively, and the cells were incubated for 5 min. All fractions were collected in Eppendorf tubes and ^{111}In - or ^{177}Lu -activities were measured by automated γ -counter with the corresponding protocols (^{111}In or ^{177}Lu) (n=3).

3D spheroid viability with SPIONs. 3D spheroids with the size of 400-500 μm were incubated in a DMEM medium containing different concentrations (0-1 mM of iron) of functionalized SPIONs (SPIONs- N_3 -FA and SPIONs-PEG- N_3 -FA) for 24h. After this, the medium containing nanoparticles was removed and the spheroids were washed three times with PBS. The number of viable cells in 3D spheroids after the treatment with SPIONs was determined with Celltiter Glo3D assay based on the presence of adenosine triphosphate (ATP). Therefore, the spheroids were incubated for 1h at room temperature with the Celltiter Glo3D reagent and the luminescence was measured (n=5).

Cell viability after ^{177}Lu -DOTA-BCN treatment. 3D spheroids with the size of 400-500 μm were incubated first with SPIONs- N_3 -FA for 24h. Different activities of ^{177}Lu -DOTA-BCN (0-1 MBq) were added and incubated for another 30 min at 37 °C and with 5% CO_2 . Subsequently, the medium was removed and replaced by the Celltiter Glo3D reagent to determine the number of viable cells in the spheroid (n=5).

Similar experiment was also conducted for 2D HeLa and U87. HeLa and U87 cell lines (1×10^4 cells per well) in 200 μL of DMEM medium were seeded into a 96-well plate for a day and after incubated for 24h with SPIONs- N_3 -FA incubation. Different activities of ^{177}Lu -DOTA-BCN (0-1 MBq) were added and incubated for another 30 min at 37 °C and with 5% CO_2 and then the viable cells were determined with CCK-8 assays method (n=5).

Acknowledgement

Thanks are due to Dr. Stephen Eustace from the Department of Biotechnology (TU Delft) for the T_1/T_2 NMR relaxation measurements.

References

- [1] R. M. de Kruijff, H. T. Wolterbeek and A. G. Denkova, *Pharmaceuticals (Basel)* **2015**, *8*, 321-336.
- [2] H. Karacay, P. Y. Brard, R. M. Sharkey, C. H. Chang, E. A. Rossi, W. J. McBride, D. R. Ragland, I. D. Horak and D. M. Goldenberg, *Clinical Cancer Research* **2005**, *11*, 7879-7885.
- [3] S. S. Kelkar and T. M. Reineke, *Bioconjugate Chemistry* **2011**, *22*, 1879-1903.
- [4] S. Laurent, L. V. Elst and R. N. Muller, *The Chemistry of Contrast Agents in Medical Magnetic Resonance Imaging* **2013**, 427-447.
- [5] J. D. Byrne, T. Betancourt and L. Brannon-Peppas, *Advanced Drug Delivery Reviews* **2008**, *60*, 1615-1626.
- [6] J. V. Jokerst, T. Lobovkina, R. N. Zare and S. S. Gambhir, *Nanomedicine (Lond)* **2011**, *6*, 715-728.
- [7] H. C. Kolb, M. G. Finn and K. B. Sharpless, *Angewandte Chemie International Edition* **2001**, *40*, 2004-2021.
- [8] H. Y. Yoon, H. Koo, K. Kim and I. C. Kwon, *Biomaterials* **2017**, *132*, 28-36.
- [9] C. P. Ramil and Q. Lin, *Chemical Communications (Cambridge)* **2013**, *49*, 11007-11022.
- [10] P. V. Chang, J. A. Prescher, E. M. Sletten, J. M. Baskin, I. A. Miller, N. J. Agard, A. Lo and C. R. Bertozzi, *Proceedings of the National Academy Sciences U S A* **2010**, *107*, 1821-1826.
- [11] J. Y. Choi and B. C. Lee, *Nuclear Medicine Molecular Imaging* **2015**, *49*, 258-267.
- [12] K. Yamagishi, K. Sawaki, A. Murata and S. Takeoka, *Chemical Communications (Cambridge)* **2015**, *51*, 7879-7882.
- [13] M. Kapalczynska, T. Kolenda, W. Przybyla, M. Zajaczkowska, A. Teresiak, V. Filas, M. Ibbs, R. Blizniak, L. Luczewski and K. Lamperska, *Archives of Medical Science* **2018**, *14*, 910-919.
- [14] M. Millard, I. Yakavets, V. Zorin, A. Kulmukhamedova, S. Marchal and L. Bezdetnaya, *International Journal of Nanomedicine* **2017**, *12*, 7993-8007.
- [15] R. Membreno, B. E. Cook, K. Fung, J. S. Lewis and B. M. Zeglis, *Molecular Pharmaceutics* **2018**, *15*, 1729-1734.

- [16] J. M. Idee, M. Port, C. Robic, C. Medina, M. Sabatou and C. Corot, *Journal of Magnetic Resonance Imaging* **2009**, *30*, 1249-1258.
- [17] A. Pasha, M. Lin, G. Tircso, C. L. Rostollan, M. Woods, G. E. Kiefer, A. D. Sherry and X. Sun, *Journal of Biological Inorganic Chemistry* **2009**, *14*, 421-438.
- [18] A. Barge, G. Cravotto, E. Gianolio and F. Fedeli, *Contrast Media and Molecular Imaging* **2006**, *1*, 184-188.
- [19] G. J. Stasiuk and M. P. Lowe, *Dalton Trans* **2009**, 9725-9727.
- [20] D. M. Corsi, C. Platas-Iglesias, H. v. Bekkum and J. A. Peters, *Magnetic Resonance in Chemistry* **2001**, *39*, 723-726.
- [21] J. A. Peters, J. Huskens and D. J. Raber, *Progress in Nuclear Magnetic Resonance Spectroscopy* **1996**, *28*, 283-350.
- [22] S. Aime, M. Botta, M. Fasano and E. Terreno, *Chemical Society Reviews* **1998**, *27*, 19-29.
- [23] J. Li, Y. Hu, J. Yang, W. Sun, H. Cai, P. Wei, Y. Sun, G. Zhang, X. Shi and M. Shen, *Journal of Materials Chemistry B* **2015**, *3*, 5720-5730.
- [24] I. Fernández-Barahona, M. Muñoz-Hernando, J. Ruiz-Cabello, F. Herranz and J. Pellico, *Inorganics* **2020**, *8*.
- [25] U. O. Häfeli, J. Yu, F. Farudi, Y. Li and G. Tapolsky, *Nuclear Medicine and Biology* **2003**, *30*, 761-769.
- [26] W. A. Breeman, M. De Jong, T. J. Visser, J. L. Erion and E. P. Krenning, *European Journal of Nuclear Medicines and Molecular Imaging* **2003**, *30*, 917-920.
- [27] F. José de Souza Caldeira, *Journal of Chemistry and Chemical Engineering* **2016**, *10*.
- [28] R. Bhardwaj, H. T. Wolterbeek, A. G. Denkova and P. Serra-Crespo, *EJNMMI Radiopharmacy and Chemistry* **2019**, *4*, 13.
- [29] P. S. Low and S. A. Kularatne, *Current Opinion in Chemical Biology* **2009**, *13*, 256-262.
- [30] E. McCord, S. Pawar, T. Koneru, K. Tatiparti, S. Sau and A. K. Iyer, *ACS Omega* **2021**, *6*, 4111-4118.
- [31] A. Nyga, U. Cheema and M. Loizidou, *Journal of Cell Communications and Signaling* **2011**, *5*, 239-248.

- [32] M. Zanoni, F. Piccinini, C. Arienti, A. Zamagni, S. Santi, R. Polico, A. Bevilacqua and A. Tesei, *Scientific Reports* **2016**, *6*, 19103.
- [33] S. Chandrasekaran, *Journal of Bioengineering and Biomedical Science* **2012**, *02*.
- [34] S. Poty, K. Mandleywala, E. O'Neill, J. C. Knight, B. Cornelissen and J. S. Lewis, *Theranostics* **2020**, *10*, 5802-5814.
- [35] L. Chen, F. Zang, H. Wu, J. Li, J. Xie, M. Ma, N. Gu and Y. Zhang, *Nanoscale* **2018**, *10*, 1788-1797.

Introduction

Alpha radionuclide therapy is under intensive investigation in oncology as a very promising treatment for cancer.^[1] Due to the short penetration depth of alpha-particles (0.1 mm) and their high linear energy transfer (50-250 keV/ μm),^[2] they are capable of depositing their energy very locally, leading to direct damage of the DNA. The damage of the surrounding healthy tissues remains limited provided that specific local delivery with minimal blood-circulation time can be achieved.^[3] Therefore, a successful alpha radionuclide therapy requires an effective and fast targeted delivery of radiopharmaceuticals. Several alpha-emitters with convenient half-lives are currently under investigation, such as astatine-211 (^{211}At , 7.2h),^[4] bismuth-213 (^{213}Bi , 45.6 min),^[5] radium-223 (^{223}Ra , 11.4 d)^[6] and actinium-225 (^{225}Ac , 10.0 d).^[1] The latter radionuclide is particularly interesting for the application in cancer therapy.^[7] The decay of ^{225}Ac leads to generation of six daughter radionuclides: ^{221}Fr ($t_{1/2} = 4.8 \text{ m}$), ^{217}At ($t_{1/2} = 32.3 \text{ ms}$), ^{213}Bi ($t_{1/2} = 45.6 \text{ m}$), ^{213}Po ($t_{1/2} = 4.2 \mu\text{s}$), ^{209}Tl ($t_{1/2} = 2.2 \text{ m}$), and ^{209}Pb ($t_{1/2} = 3.25 \text{ h}$), and ^{209}Bi as a stable isotope (Figure 5.1).^[8]

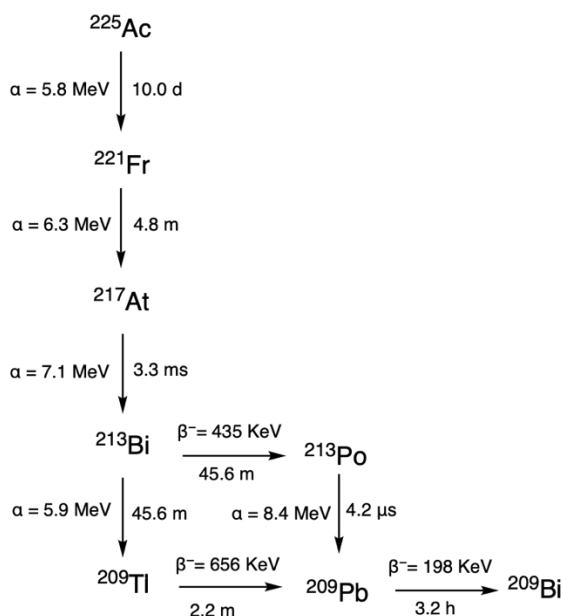


Figure 5.1. The decay scheme of the alpha-emitter ^{225}Ac ($t_{1/2} = 10.0 \text{ d}$) ending at the stable isotope ^{209}Bi .^[8]

However, the challenge of using ^{225}Ac is the release of its daughters due to the recoil effect resulting from the alpha emission. The energy that the recoiling daughter receives is above 100 keV, which results in breaking of chemical bonds. Some of the daughters such as ^{221}Fr and ^{213}Bi (i.e. ^{213}Po) are long-lived alpha emitters as well,^[3] and therefore, their release can damage healthy tissues and organs.^[9]

Therefore, in the case of alpha-radionuclide therapy it is very important to deliver the right dose to the site of interest very fast and selectively preventing harm to healthy tissues. Image-guided delivery of therapeutics using Magnetic Resonance Imaging (MRI) with superparamagnetic iron oxide nanoparticles (SPIONs)^[10] for the contrast enhancement offers this possibility.

As described in the previous chapter, the advantages of the click-reaction^[11] method in combination with the tumor specificity of the prepared MRI-active SPIONs has been exploited for the design of a two-step tumor targeting. This two-step tumor targeting concept *via* click-reaction has been evaluated using two different radionuclides^[12] namely ^{111}In ($t_{1/2} = 2.8$ d) and ^{177}Lu ($t_{1/2} = 6.7$ d),^[13] and proven to be promising for further therapeutic applications.

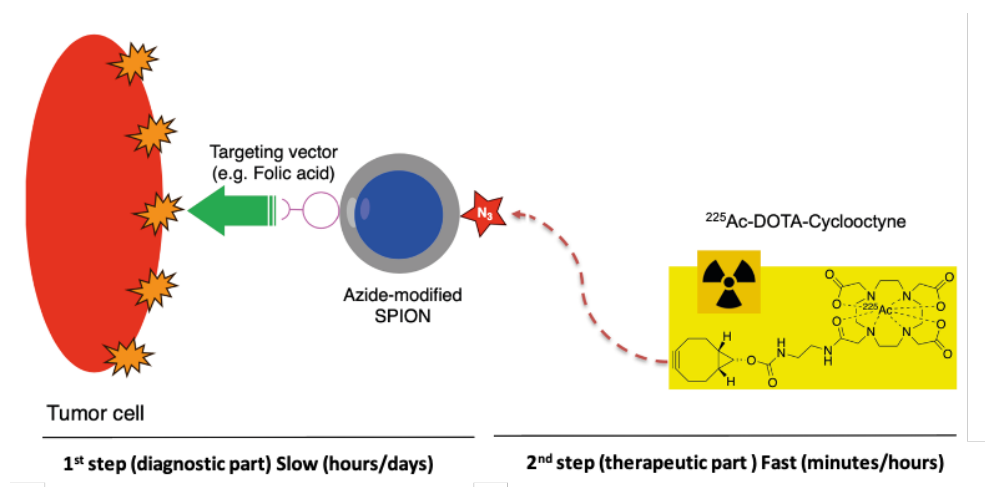


Figure 5.2. Schematic representation of the two-step tumor targeting process utilizing the alpha emitting radionuclide ^{225}Ac .

This last chapter focuses on evaluation of *in vitro* click-reaction with an alpha-emitting radionuclide complex functioning as a therapeutic modality. Once a sufficient amount of tumor targeting SPIONs is accumulated at the tumor site, the second step is performed by the injection of the alpha-therapeutic agent (Figure 5.2).^[14] The whole process aims to be visualized by MRI. As the particles are not expected to re-enter the bloodstream after targeting the tumor via folic acid vector, the therapeutic effect will only be applied locally and the damage of healthy tissues can be limited. Small nanoparticles (<10nm) were also found to have limited uptake in the liver and spleen and fast elimination through kidneys.^[15] The chelator DOTA (1,4,7,10-tetraazacyclododecane-1,4,7,10-tetraacetic acid) complexed with metal ions (for instance, gadolinium) has a thermodynamic stability constant that is 100 to 1000 times greater than that of diethylenetriamine pentaacetate (DTPA) derivatives. The kinetic stability of many metal macrocyclic complexes was also found to be much higher than that of linear chelators.^[16] This is why DOTA was chosen for the complexation of ²²⁵Ac to serve as a therapeutic modality, while its functionalization with an cyclooctyne group enables the click-reaction with SPIONs decorated with azide groups on their surface (prepared on the previous chapter). ²²⁵Ac-DOTA provided with an cyclooctyne functionality this small molecule is expected to accumulate at the site of interest for a time sufficient to achieve the required therapeutic effect.

To further investigate the therapeutic outcome of alpha emitter ²²⁵Ac *via* click-reaction, 3D glioblastoma spheroids were utilized and their growth was followed. In addition, uptake studies of ²²⁵Ac were also carried out and compared to the uptake in 2D cell pallets. Finally, the damage to DNA caused by ²²⁵Ac for two different activities of 1 and 10 kBq was determined by applying a γ -H2AX marker in a 3D tumor model.^[17]

Results and Discussion

Radiolabeling ²²⁵Ac-DOTA-BCN

Radiolabeling of DOTA-BCN with ²²⁵Ac was performed at 90 °C and pH 5.5, which was reported in literature as the most optimal conditions.^[18] In addition, 0.2% of ascorbic acid was used during the labeling procedure to prevent radiolysis of the ligand DOTA-BCN due

to the high energy of the alpha particles.^[19] The highest efficiency of the radiolabeling (>95%) was achieved using 100000 times higher DOTA-BCN ligand to ^{225}Ac ratio and the calculated specific activity (SA) was 5 kBq/nmol of DOTA-BCN.

Uptake of ^{225}Ac -DOTA-BCN in U87 glioblastoma cells after click-reaction

The binding of ^{225}Ac -DOTA-BCN to the azide-functionalized SPIONs in the 2D and 3D glioblastoma cells was investigated after 30 min of the click-reaction, which was determined to be the optimum time (see Chapter 4). An automated-gamma counter was used to determine the percentage ^{225}Ac (At/A0) bound to the U87 glioblastoma cells, grown in 2D pallets as well as in spheroids. As shown in Figure 5.3, there is no significant difference between azide-functionalized SPIONs with or without polyethylene glycol (SPIONs- N_3 -FA and SPIONs-PEG- N_3 -FA). Additionally, when ^{225}Ac -DOTA-BCN was added to the cells without pre-incubation with SPIONs (control), the low accumulation of ^{225}Ac can be seen clearly when compared to cells incubated with nanoparticles first. These results were observed in both 2D cells and 3D spheroids, confirming that the click-reaction took place.

Evidently, the difference in the number of seeded cells in the case of 2D and 3D models, as well as the complex nature of the spheroids, play a role in the maximum of ^{225}Ac accumulation being in line with the results obtained with ^{111}In and ^{177}Lu , as shown in the previous chapter. These results demonstrate that the click-reaction occurs already within 30 min of incubation with the alpha-radiotherapeutic agent.

Interestingly, in the case of the 2D system incubated with both PEGylated and non-PEGylated SPIONs, around 0.6% of ^{225}Ac was still found on the membrane after the click-reaction happened. However, the amount of ^{225}Ac internalized after the click-reaction had taken place was slightly different between the two types of SPIONs. It appears that the PEGylated nanoparticles reduce the uptake of ^{225}Ac suggesting that a larger number of nanoparticles was internalized.

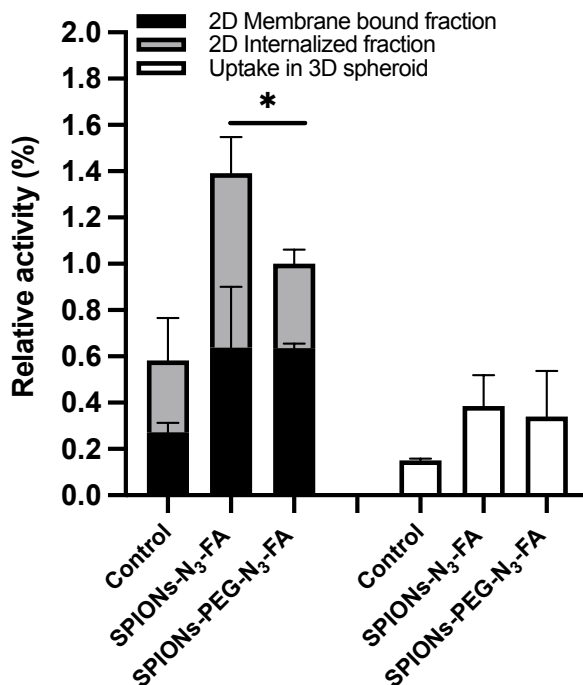


Figure 5.3. The relative activity found in the U87 glioblastoma cells (2D and 3D spheroids) after click-reaction (30 min) between the azide-functionalized SPION present on the cell surface and ²²⁵Ac-DOTA-BCN. In the control experiment, cells were incubated with ²²⁵Ac-DOTA-BCN only. All experiments were conducted in triplicate (n=3). Bars represent mean±SD; *P < 0.05.

²²⁵Ac-DOTA-BCN cells killing efficiency

²²⁵Ac ($t_{1/2} = 10.0$ days, $E_{\alpha} = 5.8$ MeV) emits four alpha- and three beta-particles before decaying to the stable isotope ²⁰⁹Bi. One radionuclide, therefore, delivers an energy of around 28 MeV making it very efficient in cell killing even at very low concentrations. The cell killing effect of different ²²⁵Ac-DOTA-BCN activities after 30 min of click-reaction was evaluated based on the viability test in both 3D tumor models and 2D cell pallets (Figure 5.4).

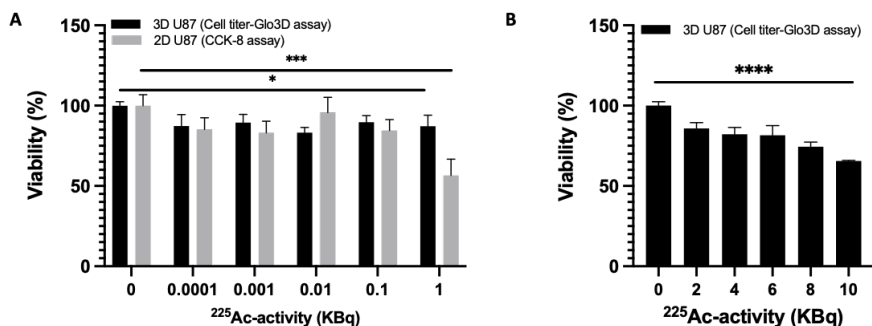


Figure 5.4 The cell killing efficiency of ^{225}Ac -DOTA-BCN after the click-reaction (30 min) with azide-functionalized SPIONs (SPIONs- N_3 -FA) in 2D and 3D spheroids of U87 glioblastoma cells: **A**) using activities from 0 to 1 kBq and **B**) using activities up to 10 kBq; * $P < 0.05$; *** $P < 0.001$; **** $P < 0.0001$.

From Figure 5.4A, it is clear that 1 kBq of ^{225}Ac -DOTA-BCN is already enough for killing around 50% ($55 \pm 10\%$) of the 2D glioblastoma cells, but this activity has little effect on the 3D spheroids. The number of viable cells in the spheroid was found to be higher than 80% ($87 \pm 1\%$) compared to the cells non-treated with ^{225}Ac -DOTA-BCN. A possible reason for this effect can be due to differences in the distribution of ^{225}Ac -DOTA-BCN between the 2D and 3D models. Although SPIONs do accumulate better after 24h of incubation, their distribution is rather non-homogenous, which on its turn influences the binding of ^{225}Ac -DOTA-BCN. To observe an effect in the 3D models, the activity was further elevated to 10 kBq. This increase in activity has led to reduction of the vital cells to $66 \pm 1\%$ (Figure 5.4B). Based on these experiments it was decided to continue with the activities of 1 and 10 kBq applied to the 3D models, which come closest to the actual *in vivo* tumor conditions.^[20]

Spheroid growth observation

To further investigate the effect of ^{225}Ac -DOTA-BCN upon the click-reaction with azide-functionalized SPIONs, the spheroids growth was followed for 30 days. Figure 5.5A, shows that the cytotoxic effect of ^{225}Ac -DOTA-BCN is much higher after click-reaction with pretargeted cells as compared to cells treated with ^{225}Ac -DOTA-BCN only (control).

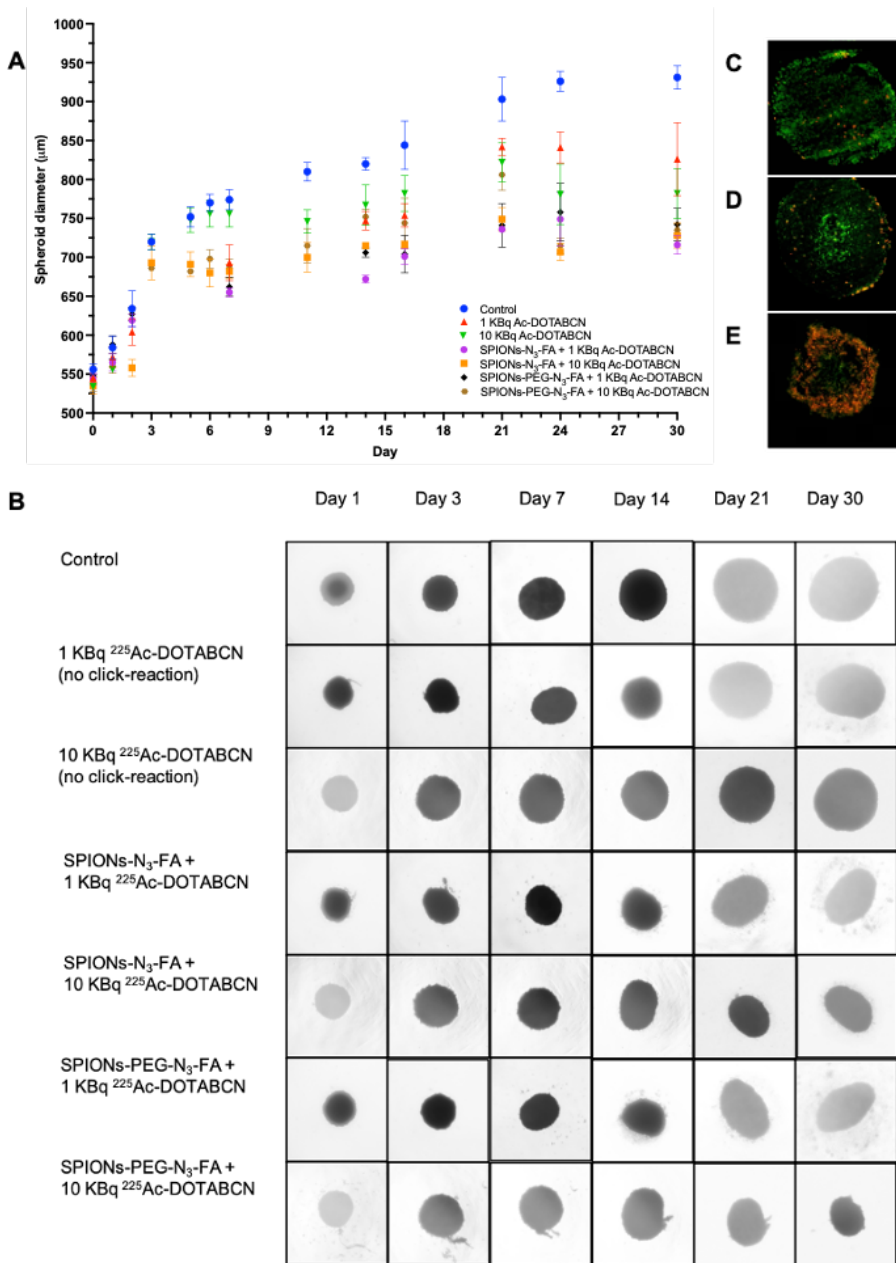


Figure 5.5. The U87 tumor spheroid growth after incubation(4h) with azide-functionalized SPIONs (SPIONs-N₃-FA and SPIONs-PEG-N₃-FA) and the subsequent treatment with 1 and 10 kBq of ²²⁵Ac-DOTA-BCN (30 min). Spheroids treated with only ²²⁵Ac-DOTA-BCN (no click-reaction) indicate the control (**A-B**). The LIVE/DEAD cells staining of spheroids at Day 30 for spheroids not exposed to SPIONs and spheroids incubated first with azide-functionalized SPIONs respectively (**C-E**). The colors correspond to: live (green) and death (red) cells.

It can be seen that the spheroids treated with combination of SPIONs and 1 kBq ^{225}Ac -DOTA-BCN, stopped growing at Day 21 (Figure 5.5B). As expected, increasing the activity to 10 kBq had even more pronounced effect, which could be observed already at Day 3. The loss of the spherical shape by the spheroids after the click-reaction can be explained by the inhomogeneous distribution of SPIONs and consequently the treated area being on one site of the spheroid. In contrast, spheroids that were not pre-treated with SPIONs retained the spherical shape (Figure 5.5B).

Furthermore, to further determine the actual cells killing potential of the treatment, a LIVE/DEAD assay as performed on Day 30 (Figure 5.5). The green and red colors represent the live and dead cells, respectively. The results show that using 10 kBq of activity after thirty days a significant number of dead cells can already be detected in the inner core of the spheroid, when PEGylated SPIONs were used (Figure 5.5E). The non-PEGylated SPIONs mostly caused damage on the outer surface of the spheroid (Figure 5.5D), but treatment with both types of SPIONs resulted in more dead cells compared to the non-treated tumors (Figure 5.5C). Moreover, spheroids treated with PEGylated-SPIONs (Figure 5.5D) showed highest degree of damage.

The ^{225}Ac therapeutic evaluation based on DNA damage

The DNA damage as the result of the two-step tumor targeting was evaluated by immunostaining of the double strand break (DSB) using a γ -H2AX primary antibody.^[17] Figure 5.6 shows that the DNA damage increases with increased activity, indicating that the damage of the spheroids incubated with azide-functionalized SPIONs is much more pronounced than in the case of the spheroids treated with only ^{225}Ac -DOTA-BCN. At Day 7 after the click-reaction even more DNA-DSB breaks are detected in the inner core part of spheroids. This finding is in line with the spheroid growth experiment, which shows that size of the spheroid treated with the combination of azide-functionalized SPIONs and 10 kBq of ^{225}Ac -DOTA-BCN did not significantly grow after seven days. Obviously, the click-reaction between ^{225}Ac -DOTA-BCN and SPIONs within 30 min resulted in more DNA damage induced to the U87 glioblastoma spheroids which has led to apoptosis.^[21] This fast and selective reaction is very promising for the further application of *in vivo* click-reaction for cancer treatment.

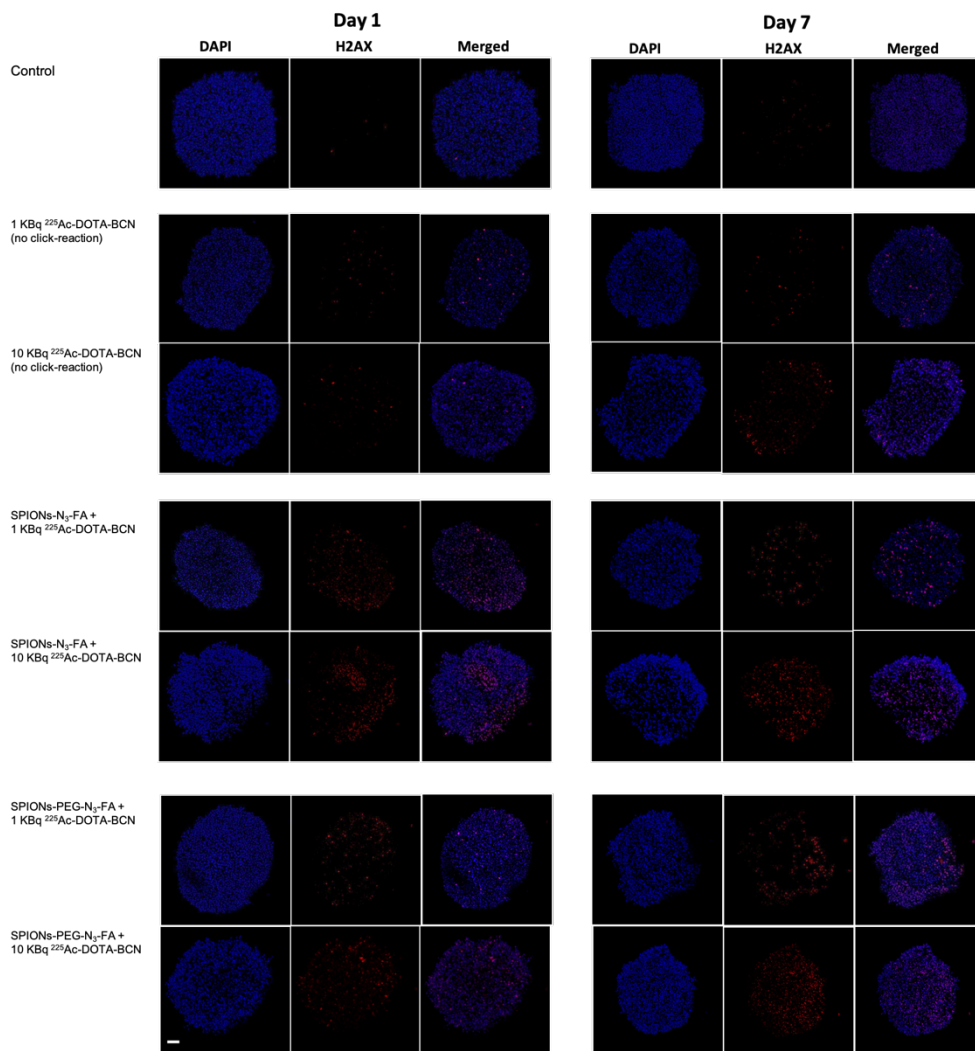


Figure 5.6 Confocal fluorescence microscope images of 3D spheroid U87 at Day 1 (**left**) and Day 7 (**right**) after the 30 minutes click-reaction of azides-functionalized SPIONs (SPIONs- N_3 -FA and SPIONs-PEG- N_3 -FA) with ^{225}Ac -DOTA-BCN 1 and 10 kBq. Spheroid treated only with 1 and 10 kBq ^{225}Ac -DOTA-BCN (no click-reaction) and non-treated spheroids are also included for comparison. The colors correspond to: DNA damage *via* γ -H2AX protein (red) and nucleus stained with DAPI (blue). Scale bar 100 μm .

Conclusions

In this chapter the therapeutic potential of the click-reaction between ^{225}Ac -DOTA-BCN and azide-functionalized SPIONs was investigated in 3D tumor models and compared to an unspecific incubation with ^{225}Ac -DOTA-BCN. The results show that the click-reaction is much more efficient in destroying the cancer cells as evident by the percentage of dead cells as well as the much slower growth of the spheroids.

PEGylated and non-PEGylated SPIONs were both investigated in combination with ^{225}Ac -DOTA-BCN but no significant differences were found for either the degree of click-reaction with ^{225}Ac -DOTA-BCN or DNA damage. Therefore, we believe that PEGylated nanoparticles should be considered for further *in vivo* application, since they are expected to have longer circulation times and hence higher tumor accumulation.

The two-step tumor targeting approach using combination of azide-functionalized SPIONs and ^{225}Ac -DOTA-BCN *via* click-reaction is considered to be promising for alpha-radionuclide therapy as it can fast and selectively deliver the alpha-emitter to the tumor with minimum damage to healthy cells. The safety of this approach for the healthy tissues should be further evaluated using the cells that do not overexpress FA-receptors.

Experimental details

Materials and Methods. All reagents and solvents used were of analytical and synthetic grade. 1,4,7,10-Tetraazacyclododecane-1,4,7,10-tetraacetate cyclooctyne (DOTA-BCN) was purchased from Chematech (Dijon, France), ammonium acetate (NH_4OAc), ethylenediaminetetraacetic acid (EDTA), glycine, hydrochloric acid (HCl) and sodium hydroxide (NaOH) were purchased from Sigma-Aldrich. MQ H_2O was obtained from a Milli-Q System. Iron oxide nanoparticles (SPIONs) were prepared and functionalized as described in Chapter 3. γ -H2AX primary antibody and secondary antibody Alexa Fluor 568 were purchased from ThermoFisher.

The confocal microscope used was Nikon A1R confocal with 20 \times magnification. Laser excitation at 405 and 560 nm were applied for DAPI and γ -H2AX marker, respectively. The obtained data was analyzed with Image-J software using FIJI.

The inverted microscope used was a SZ 45 B zoom Binocular stereo microscope 7×-45× and using 2× magnification. Spheroid images were taken using 12 MP camera and analyzed with Samplescan software.

The luminescence spectroscope used was Agilent Technologies Cary Eclipse Spectrophotometer (bio/chemiluminescence data mode) applied at integration time of 0.2–1 s. The emission wavelength and slit used were 600 and 20 nm, respectively.

The count rates of ^{221}Fr and ^{231}Bi and were determined with a Perkin Elmer 2480 automated γ -counter WALLAC using the gamma photons of 218 and 440 KeV for ^{221}Fr and ^{231}Bi , respectively.

Cryosectioning of the spheroids was performed with a cryostat Leica CM1900. The cryostat was operated under the following conditions: cryostat temperature -25°C , cutting table temperature -20°C , cutting size was set to 10-20 μm , freezing medium PELCO Cryo-Embedding Compound was used to freeze the samples.

Radiolabeling of DOTA-BCN with ^{225}Ac . The ^{225}Ac was provided by the Directorate for Nuclear Safety and Security Karlsruhe, Germany. Radiolabeling of DOTA-BCN with ^{225}Ac radionuclide was done following the previously published method.^[18] 90 μL of a solution containing 62 μg of DOTA-BCN in 250 mM NH_4OAc at pH 5.5 were added to 100 μL of an acidic solution of ^{225}Ac (0.5 MBq/pmol). 10 μL of 2% ascorbic acid was also added to avoid the breaking of DOTA chemical bonds during the radiolabeling with ^{225}Ac . The mixtures were stirred during 1h at 90°C . The radiochemical purities were determined by Thin Layer Chromatography (TLC) using 0.1M EDTA and 0.1M NH_4OAc (1:1) as the mobile phase with R_f ^{225}Ac -DOTA-BCN = 0 and R_f $^{225}\text{Ac}^{\text{III}}$ = 1. The radiolabeling yields were determined by automated γ -counter. 0.2 mL of the solution of ^{225}Ac -DOTA-BCN was diluted in PBS (until the desired activity) for *in vitro* click-reaction studies.

Cell culture. U87 cell lines (obtained from Erasmus Medical Centre, Rotterdam, The Netherlands) were cultured regularly in T-75 flask using Dulbecco's Modified Eagle Medium (DMEM) containing 10% Fetal Bovine serum (FBS) and 1% Penicillin-Streptomycin (10000 $\mu\text{g}/\text{mL}$) until they reached their 90% confluence (5-7 days).

In vitro click-reaction between azide-functionalized SPIONs and ^{225}Ac -DOTA-BCN. U87 spheroids were first incubated for 4h with azide-functionalized SPIONs and then ^{225}Ac -DOTA-BCN (100 Bq/20 pmol) were added and left for another 30 min. Subsequently, the spheroids were washed three times with PBS and collected by using membrane filter. The remaining activity of ^{225}Ac was determined by automated γ -counter following the protocols established for its daughter radionuclides ^{221}Fr and/or ^{213}Bi (n=3).

2D U87 cells treated with SPIONs were incubated with ^{225}Ac -DOTA-BCN (100 Bq/20 pmol) for 30 min. The membrane bound and internalized SPIONs fractions were determined by glycine treatment in which glycine-HCl (50 mM, pH 2.8) and NaOH 0.1 N were added to the cells consecutively, and left for 5 min. All fractions were collected in Eppendorf tubes and ^{225}Ac -activities were measured by automated γ -counter with the corresponding protocols (^{221}Fr and/or ^{213}Bi) (n=3).

Cell viability after ^{225}Ac -DOTA-BCN treatment. 3D spheroids composed of U87 with the size of 400-500 μm were incubated first with SPIONs- N_3 -FA for 24h. Different activities of ^{225}Ac -DOTA-BCN (0.1-10000 Bq) were added and the cells were incubated for another 30 min at 37 °C and with 5% CO_2 . Subsequently, the medium was removed and replaced by the Celltiter-Glo3D reagent to determine the number of viable cells in the spheroid (n=5).

Similar experiment was also conducted using a 2D U87 cells. U87 cell lines (1×10^4 cells per well) in 200 μL of DMEM medium were seeded into a 96-well plate for one day and after incubated for 24h with SPIONs- N_3 -FA. Different activities of ^{225}Ac -DOTA-BCN (0.1-1000 Bq) were added and the cells were incubated for another 30 min at 37 °C and with 5% CO_2 . The number of viable cells was determined with CCK-8 assays (n=5).

Spheroid growth observation. After the spheroids reached the size of 400-500 μm they were incubated with two different azide-functionalized SPIONs (SPIONs- N_3 -FA and SPIONs-PEG- N_3 -FA) for 4h. Two different activities of ^{225}Ac -DOTA-BCN (1 and 10 kBq) were added and the cells were incubated for another 30 min followed by washing with PBS (3 \times) and then incubated in DMEM culture medium (without any radiotracers). Spheroid growth was observed for 30 days using the inverted microscope. Spheroids non-treated or treated only with ^{225}Ac -DOTA-BCN were included for comparison. The obtained images were analysed using FIJI by Image-J software (n=3).

DNA damage immunostaining. To observe the DNA damage caused by ^{225}Ac upon the click-reaction, the DSB were stained and confocal fluorescence microscope was used for the analysis. After spheroids were incubated for 4h with azide-functionalized SPIONs (SPIONs- N_3 -FA and SPIONs-PEG- N_3 -FA), 1 and 10 kBq of ^{225}Ac -DOTA-BCN were added and the cells were incubated for 30 min. Spheroids were washed with PBS and fresh DMEM medium was added. At Day 1 and 7, spheroids were fixed with 4% paraformaldehyde at RT for 15 min. For the spheroid immunostaining, spheroids were incubated with 0.1% Triton 100X for 15 min and blocking buffer 4% Bovine Serum Albumin (BSA) for 1h at RT. Subsequently, the primary antibody of γ -H2AX (1/200 in 4% BSA) was added, the cells were incubated overnight at 4 °C and then washed with PBS (3 \times). Afterwards, the secondary antibody Alexa fluor 568 (1/200 in 4% BSA) was added, the cells were incubated for another 1h at RT and then washed with PBS (3 \times) and DAPI was added to stain the nucleus for 15 min before observation with the confocal fluorescence microscope. Spheroids non-treated or treated only with ^{225}Ac -DOTA-BCN were included for comparison (n=3).

References

- [1] M. Makvandi, E. Dupis, J. W. Engle, F. M. Nortier, M. E. Fassbender, S. Simon, E. R. Birnbaum, R. W. Atcher, K. D. John, O. Rixe and J. P. Norenberg, *Targeted Oncology* **2018**, *13*, 189-203.
- [2] S. Poty, L. C. Francesconi, M. R. McDevitt, M. J. Morris and J. S. Lewis, *Journal of Nuclear Medicine* **2018**, *59*, 878-884.
- [3] R. M. de Kruijff, H. T. Wolterbeek and A. G. Denkova, *Pharmaceuticals (Basel)* **2015**, *8*, 321-336.
- [4] D. Teze, D. C. Sergentu, V. Kalichuk, J. Barbet, D. Deniaud, N. Galland, R. Maurice and G. Montavon, *Scientific Reports* **2017**, *7*, 2579.
- [5] S. Ahenkorah, I. Cassells, C. M. Deroose, T. Cardinaels, A. R. Burgoyne, G. Bormans, M. Ooms and F. Cleeren, *Pharmaceutics* **2021**, *13*.
- [6] L. Arazi, *Phys Med Biol* **2020**, *65*, 015015.
- [7] C. A. Alfred Morgenstern, Clemens Kratochwil, Mike Satheke, Leszek and K. a. F. Bruchertseifer, *Current Radiopharmaceuticals* **2018**, *11*, 200-208.
- [8] M. Miederer, D. A. Scheinberg and M. R. McDevitt, *Advanced Drug Delivery Reviews* **2008**, *60*, 1371-1382.
- [9] J. Kozempel, O. Mokhodoeva and M. Vlk, *Molecules* **2018**, *23*.
- [10] J. Li, Y. Hu, J. Yang, W. Sun, H. Cai, P. Wei, Y. Sun, G. Zhang, X. Shi and M. Shen, *Journal of Materials Chemistry B* **2015**, *3*, 5720-5730.
- [11] J. A. P. Nicholas J. Agard, and Carolyn R. Bertozzi, *Journal of the American Chemical Society* **2004**, *126*, 15046-15047.
- [12] R. Membreno, B. E. Cook, K. Fung, J. S. Lewis and B. M. Zeglis, *Molecular Pharmaceutics* **2018**, *15*, 1729-1734.
- [13] S. Poty, K. Mandleywala, E. O'Neill, J. C. Knight, B. Cornelissen and J. S. Lewis, *Theranostics* **2020**, *10*, 5802-5814.
- [14] J. C. K. a. B. Cornelissen, *American Journal Nuclear Medicine and Molecular Imaging* **2014**, *4*, 96-113.
- [15] S. Acharya and S. K. Sahoo, *Advanced Drug Delivery Reviews* **2011**, *63*, 170-183.

- [16] J. M. Idee, M. Port, C. Robic, C. Medina, M. Sabatou and C. Corot, *Journal of Magnetic Resonance Imaging* **2009**, *30*, 1249-1258.
- [17] A. Sharma, K. Singh and A. Almasan in *Histone H2AX Phosphorylation: A Marker for DNA Damage*, (Ed. L. Bjergbæk), Humana Press, Totowa, NJ, **2012**, pp. 613-626.
- [18] C. F. Ramogida, A. K. H. Robertson, U. Jermilova, C. Zhang, H. Yang, P. Kunz, J. Lassen, I. Bratanovic, V. Brown, L. Southcott, C. Rodriguez-Rodriguez, V. Radchenko, F. Benard, C. Orvig and P. Schaffer, *EJNMMI Radiopharmacy and Chemistry* **2019**, *4*, 21.
- [19] H. S. Chan, E. de Blois, M. W. Konijnenberg, A. Morgenstern, F. Bruchertseifer, J. P. Norenberg, F. J. Verzijlbergen, M. de Jong and W. A. P. Breeman, *EJNMMI Radiopharmacy and Chemistry* **2017**, *1*, 9.
- [20] M. Kapalczynska, T. Kolenda, W. Przybyla, M. Zajaczkowska, A. Teresiak, V. Filas, M. Ibbs, R. Blizniak, L. Luczewski and K. Lamperska, *Archivers of Medical Science* **2018**, *14*, 910-919.
- [21] R. M. Kruijff, R. Raave, A. Kip, J. Molkenboer-Kuening, A. Morgenstern, F. Bruchertseifer, S. Heskamp and A. G. Denkova, *Scientific Reports* **2019**, *9*, 11671.

Summary

Radiation therapy has made tremendous progress in oncology over the last decades due to advances in engineering and physical sciences in combination with better biochemical, genetic and molecular understanding of this disease. Local delivery of optimal radiation dose to a tumor, while sparing healthy surrounding tissues, remains a great challenge, especially in the proximity of vital organs. Therefore, imaging plays a key role in tumor staging, accurate target volume delineation, assessment of individual radiation resistance, and even personalized dose prescription. From this point of view, radiation therapy (both external and internal) might be one of the few therapeutic modalities that relies entirely on high-resolution imaging. **Chapter 1** gives a short overview of the strategies in radionuclide therapy in terms of targeted drug delivery in combination with magnetic resonance imaging (MRI).

MRI with its superior soft-tissue resolution is already used in radiotherapy treatment planning, complementing conventional computed tomography (CT). Development of systems integrating MRI and linear accelerators opens possibilities for simultaneous imaging and therapy, which in turn, generates the need for imaging probes with therapeutic components. The role of MRI in both external and internal radiotherapies, as well as the most important examples of contrast agents with combined therapeutic functionalities, are surveyed in depth in **Chapter 2**.

Superparamagnetic iron oxide nanoparticles (SPIONs) have been studied extensively as contrast agents for T_2 -weighted MR imaging due to their effect on the transversal relaxation of protons in surrounding tissues, leading to dark contrast. With a proper surface modification, SPIONs are promising materials not only for MRI diagnosis but also for therapeutic purposes, such as drug delivery and magnetic hyperthermia. **Chapter 3** focuses on the preparation of SPIONs with the properties determined by morphological characteristics. Based on experimental results, thermal decomposition was identified as the best method leading to SPIONs with a diameter below 10 nm and narrow size distribution. Evaluation of magnetic properties of these nanoparticles revealed maghemite-like crystal

structures composed of Fe^{3+} -ions in octahedral configuration. Surface functionalization of the prepared SPIONs with folic acid was designed to increase their selectivity towards cancer cells. This targeting vector is known to bind to folic acid receptors overexpressed by a number of tumors, including ovarian, breast and cervical cancers. Furthermore, functionalization with azide-groups was implemented to enable the envisioned click-reaction with cyclooctyne-modified drug molecules. Thereby, azide-groups were introduced either directly to the surface of the nanoparticles or as terminal groups on polyethylene glycol (PEG) molecules. Finally, a small part of PEG molecules was provided with a fluorescent tag (fluoresceine) that allowed to perform microscopy during the *in vitro* evaluations of these nanoparticles. The r_2 -relaxivities (85 and 45 $\text{mM}^{-1}\text{s}^{-1}$) and magnetic moments (10-11 emu) of the functionalized SPIONs are in agreement with the determined $\gamma\text{-Fe}_2\text{O}_3$ composition. The preliminary 2D *in vitro* study confirmed the importance of folic acid for targeting properties of SPIONs, while the presence of PEG-molecules resulted in lower cytotoxicity and higher accumulation on the tumor cells compared to the non-PEGylated nanoparticles.

Despite a high therapeutic potential, clinical acceptance of radionuclide therapy is hampered by the undesired side-effects caused by an unspecific delivery of radiopharmaceuticals. Therefore, different strategies are being investigated to minimize the risk and improve the outcome radionuclide therapy. The concept of tumor pre-targeting based on biorthogonal mechanism *via* click-reaction, presented in **Chapter 4**, is one of possible ways for prompt delivery of radiopharmaceuticals. For this purpose, 1,4,7,10-tetraazacyclododecane-1,4,7,10-tetraacetate (DOTA) was used as a potential chelate for complexation of alpha-emitting radiometals, while its modification with cyclooctyne (BCN) was utilized for the click-reaction with azide-functionalized SPIONs that were pre-delivered to the tumor in a targeting manner. To study the rate of the click-reaction, DOTA-BCN was complexed with diamagnetic and luminescent Eu^{III} -ions and the reaction with a model azide-compound was followed by NMR and UV-spectroscopies. Based on these results, 30 min reaction time was considered to be sufficient for the formation of the click-reaction adduct. In the following, DOTA-BCN was complexed with paramagnetic Gd^{III} -ions and the click-reaction with azide-functionalized SPIONs was carried out. The efficiency of the reaction

was evaluated by T_1/T_2 NMR relaxation measurements. Next, *in vitro* studies using 3D and 2D tumor cell models were conducted using SPIONs- N_3 -FA and SPIONs-PEG- N_3 -FA for the click-reactions with DOTA-BCN complexed to two long-lived radionuclides, ^{111}In ($t_{1/2} = 2.8$ d) and ^{177}Lu ($t_{1/2} = 6.6$ d), which could be quantified using gamma-counting. The results confirmed completion of the reaction within 30 min demonstrating the maximum uptake of 0.2% of ^{111}In -DOTA-BCN and 0.1% of ^{177}Lu -DOTA-BCN by the U87 spheroids after the click-reactions with azide-functionalized SPIONs (SPIONs- N_3 -FA and SPIONs-PEG- N_3 -FA). The differences in uptake of these complexes found in 2D systems could be attributed to the differences in morphology of 2D compared to 3D cell models. Furthermore, a preference of the non-PEGylated nanoparticles for accumulation at the surface of tumor cells was observed. Finally, evaluation of therapeutic effect of ^{177}Lu as a beta-emitter suggested that 1 MBq is already sufficient for a notable decrease of the cell viability.

Alpha-radionuclide therapy can become a very powerful cancer treatment, provided that the harmful aspects are taken care of. Short penetration depth and high linear energy transfer (LET) of alpha-particles is leading to direct DNA damage of the cells, both cancerous and healthy. Another point of concern is the presence of recoiling high-energy daughter-nuclides. Therefore, minimization of radiation exposure through specific delivery to the site of interest is even more important in the case of alpha-emitters than for any other radionuclides. In **Chapter 5**, the pre-targeting approach is adopted to an alpha-emitting radionuclide ^{225}Ac ($t_{1/2} = 10.0$ d) complexed with DOTA-BCN. *In vitro* evaluation using the combination of previously developed azide-functionalized SPIONs was further investigated using 3D glioblastoma spheroid model. The growth of the spheroids and the DNA damage caused by the alpha-particles were studied. The results demonstrate the efficiency of the click-reaction in destroying cancer cells as the slower growth was observed starting from day 21 and day 7 for 1 kBq and 10 kBq of added ^{225}Ac -DOTA-BCN, respectively. As both non-PEGylated and PEGylated SPIONs have shown similar therapeutic outcome upon the click-reaction with ^{225}Ac -DOTA-BCN, the latter nanoparticles are suggested for the further *in vivo* investigations due to their minimized immune-response.

Samenvatting

Radiotherapie heeft de afgelopen decennia enorme vooruitgang geboekt in de oncologie dankzij de vooruitgang in technische en fysische wetenschappen in combinatie met betere biochemische, genetische en moleculaire inzichten in deze ziekte. Lokale afgifte van een optimale stralingsdosis aan een tumor, terwijl gezonde omliggende weefsels worden gespaard, blijft een grote uitdaging, vooral in de nabijheid van vitale organen. Beeldvorming speelt een belangrijke rol bij de nauwkeurige evaluatie van de tumoren; identificatie van het tumorstadium, het doelvolumen, beoordeling van de stralingsbestendigheid, en zelfs bepaling van de gepersonaliseerde dosis. Vanuit dit oogpunt zou radiotherapie (zowel externe als interne) een van de weinige therapeutische modaliteiten kunnen zijn die volledig afhankelijk is van hoge resolutie beeldvorming. **Hoofdstuk 1** geeft een kort overzicht van de verschillende strategieën in radionuclidetherapie, in termen van gerichte dosisafgifte in combinatie met magnetische resonantie imaging (MRI).

MRI wordt al gebruikt bij de planning van radiotherapiebehandelingen door zijn superieure resolutie van zachte weefsels, als aanvulling op conventionele computertomografie (CT). Ontwikkeling van systemen die MRI en lineaire versnellers integreren biedt kansen voor gelijktijdige imaging en therapie, wat op zijn beurt de behoefte genereert voor de probes met beide componenten. De rol van MRI bij zowel externe als interne radiotherapieën, evenals de belangrijkste voorbeelden van contrastmiddelen met bijkomende therapeutische functionaliteiten, worden in **Hoofdstuk 2** uitgebreid besproken.

Superparamagnetische ijzeroxide nanodeeltjes (SPIONs) zijn uitgebreid bestudeerd als contrastmiddelen voor T_2 -gewogen MR beeldvorming vanwege hun effect op de transversale relaxatie van protonen in omliggende weefsels, wat leidt tot donker contrast. Met een goede oppervlaktemodificatie zijn SPIONs veelbelovende materialen, niet alleen voor MRI-diagnose, maar ook voor therapeutische doeleinden zoals drugafgifte en magnetische hyperthermie. **Hoofdstuk 3** richt zich op de bereiding van SPIONs met de eigenschappen die bepaald zijn door de morfologische kenmerken. Op basis van experimentele resultaten werd thermische decompositie geïdentificeerd als de beste

methode, resulterend in SPIONs met een diameter kleiner dan 10 nm en een smalle grootteverdeling. Evaluatie van de magnetische eigenschappen van deze nanodeeltjes onthulde maghemiet-achtige kristalstructuren die waren samengesteld uit Fe³⁺-ionen in octaëdrische configuratie. Conjugatie van foliumzuur aan de oppervlakte van SPIONs was toegepast om hun selectiviteit naar tumorcellen te vergroten. Van deze targeting vector is bekend dat deze bindt aan foliumzuurreceptoren die tot overexpressie worden gebracht door een aantal tumoren, waaronder eierstok-, borst- en baarmoederhalskanker. Verder werden SPIONs gefunctionaliseerd met azide-groepen om de beoogde click-reactie met cyclooctyn-gemodificeerde drugmoleculen mogelijk te maken. Daarbij werden N₃-groepen ofwel direct op het oppervlak van de nanodeeltjes geïntroduceerd, ofwel als eindgroepen op polyethyleenglycol (PEG) moleculen. Ten slotte werd een klein deel van de PEG-moleculen voorzien van een fluorescerende tag (fluoresceïne) die het mogelijk maakte om deze SPIONs *in vitro* met microscopie te evalueren. De r₂-relaxiviteiten (85 en 45 mM⁻¹s⁻¹) en magnetische momenten (10-11 emu) van de gefunctionaliseerde SPIONs zijn in overeenstemming met de vastgestelde γ-Fe₂O₃-samenstelling. De 2D *in vitro* studie bevestigde het belang van foliumzuur voor de targeting eigenschappen van SPIONs, terwijl de aanwezigheid van PEG-moleculen resulteerde in lagere cytotoxiciteit en hogere accumulatie bij de tumorcellen in vergelijking met de niet gePEGyleerde nanodeeltjes.

Ondanks een hoog therapeutisch potentieel wordt de klinische acceptatie van radionuclidetherapie belemmerd door de ongewenste bijwerkingen veroorzaakt door de niet-specifieke afgifte van radiofarmaceutica. Verschillende strategieën worden onderzocht om het risico te minimaliseren en de uitkomst van radionuclidetherapie te verbeteren. Het concept van tumor pretargeting op basis van een biorthogonaal mechanisme via een click-reactie, gepresenteerd in **Hoofdstuk 4**, is een van de mogelijke manieren voor de snelle levering van radiofarmaceutica. Voor dit doel werd 1,4,7,10-tetraazacyclododecaan-1,4,7,10-tetraacetaat (DOTA) gebruikt als een potentieel ligand voor het complexeren van alfastralers. Modificatie van DOTA met cyclooctyn (BCN) werd gebruikt voor de click-reactie met azide-geconjugeerde SPIONs die vooraf op een doelgerichte manier aan de tumor waren afgeleverd. Om de snelheid van de click-reactie te bestuderen, werd DOTA-BCN gecomplexeerd met luminescerende Eu^{III}-ionen, en de reactie met een model-N₃-verbinding

werd gevolgd met NMR- en UV-spectroscopieën. Op basis van deze resultaten werd een reactietijd van 30 minuten als voldoende beschouwd voor de vorming van het click-reactie adduct. Vervolgens werd DOTA-BCN gecomplexeerd met paramagnetische Gd^{III}-ionen en werd de click-reactie met azide-geconjugeerde SPIONs uitgevoerd. De efficiëntie van de reactie werd geëvalueerd door T₁/T₂ NMR-relaxatiemetingen. *In vitro* studies werden uitgevoerd met 3D- en 2D-tumorcelmodellen met SPIONs-N₃-FA en SPIONs-PEG-N₃-FA in de click-reacties met DOTA-BCN gecomplexeerd met twee langlevende radionucliden, ¹¹¹In (t_{1/2} = 2.8 d) en ¹⁷⁷Lu (t_{1/2} = 6.6 d). Gammatelling werd toegepast om resultaten te kwantificeren en het voltooien van de reactie binnen 30 min te bevestigen. De maximale opname van 0.2% van ¹¹¹In-DOTA-BCN en 0.1% van ¹⁷⁷Lu-DOTA-BCN door de U87-sferoïden toonde de click-reacties met N₃-geconjugeerde SPIONs aan. Verschillen in opname van deze complexen in 2D-systemen werden toegeschreven aan de verschillen in morfologie van 2D in vergelijking met 3D-celmodellen. Verder werd een voorkeur waargenomen van de niet gePEGyleerde SPIONs om te accumuleren op het oppervlak van de tumorcellen. Ten slotte suggereerde evaluatie van het therapeutische effect van de beta-emitter ¹⁷⁷Lu (t_{1/2} = 6.6 d) dat 1 MBq al voldoende is voor een opmerkelijke afname van de levensvatbaarheid van de cellen.

Alfa-radionuclidetherapie kan een zeer krachtige kankerbehandeling worden, op voorwaarde dat de schadelijke aspecten worden aangepakt. Korte penetratiediepte en de hoge lineaire energieoverdracht (LET) van alfadeeltjes leidt tot directe DNA-schade van zowel tumor als gezonde cellen. Een ander punt van aandacht is de aanwezigheid van terugspringende hoogenergetische dochternucliden. Daarom is het minimaliseren van de blootstelling aan de straling door specifieke afgifte aan de betreffende locatie nog belangrijker in het geval van alfastralers dan voor andere radionucliden. In **Hoofdstuk 5** wordt pretargeting toegepast op een alfa-emitterende radionuclide ²²⁵Ac (t_{1/2} = 10.0 d) gecomplexeerd met DOTA-BCN. *In vitro* evaluatie met behulp van de combinatie van eerder ontwikkelde N₃-geconjugeerde SPIONs werd verder onderzocht met behulp van 3D glioblastoma sferoïde model. De groei van de sferoïden en de DNA-schade veroorzaakt door de alfadeeltjes werden bestudeerd. De resultaten demonstreren de efficiëntie van de click-reactie bij het vernietigen van kankercellen. Een langzamere groei werd waargenomen

vanaf dag 21 en dag 7 voor respectievelijk 1 kBq en 10 kBq toegevoegde ^{225}Ac -DOTA-BCN. Zowel niet gePEGyleerde als gePEGyleerde SPIONs laten vergelijkbare therapeutische resultaten zien na de click-reactie met ^{225}Ac -DOTA-BCN. Daarom wordt het gebruik van gePEGyleerde SPIONs voorgesteld voor verdere *in vivo* studies vanwege de verwachte minimale immuunresponse.

Acknowledgements

Truthfully speaking, pursuing a PhD with cultural and linguistic challenges was not easy for me. Therefore, I really want to show my appreciation to everyone who became a part of this PhD journey.

Firstly, I am not sure this acknowledgement is enough for me to express my gratitude toward you, **Kristina**. You helped me a lot during this PhD journey. Thank you for everything. You were always there to answer my questions, share your knowledge and understand my limitations. You were never tired of guiding and making me learn from my mistakes. You always encouraged me to do better. You are not only an amazing promotor but also a warm friend and mom for me. You are an inspiration to me and I am lucky to have you as my promotor.

I am also indebted to **Antonia**. Thank you for allowing me to be a part of the Applied Radiation and Isotopes (ARI) Group. Without your guidance, support, and suggestions, I am not sure I would have been able to do the final (radioactive) experiments. Thank you for your trust and patience, despite my knowledge limitations on radioactivity. I learned a lot from you, and I cannot imagine finishing this PhD project without you and Kristina.

Furthermore, I also want to give my thanks to my previous promotor, **Isabel** and **Ulf**. You comforted me a lot during the first stage of my PhD in Biocatalysis (BOC) Group. Even though it was very short for me to learn more from you both, I am really grateful I had your guidance in the beginning, when needed the most. Thank you for the really nice discussions regarding your unlimited chemistry knowledge.

Being a part of the two groups was very challenging at first. In retrospective, it is a really good advantage. I would like to extend my thanks to all my colleagues from the BOC and ARI groups.

To **Mieke** and **Anouk**, thank you both for helping me settle in BOC and ARI. Thank you to **Stephen** for all the advice, guidance, and discussions on the NMR-experiments and laboratory-related stuff. To **Laura**, thank you for your fast-reply with the information regarding the bio-related instruments in BOC lab, and for assisting me in using them. Next,

to **Duncan, Caroline, Frank, Peter-Leon, Fred, Linda, Marc, Lloyd, and Remco**, thank you for the really nice discussions during the time I spent in BOC. **Astrid**, thank you for your patience while guiding me to start my work with U87 and HeLa cells, the radioactive experiments with ^{111}In , ^{177}Lu , and most importantly with ^{225}Ac . Thank you for always sharing your knowledge and experience while we worked in the Bio-Lab. **Baukje**, thanks a lot for training me in ICP and microwave instruments, even though I always texted or called when I experienced problems with the ICP-stuff. Thank you for answering all my lab-related questions. **Folkert**, thank you for assisting me with the computer and software problems I encountered both in the lab and office. **Mehmet** and **Delia**, thank you for the proper training on the freeze dryer. **Adrie**, thank you for showing me how to work with HPLC and spectroscopies instruments when you were still in ARI. To **Eline**, thank you for the time we spent together working with the WALLAC when Astrid and Folkert were not around. And also, to **Robin**, thank you for really nice suggestions on working with radioactivity in the lab and also for sharing your experience on dealing with 'unpredicted amount' of ^{225}Ac arrival from Karlsruhe Institute to the Reactor Institute.

Special thanks to all SBD People: **Radboud, Erwin, Hanks, Jossete, Misja, Maris, and Coos** for assisting me with the radioactive experiments including giving feedback for my IV and checking several times the contamination-suspect stuff of ^{111}In , ^{177}Lu or ^{225}Ac when I was working in the lab. Also, thanks to **Dosti, Ico, and Rene** regarding the radioactive course, the laboratory access, and the endless supply of ^{111}In or ^{177}Lu from our colleagues in Erasmus MC, respectively.

I also want to give my thanks to my fellow PhDs and Postdocs for creating this unforgettable PhD journey. To **Alexandra**, thank you for being there with me on figuring out how to deal with the 'two-groups' lab experiments hurdles while preparing our Fe nanoparticles. And also, I want to give my sincere thanks to you for advising me on my English due to my English-limitation. To **Huanhuan**, thank you for the cheerful vibes in our office and ARI. We started our PhD project at almost the same time and you always motivated me to finish my work and write as soon as possible. I hope we can meet again in the future (in Bali perhaps?). To **Robin**, thank you for guiding me a lot during the cells experiments. Your awesome knowledge and skills made me learn how to properly work with cells. Thanks also to **Rogier**,

Chao, Runze, Hu, Svenja, Rogelio, Tiantian, Rupali from ARI and **Wuyuan, Florian, Luuk, Marine, Seb, Stefan, Morten, Albert, Sam, Jose, Eman, Xiaomin** from BOC, not only for the nice discussions regarding the work-based knowledge, but also for the valuable time that we spent together during coffee, lunch, and *borrel* time. I would also like to thank my master and bachelor students, **Jairus, Jaap, and Alysha**, for helping me with my research during this PhD project.

My sincere thanks I express also to my colleagues in the BT, BN, CE and RST departments: **Ingrid, Patricia, Jeremie, Catia, Irfan, Wiel, Hendrik, Lars, Bart, Pedro, Anton, and Iulian** for assisting me while working with the instruments in their labs. This was great support through my PhD project.

I also would like to acknowledge **Indonesian Endowment Fund for Education (LPDP)** for giving me the full financial support to pursue my PhD degree at TU Delft. Additionally, to all my colleagues in Universitas Padjadjaran, **Prof. Husein, Prof. Ukun, Pak Abdul Mutalib, Bu Anni, Prof. Rista, Prof. Iman, Prof. Iman, Bu Desi, Bu Anne, and Pak Safri** thank you for always encouraging and motivating me in doing my PhD study abroad.

And to all the Indonesian PhD students in the Netherlands, especially to **Siti Farah, Bramka, Kartika, Kusnandar, Aldy, Antra, Nasikun, Mamin, Shabila, Asiyah, Nabriz, and Anni**, thank you for the wonderful times and memories that somehow helped me a lot to complete these ‘tough’ four years of my PhD journey in Delft.

The last and most important part, I would like to thank to all **my families** for the support, particularly to my parents, **Mama dan Bapa, terima kasih banyak selalu mendukung dan mendoakan anakmu**. To my beloved husband **Barokah**, I am really thankful for your endless love and patience, that helped me survive in order to accomplish my PhD degree. Even though we experienced so many unpredictable situations due to my poor health condition during the last stage of my PhD journey, together with our ‘Baby-Z’, we managed to go through it and eventually, we did it! I love you both ♥.

Delft, 10 December 2021



List of publications

Publications (this thesis)

R. Putri Fauzia, A. G. Denkova, and K. Djanashvili. Two-Step Radionuclide Tumor Targeting through Bioorthogonal Mechanism using SPIONs. **2022**. *Manuscript in preparation*.

R. Putri Fauzia, A. G. Denkova, and K. Djanashvili. Preparation and Surface Functionalization of Superparamagnetic Iron Oxide Nanoparticles Designed for Theranostic Applications. **2022**. *Manuscript in preparation*.

R. Putri Fauzia, A. G. Denkova, and K. Djanashvili. Potential of MRI in Radiotherapy Mediated by Small Conjugates and Nanosystems. *Inorganics* **2019**, 7, 59.

Other publications

H. Liu, R. Nadar, **R. Putri Fauzia**, A. van der Meer, Britt, Q. van Cooten, E. Carol, A. G. Denkova, and R. Eelkema. Combined Chemo-radionuclide Therapy by using Poly (ϵ -caprolactone-b-ethylene glycol) Micelles Co-loaded with Paclitaxel and ^{177}Lu . **2022**. *Manuscript in preparation*.

A. R. Noviyanti, N. Akbar, Y. Deawati, E. E. Ernawati, Y. T. Malik, **R. Putri Fauzia**, and Risdiana. A Novel Hydrothermal Synthesis of Nanohydroxyapatite from Eggshell-calcium-oxide Precursors. *Heliyon* **2020**, 6, e03655.

I. P. Maksum, A. Lestari, **R. Putri Fauzia**, S. D. Rachman, and U. M. S. Sudjanaatmadja. View of Escherichia coli BL21 (DE3) Expression System using TorA Signal Peptide for Recombinant Human Albumin (rHA) Secretion. *International Journal of Research in Pharmaceutical Sciences* **2019**, 10, 3319-3324.

D. Rakhmawaty Eddy, A. Anggraeni, **R. Putri Fauzia**, I. Rahayu, A. Mutalib, M. L. Firdaus, and H. Hernadi Bahti. Gadolinium-Mesoporous Silica as a Potential Magnetic Resonance Imaging Contrast Agent. *Oriental Journal Chemistry* **2018**, *34*, 2603-2607.

Oral Presentation

R. Putri Fauzia, A.G. Denkova, and K. Djanashvili. Preparation and Surface Functionalization of Superparamagnetic Iron Oxide Nanoparticles Designed for Theranostic Applications. The 5th International Seminar on Chemistry (ISC-2021). Indonesia, 27-28 October **2021**. Best parallel session lecture award.

Poster Presentation

R. Putri Fauzia and K. Djanashvili. Surface Functionalization of Iron Oxide Nanoparticles for Medical Applications. CHAINS Conference 2018. Veldhoven, The Netherlands. 3-5 December **2018**.

R. Putri Fauzia, R. U. M. S. Soedjanaatmadja, A. Hardi Gunawan and K. Djanashvili. Affinity Study on Gd-DTPA-PEG-Folate to Cervix Cancer Cells Overexpressing Folic Acid Receptors. Is Multimodal Imaging an Invention with a Future? The input of Chemistry Conference, Orleans, France, 11-13 December **2017**.

Curriculum Vitae



Retna Putri Fauzia was born on March 10th, 1990 in Serang, Indonesia. She obtained her bachelor degree in 2011, followed by her master degree in 2014 at the Department of Chemistry, Faculty of Mathematics and Natural Sciences, Universitas Padjadjaran, Indonesia under the supervision of Dr. Abdul Mutalib, Prof. Dr. R. Ukun. M. S. Sudjanaatmadja, and Dr. Anni Anggraeni. From 2014, she continued her career in Academia as a junior lecturer and researcher in Universitas Padjadjaran. Next, she joined a project with focus on the preparation of Magnetic Resonance Imaging Contrast Agents (MRI-CA) for cancer diagnostic. The project was a collaborative work between Universitas Padjadjaran, National Nuclear Energy Agency (BATAN-Serpong) and PT. Kimia Farma, Indonesia under the lead of Prof. Dr. Husein H. Bahti.

In 2016, she obtained the PhD scholarship from Indonesia Endowment Fund for Education (LPDP), followed by the start of her PhD on October 1st, 2017. For the next 4 years she pursued her PhD study at the Department of Biotechnology, Faculty of Applied Sciences, Delft University of Technology, The Netherlands under the supervision of Dr. Kristina Djanashvili and Dr. ir. Antonia G. Denkova. During this time, her research focused on the Two-Step Radionuclide Tumor Targeting through Bioorthogonal Mechanism using SPIONs which was performed in Reactor Institute Delft.

After completion of her PhD, she will pursue a career in Academia as a lecturer and continue her research at the Department of Chemistry, Faculty of Mathematics and Natural Sciences, Universitas Padjadjaran, Indonesia.